Experimental Evaluation and Modelling for Galvanically-Induced Localized Corrosion of AA70750-T6

A Dissertation ▾

Presented to

the faculty of the School of Engineering and Applied Science

University of Virginia

---

in partial fulfillment

of the requirements for the degree

Doctor of Philosophy ▾

by

Yijing Shi

May ▾

2015

APPROVAL SHEET

The dissertation ▼

is submitted in partial fulfillment of the requirements

for the degree of

Doctor of Philosophy ▼

AUTHOR

The dissertation has been read and approved by the examining committee: ▼

Rob Kelly

Advisor

James Burns, Chair

John Scully

Jason Lee

Gary Koenig

Accepted for the School of Engineering and Applied Science:

James H. Aylor

Dean, School of Engineering and Applied Science

May ▼

2015

Print Form

Experimental Evaluation and Modelling for Galvanically-Induced Localized Corrosion of AA7075-T6

A Thesis
Presented to
the faculty of the School of Engineering and Applied Science
University of Virginia
In Partial Fulfillment
of the requirements for the Degree
Doctor of Philosophy
Materials Science and Engineering
by
Yijing Shi
May 2015

Abstract

This research addresses the galvanically-induced localized corrosion of AA7075-T6 in contact with several noble materials (i.e., silver, nickel, bis-maleimides (BMI)/carbon fiber composites), under both full immersion and atmospheric conditions. The overall study is composed of two parts. First, a quantitative understanding of the fundamental mechanism for the stability of localized corrosion of AA7075-T6 is sought using electrochemical testing with both bulk samples and artificial pit samples. This understanding is then applied to galvanically-induced localized corrosion of AA7075-T6 under various environments including full immersion and atmospheric conditions using the finite element analysis (FEA) method in order to predict the scenarios (i.e., environment, area ratio) under which localized corrosion can be stabilized. Second, the conditions are identified under which the localized corrosion of AA7075-T6 could be mitigated when coupled with the above noble materials through the inhibition of oxygen reduction on the noble materials.

Acknowledgements

I would sincerely thank my advisor Rob Kelly for all his support and guidance. Rob brought the essential knowledge and innovative approach that allow me to crack the critical challenges timely through my PhD study. Moreover, he shares the students with his enthusiasm about the research and life, as well as his wisdom of being an encouraging advisor for his students, a passionate leader for our CESE, and a thoughtful father and husband for his family. I am truly grateful to have him as my advisor for my academic growth and mentor for a more meaningful life.

I would also like to acknowledge my committee members, John Scully, Jason Lee, Jimmy Burns, and Gary Koenig, for their advisement and review of all my work.

I would thank you for all of our CESE present members and alumni, as well as all the faculty, staffs and students at Materials Science and Engineering department. My completion of this long journey at U.Va would have not been achieved without your support, care and encouragement.

Thank you to my family and friends for being so patient and supportive during this long and demanding venture. Thank you for all your love, support, and sacrifice. Thank you for always believing in me and providing me with encouragement on my toughest days.

Table of Content

List of Table

List of Figures

List of Symbols

m: mass loss (grams),

I: current (amps),

t: time (sec),

A.W.: atomic weight (grams/mole),

F: Faraday's constant (96,498 coulombs/equivalent),

d: depth of artificial pit,

D: density of materials (g/cm^3),

r: radius of wire, were used in this study.

E_{corr} : the corrosion potential with a given solution,

ΔE_{ac} : the overpotential,

η_{IR} : ohmic drop inside the pit.

D_i : diffusion coefficient of species i,

c_i :concetration of species i,

z_i : charge of species i,

u_i : mobility of species i,

R_i : reaction rate of species i ,

F :Faraday's constant,

Φ : the potential of the solution.

$i^p a_{corr}$: anode corrosion current density,

$E^{p}a_{corr}$: anode corrosion potential,

$\alpha^{p}{}_{a}$: the anodic coefficient for the anode,

$\beta^{p}{}_{a}$: the cathodic coefficient for the anode,

z_i : the charge of ion specie,

u_i: the mobility of ion specie,

c_i : the concentration of specie,

R : the gas constant (8.31Jmol^{-1}K^{-1}).

.

Scope of Research

This research addresses the galvanically-induced localized corrosion of AA7075-T6 in contact with several noble materials (i.e., silver, nickel, bis-maleimides (BMI)/carbon fiber composites), under both full immersion and atmospheric conditions. The overall study is composed of two parts. First, a quantitative understanding of the fundamental mechanism for the stability of localized corrosion of AA7075-T6 is sought using electrochemical testing with both bulk samples and artificial pit samples. This understanding is then applied to galvanically-induced localized corrosion of AA7075-T6 under various environments including full immersion and atmospheric conditions using the finite element analysis (FEA) method in order to predict the scenarios (i.e., environment, area ratio) under which localized corrosion can be stabilized. Second, the conditions are identified under which the localized corrosion of AA7075-T6 could be mitigated when coupled with the above noble materials through the inhibition of oxygen reduction on the noble materials.

Overall of Dissertation

This dissertation consists of five chapters. Chapter 1 reviews the fundamentals of localized corrosion of aluminum alloys, including consideration of the effects of galvanic coupling with noble materials and atmospheric exposure. It also covers the basic framework used for numerical modeling of corrosion. Both the contributions and limitations of previous studies of localized corrosion and modeling are briefly highlighted. Chapter 2 discusses the mechanisms that control the stability of localized corrosion of AA7075-T6. Two criteria, the repassivation potential, $E_{rp,}$ and the stability product, i*x, were quantified for AA7075-T6 in the chloride solutions under full immersion. The correlation between these two criteria was confirmed. Chapter 3 characterizes the galvanically-induced localized corrosion of AA7075-T6 in both full immersion and atmospheric conditions. The effects of environmental parameters, including the chloride concentration, relative humidity, and the cathode-to-anode area ratio on the electrochemical kinetics and corrosion damage of AA7075-T6 were determined. The effectiveness of E_{rp} described in Chapter 2 for the prediction of damage under atmospheric conditions was validated through comparing the interfacial potential along galvanic coupling interface measured by SKP and the damage evolution. The galvanic electrochemical kinetics measured in this chapter was also applied as the boundary condition for the modelling work in Chapter 4. Chapter 4 describes the modeling approaches used to predict the stability of localized corrosion with various geometry and environmental parameters, which was achieved by comparing the resulting modelling outputs with the stability criteria from Chapter 2. A mitigation strategy through the addition of inhibitors was also discussed. Overall conclusions and future work was summarized in Chapter 5

Chapter 1 Background

Although high-strength Al alloys are widely used in aerospace structures due to their high strength-to-weight ratio, they are prone to localized corrosion due to the formation of galvanic cells on the scale of the alloy microstructure [1] . Localized corrosion of Al alloy can be further exacerbated by galvanic coupling with more noble materials when the couple is in a conductive, corrosive environment. Modern aerospace structures are increasingly involving such couples as a part of designs aimed at future weight reduction and higher performance. This chapter starts with a review of the important phenomena including both the mechanisms that control the localized corrosion of the Al alloy and the factors that affect the galvanic corrosion behavior (section 1.1.-1.2.) The goal of the review is to provide a context for the issues of interest in the dissertation. The modeling of localized corrosion is also briefly reviewed because the present study includes the use of a FEM modeling tool to analyze the role of geometry and atmospheric exposure conditions on the stabilization of localized corrosion (section 1.3). Because most aerospace applications involve atmospheric exposure rather than full immersion, literature concerning the properties of localized corrosion under atmospheric condition is also included. (section 1.4)

1.1 Galvanic induced localized corrosion of Aluminum alloys

High-strength Al alloys (such as AA7075-T6) and high-performance noble materials (such as Ag, Nickel and carbon-fiber composites) are widely used in the aerospace industry for weight-saving and military purposes. Due to their low electrochemical potentials and heterogeneous microstructures, Al alloys often suffer significant localized corrosion which is worsened when they are in contact with more noble materials in corrosive environments [2,3]. Galvanically induced localized corrosion thus has become a serious concern for the long-term reliability of aluminum alloy structures in these applications. The understanding and prevention of this type of corrosion is therefore important to ensure structural integrity in many engineering designs.

1.1.1. Galvanic corrosion fundamentals

Galvanic corrosion occurs when two dissimilar materials are electrically coupled in a corrosive electrolyte. The electrochemical kinetics of the reactions on the surfaces of the dissimilar materials, the conductivity of the electrolyte, the cathode/anode ratio, and the character of the electrically conductive path all affect the rate of corrosion damage [4]. Mixed potential-theory is commonly used to predict galvanic corrosion behavior [5]. It consists of two simple assumptions: (1) any electrochemical reaction can be divided into partial oxidation and reduction reactions, and (2) there can be no accumulation of electrical charge during an electrochemical reaction (i.e., charge conservation). A schematic graph is shown in Figure 1.1 to demonstrate the application of mixed potential theory. It can be experimentally demonstrated that electrochemical reactions are composed of two or more partial oxidation or reduction reactions. Accordingly, by knowing both the cathodic kinetics (oxygen reduction in the present study) and the anodic kinetics of metal dissolution, the coupling potential/corrosion rate can be determined to evaluate the galvanic corrosion behavior. However, the direct application of mixed potential theory is limited to galvanic systems with simple geometry; for a complex engineering structure. more sophisticated techniques, such as numerical modeling need to be used in order to account for the potential and current distributions that result from ohmic drop. These distributions interact with the electrochemical kinetics to create a spatial distribution of damage.

The present research deals with a galvanically-connected engineering structure where a bulk AA7075-T6 alloy is covered by a noble material coating (shown in Figure 1.2). The engineering structure could be exposed under either a full immersion or an atmospheric condition.

1.1.2. Localized Corrosion of AA7075

The most common forms of localized corrosion attack are pitting, crevice corrosion and stress-corrosion cracking [6]. The first two forms are considered in this study. Pitting is caused by the localized breakdown of passive film and the subsequent attack of the underlying metal at certain fixed specific sites [6,7]. Crevice corrosion occurs within narrow clearances or under shielded metal surfaces, and is often treated as a special case of pitting corrosion [8]. The initiation of the pitting is briefly introduced in the following section before justifying the focus of the dissertation research on the mechanism of propagation stability of localized corrosion.

1.1.3. Initiation of Pitting

The poor corrosion resistance of AA7075 is generally attributed to the presence of a significant population of second-phase intermetallic particles which are either anodic or cathodic relative to the alloy matrix, and thus spontaneously induce micro-galvanic cell pitting [1,9,10]. One of the critical potentials associated with pitting corrosion is the pitting potential, E_p, which was long considered to be the potential above which pits nucleate and the protective passive film starts to breakdown. [6,7][10]. A preliminary study in the present work showed that E_p can be strongly affected by both the pH value and the Cl^- concentration ($[Cl^-]$) as has been shown elsewhere [11]. However, a more modern view of pitting includes the concept of metastable pitting and a focuses on propagation as the key stage of localized corrosion in terms of engineering significance.

Metastable pitting are those that grow transiently, and they are observed at potentials well below E_p[12]. It has been shown that metastable pits can transition into stable pits and sustainably grow below E_p [12][13]. The stability of the growth depends on the kinetics of pit dissolution rather than the breakdown resistance of the passive film [10,12]. Therefore, understanding the controlling kinetics for pit growth stability is more of importance for the purpose of corrosion control and protection.

1.1.4. Propagation and Propagation Stability of pitting

Pits on passive surfaces can grow if and only if sufficiently aggressive conditions are maintained at and within the pit [14]. One of the parameters that determine whether those conditions are maintained is the electrochemical potential. Once initiated, pits grow unless the potential is more negative than the repassivation potential, E_{rp}, below which they can repassivate and thereby stop growing [13]. At potentials lower than E_{rp}, the current density at the corroding surface of the metal is too low to sustain the right local chemistry for pitting growth [15].

Determination of E_{rp} has been challenging experimentally. The value of E_{rp} attained from traditional cyclic polarization scans has been shown to have limited predictive power and poor repeatability [16,17]. Dunn and Sridhar have developed a new approach to determine E_{rp} for alloy 825 [18,19]. In their study, they first polarized the materials to a high potential to generate substantial corrosion damage, then slowly lowered the potential until the material with the severe damage was able to repassivate. They defined E_{rp} as the potential at which a threshold current density ($50\mu A/cm^2$) was reached. By plotting E_{rp} versus the charge density during the dissolution, they found that with an increase of the pit depth/damage (charge), E_{rp} decreased until a lower bound was reached. E_{rp} became independent of further increases in charge density. This phenomenon is shown in Figure 1.3-a. They then demonstrated that this E_{rp} was predictive of localized corrosion stability through the use of extremely long-term potentiostatic holds both above and below the measured E_{rp} [19] as shown in Figure 1.3-b. They found that no polarizations below E_{rp} led to localized corrosion for times out to 1,000days. Although it has been shown that the lower bound of E_{rp} can be used in the long-term prediction of the stability of localized corrosion of the tested alloy, the fundamental mechanism behind the observation has not been clearly established.

Several theories and models have been developed that can be used to interpret the correlation between the value of E_{rp} and the mechanism for controlling the stability of pitting growth. The two most prominent ones are the pit stability product [14,15,20] and the formation of a salt film [21–24]. The pit stability product describes the mass transport and critical chemistry inside pits as the determining factors for growth stability, whereas the salt film mechanism argues that only with an additional salt film at the corroding surface of the pit can stability be ensured.

Galvele developed a one-dimensional pit model based on numerical analysis of mass transport. [14,15,20] In his model, it was assumed that metal dissolution at the pit bottom is followed by hydrolysis of the metal cations, which leads to the acidification necessary to sustain pit growth. By considering the transport of ionic species in and out of the pit, he showed that a parameter called the pit stability product, $i*x$, could be used to determine pitting stability, where x is a one-dimensional pit depth, and i is the dissolution rate at the base of the pit. If $i*x \geq (i*x)_{crit}$, then the pit could maintain chemistry for propagation, and it would be stable. If at any time $i*x < (i*x)_{crit}$, the critical chemistry is lost by diffusion, and the pit will repassivate. The deeper a pit, the lower the current density is required at the base to maintain the acidic electrolyte which is needed to prevent repassivation. The pit stability product has been applied to other forms of localized corrosion including crevice corrosion and intergranular corrosion. Kehler discussed its use for determining conditions under which metstable pits within crevices can stabilize and then further coalesce to develop crevice corrosion [25].

Newman *et al.* discussed the kinetics of localized dissolution in a stainless steel, including the mass transport inside the pits, the formation of salt films, and their correlation to the critical pitting potentials [21–24]. They proposed that metastable pits can only survive and become stable with the precipitation of a salt film at the pit surface, where the growth of pits is under diffusion control. They made measurements using the artificial pit technique [21] to study the kinetics of pit propagation. The test was started by polarizing the sample to a high potential in order to grow the 1-D pit before slowly lowering the potential. The precipitation of a salt film on corroding surface results in a sudden drop in current, followed by recovery to the diffusion-limited value. As the potential is scanned to more negative values, the current density remains almost constant (Figure 1.4) until the transient occurs because as the pit growth control changes from diffusion control to ohmic/activation control. The linear relationship of depth and the reciprocal of the limiting current density, as shown in Figure 1.5, demonstrates the diffusion control at potentials on the plateau in Figure 1.4. A transition potential, E_t, was proposed to distinguish the two regimes of pitting growth. When the potential is above E_t, pit surfaces are salt-filmed, under diffusion control, and stable. The solution within the pit remains acidic enough to support growth and accommodate the extra potential from IR drop. When the potential is below E_t, the salt film dissolves. The pit is at first under ohmic control and by further lowing the potential pits grow with activation control. The ions are able to diffuse out of the pits in a rate higher than that of dissolution at the bottom surface of the corroding metal. The diluted electrolyte no longer supports stable pitting growth. The critical concentration for the formation of the salt film, given a constant transition potential E_t, can be calculated using a diffusion model. Although Al is not an active-passive metal like stainless steels, some reports by Beck *et al.* [26] indicated that a continuous aluminum chloride film may also form under artificial pit conditions where high concentrations of aluminum chloride are present at the pit base at high anodic potentials. Cook *et al.* [27] reported the observation of salt film at elevated potential while a potential dependent dissolution was observed near E_{rp}. They also pointed out the effect of the artificial pit dimension on the dissolution kinetics at the bottom of the pit with the concerns that pits with diameter >50μm are likely not fully activated even at the elevated potential to deliver accurate kinetics information. Accordingly, the artificial pit technique with a relative smaller size (<50μm) is expected to be useful for studying salt film effects and the dissolution kinetics in Al alloy systems in order to determine the critical conditions for stable pit growth.

The two theories mentioned above attempted to interpret the stability of pitting growth from the different perspectives. In spite of the different point of views, it is generally agreed that stable localized corrosion requires certain local chemistry and electrochemical conditions in the pit which lead to the local activation of the metal. The species concentration, current density, and potential associated with this critical condition are the controlling factors that ensure the stability of localized corrosion on a long-term scale. Lucente *et al.* [28–30] studied both the stability product i*x and E_{rp} for pure Al and Al-based alloys and confirmed the correlation between these two theories. Her work calculated the i*x by holding the artificial pit samples at a range of potential with which the diffusion control is generated. A significant drop in the magnitude of i*x occurred when the holding potential was lower than E_{rp}, (as shown in Figure 1.6) which confirms that the stability of the pit growth can be consistently determined by either of the theory. Investigating the underlying connections between the above theories will assist in better understanding of the fundamental controlling mechanism for pitting stability in the Al alloy system and providing predictive parameters for localized corrosion engineering structure.

1.2. Galvanically Induced Localized Corrosion

1.2.1.1. Galvanic Localized Corrosion between Al/Al Alloys and Noble Materials.

Galvanic interactions are important for the engineering applications in terms of the design for sacrificial anodes, the role of inclusions in localized corrosion, and in this study, for a coating upon an aluminum alloy for aerospace applications. Aluminum is one of the more active metals in the galvanic series [31], so is its alloy series. When it is coupled with the materials electrochemically noble to it, galvanic corrosion may occur. The electrons released through the dissolution reaction (equation 1.1) on the Al (anode site) are consumed by the noble materials (cathode site) through the oxygen reduction reaction (ORR) or hydrogen evolution reaction (HER) as shown in equation 1.2 and 1.3 [32].

$Al \rightarrow Al^{3}+ + 3e^{-1}$ Equation 1.1

ORR: $O_2+2H_2O+4e^{-1} \rightarrow 4OH^{-1}$ Equation 1.2

HER: $2H^{+1} + 2e^{-1} \rightarrow H_2$ Equation 1.3

1.2.1.2. Macro and Micro Galvanic Localized Corrosion of Al and Al Alloys

Macro galvanic corrosion has been extensively studied between Al and Al alloys with Zinc, Steel and Ceramics [33–37] . Accelerated corrosion rate varying with the coupling conditions on the Al site was observed. With the heterogeneous microstructure of Al Alloy, in particular for 2xxx and 7xxx series, it is susceptible to micro-galvanic corrosion, due to the noble local particle adjacent to Al matrix.[32,38,39] . In both cases, the nominal cathode-to-anode area ratio, the nature of the noble materials, electrolyte chemistry, and etc. are of importance to the localized corrosion propagation on the Al and Al Alloys.

1.3. Atmospheric Conditions

Many aerospace alloys are part of structures that are exposed to atmospheric conditions. Under atmospheric conditions, a thin layer of moisture exists on the metal surface. Despite the very low rate of uniform corrosion characteristic of passive materials, these materials can be susceptible to localized corrosion underneath the thin conductive layer [40,41].

1.3.1. Importance in practice

In the present study, a fastener geometry with a noble material coating is the focus. A practical situation of interest is the noble-material coated AA7075-T6 used in aerospace applications with an exposure to the various atmospheres. With the dissimilar materials interaction, accelerated galvanic corrosion is expected. The quantification of the rate and electrochemical kinetics and understanding of the controlling factors can provide insight for corrosion risk assessment and structural integrity improvement.

1.3.2. Challenges in the study of corrosion under atmospheric conditions

Unlike full immersion conditions, where the environmental parameters for corrosion can be easily adjusted independently, the parameters that control the localized corrosion under atmospheric conditions may be fixed by a given exposure environment. The chemistry of this thin layer is constrained by the type of the salts, temperature, and relative humidity [31,42]. The physical dimension of the thin layer is constrained by the relative humidity, type of the salt, and the loading density of salt. In addition, the limited thickness of the water layer restricts the mass transport including that of oxygen whose reduction is under diffusion control except for very thin films [42]. Challenges arise by the complication of solution composition and distribution on surface varying with time, as well as the limited ability to experimentally characterize the electrochemical kinetic on the corroding surface. These unique characteristics of atmospheric conditions will be considered in the present study in order to better address the corrosion behavior when an atmospheric condition is involved.

1.3.3. Defining variables of electrolyte

For a given exposure condition, the characteristics of the electrolyte layer are key controlling factors in atmospheric corrosion. The electrolyte layer character is determined by both the solution composition and the thickness of electrolyte. At a constant temperature, and with a given RH, salt concentration of the solution is fixed due to the thermodynamically equalization of the activities of water in the gas and solution phases. For example, the presence of 98%RH at room temperature requires a NaCl solution to be at 0.6M NaCl to attain equilibrium. If the concentration of the solution is higher than 0.6M, then that it will absorb water spontaneously from the surrounding gas phase until the equilibrium concentration, and vice versa. Similarly, 90%RH is equivalent to 2.8M NaCl solution at the room temperature.

The thickness of a uniform water layer is determined by the given loading density of the salt (g/m^2) and the concentration of the solution (g/m^3). In the experiments, with a constant exposed area, a volume for a target electrolyte layer thickness is thereby able to be determined.

1.3.4. Galvanically-induced localized corrosion under atmospheric conditions

The studies for the localized galvanic corrosion under atmospheric conditions using both experimental and computational approaches, with various geometry including fastener geometry have been reported [41,43–48]. The challenge is caused by the complication of the environment-dependent exposure conditions and the limited approach of quantifying the electrochemical information from the corroding surface.

Studies of the factors controlling wetness have been conducted by Cole *et al.* [49], Schindelholz *et al.*[50], and Risteen *et al.*[51] to understand the controlling process of salt deposition and solution distribution for atmospherically-exposed surface. On the other hand, the capability of Scanning Kevin Probe (SKP) to measure the electrochemical potential of corroding surface under thin electrolyte layers has been demonstrated by the work of Stratmann[67], which provides a channel to connect the electrochemical kinetics of atmospheric conditions to full immersion conditions, where the measurement of electrochemical characteristics is easy to perform. Although very little work on the predication of the localized corrosion stability under atmospheric conditions has been reported, the work above has provided a foundation for the potential prediction if an electrochemical stability criterion is given. The present work therefore focuses on discussing the feasibility of predicting the localized corrosion stability for the atmospheric condition with the introduction of corrosion stability criteria.

1.4. Modeling of localized corrosion

It is generally agreed that experimental measurements of the corrosion behavior inside crevices and pits is difficult, due to the micron-scale sizes and their dynamic nature. Modeling thus becomes a powerful tool in terms of predicting the initiation and propagation of the localized corrosion. The basic framework of modeling of localized corrosion and its extension to atmospheric conditions are discussed as below.

1.4.1. General concepts for modeling localized corrosion.

In the early modeling of localized corrosion, the Finite Element Analysis (FEA) method was introduced for the numerical modeling of localized corrosion [52–56]. Sharland *et al.* [54,55] sought to calculate the distribution of potential, current, and chemical species inside an occluded region during crevice corrosion. In their model, the FEA method was used to solve the complex set of mass-conservation equations. The chemical reactions (*i.e.*, the anodic dissolution of metal ions at anodic sites, the reduction of oxygen at cathodic sites, and the hydrolysis of metal ions in the crevice solution), mass transport of chemical species through diffusion and electromigration, and the time evolution of the solution chemistry were considered. Recently, advanced FEA software allows finer meshing and the use of more complicated (and relevant) electrochemical boundary conditions. More sophisticated models thus have been proposed to simulate more complicated conditions [57–62]. The parameters in the models, such as species concentration, the potential distribution and current density and the impacts from the environmental changes (geometry, boundary conditions, etc.) can be calculated, including the time dependence. For example, in Xiao *et a.l*'s model [62], the effect of pit morphology and size, and microstructure of the Al alloy on the rate of pit growth were investigated to predict the time-dependent damage evolution caused by pitting and micro-galvanic corrosion. These models above have been validated in simple systems and have produced results in qualitative agreement with observed trends in most of the cases studied [54,55,62]. Thus, it seems reasonable to extend these methodologies and concepts to the study of galvanically-induced localized corrosion.

1.4.2. Modeling for Atmospheric conditions.

Most modeling of localized corrosion assumes that the material is fully immersed and its surface is held at a constant potential. Under full immersion conditions, the cathode is often very large relative to the anode and the ohmic resistance between these two is limited. Thus, the behavior of the anode controls the ability for propagation of corrosion. Under atmospheric conditions, the interaction between the anode and cathode is mitigated by the ohmic drop between the various parts of the cathode and the corroding anode site. Thus, the environmental parameters, such as the characteristics of the electrolyte layer on the external cathode, the distance and area ratio for cathode/anode, and the interfacial electrode kinetics will have a strong impact on the stability of the localized corrosion [40,41,44,45,63,64]. Chen *et al.* [40,41] constructed an analytical framework to obtain the bounding condition for the stability of localized corrosion under atmospheric conditions by considering the influences of external cathode, the anode, and the electrolyte layer. Using the Galvele stability criterion, they showed that in order to maintain the critical chemistry at the corroding surface site, the anode must sustain a sufficiently high dissolution rate ($I_{LC,min}$)

while the external surface must act as a cathode to supply the current (I_{cath}) needed by the anode. Similarly, Proust et al.[65] used a threshold pH Value to determine the corrosion stability of the crevice in his modelling work.

These modeling works provide an example of framework to the quantify compatibility criteria between anode and cathode where the localized corrosion can be stabilized. By introducing the corrosion stability criteria to the galvanic corrosion modeling, such approaches can be adopted into the present study in order to predict the cathode-to-anode combination that should be avoided to ensure long-term stability of a structure.

1.4.3. Modeling of galvanically-induced localized corrosion under atmospheric conditions

Limited computational modelling work has been applied to the galvanic interaction with atmospheric conditions. The effect of electrolyte thickness on the anodic current distribution of magnesium and steel with aluminum spacer through numerical method was investigated by Deshpande[66]. Mizuno and Kelly [36, 37] developed a modelling frame work to predict the corrosion damage of 5xxx series Aluminum alloy by connecting the corrosion damage with the applied electrochemical potential of the corroding surface. The generation and distribution of corrosion products with given NaCl concentration were modeled by Okada *et al.*[69] and validated by the experimental data from FTIR. Micro-Galvanic interaction was studied by Murer[59] and Desphande[57] and validated by the experimental data attained from microelectrode techniques[59]. However, a detailed computational study for a galvanic system of an aluminum alloy and noble materials with a complex geometry has not been performed. The feasibility of using modelling to predict the effect of engineering design (such as the dimension of the geometry, the cathode-to-anode area ratio), and the environmental condition (such as the solution concentration, electrolyte layer thickness) on the galvanic interaction is thus emphasized in the present study.

Reference:

[1] F. Andreatta, H. Terryn, J. H. . de Wit, *Electrochim. Acta* 2004, *49*, 2851.

[2] http://www.corrosionist.com/Aluminum_ Galvanic_Corrosion.html.

[3] P. O. Acevedo-Hurtado, P. A. Sundaram, *Corros. Sci.* 2008, *50*, 3123.

[4] J. R. Davis, in *Corros. Alum. Alum. Alloy.*, ASM International, 1999, p. 110.

[5] N. Perez, in *Electrochem. Corros. Sci.*, Springe, 2004, p. 155.

[6] Z. Szklarska-Smialowska, *Corrosion Science* 1999, *41*, 1743–1767.

[7] G. S. Frankel, *J. Electrochem. Soc.* 1998, *145*, 2186.

[8] E. McCafferty, in *Introd. to Corros. Sci.*, Springer, 2010, pp. 263–281.

[9] S. Maitra, G. C. English, *Met. Trans. A* 1981, *12*, 535.

[10] N.Birbilis, *Mater. Sci. Forum* 1997, *247*, 1.

[11] Y. Shi, R. G. Kelly, *ECS Transctions* 2012, *41*, 155.

[12] G. S. Frankel, *Mater. Sci. Forum* 1997, *247*, 1.

[13] G. S. Frankel, *J. Electrochem. Soc.* 1996, *143*, 1834.

[14] J. Galvele, *Corros. Sci.* 1981, *21*, 551.

[15] J. R. Galvele, *Journal of The Electrochemical Society* 1976, *123*, 465.

[16] B.E.Wilde, E.Williams, *J. Electrochem. Soc.* 1971, *118*, 1057.

[17] B. E. Wilde, R.W.Staehle, in *NACE Conf.*, 1974, p. 342.

[18] D. S. Dunn, N. Sridhar, G. A. Cragnolino, *Corrosion* 1996, *52*, 115.

[19] D. S. Dunn, G. A. Cragnolino, N. Sridhar, *Corrosion* 2000, 90.

[20] B. Aires, *Corrosion Sci.* 1984, *24*, 517.

[21] N. J. Laycock, R. C. Newman, *Corros. Sci.* 1997, *39*, 1771.

[22] R. C. Newman, *Corrosion Sci.* 1985, *25*, 341.

[23] M. H. Moayed, R. C. Newman, P. Centre, *Corrosion Sci.* 1997, *39*, 1133.

[24] G. T. Gaudet, W. T. Mo, T. a. Hatton, J. W. Tester, J. Tilly, H. S. Isaacs, R. C. Newman, *AIChE J.* 1986, *32*, 949.

[25] B.A. Kehler, M.S Thesis, University of Virginia, 1999.

[26] T. R. Beck, N. W. Way, *Electrochimica Acta* 1983, *29,4,485.*

[27] A. B. Cook, D. L. Engelberg, R. C. Newman, *ECS Transctions*, 2012, *41,25, 121.*

[28] A. M. Lucente, J. R. Scully, *J. Electrochem. Soc.* 2008, *155*, C234.

[29] A. M. Lucente, J. R. Scully, *Corros. Sci.* 2007, *49*, 2351.

[30] A. M. Lucente, J. R. Scully, *Electrochem. Solid-State Lett.* 2007, *10*, C39.

[31] Denny A. Jones, *Principles and Prevention of Corrosion*, Prentice-Hall, Inc, 1996.

[32] Q. Meng, G. S. Frankel, *J. Electrochem. Soc.* 2004, *151*, B271.

[33] D. A. Jones, B. E. Wilde, *Corrosion Sci.* 1978, *18, 631*

[34] D. S. Keir, M. J. Pryor, P. R. Sperry, *J. Eletrochem. Soc.* 1965, *114*, 777.

[35] L. H. Hihara, R. M. Latanision, *Corrosion*, 1992, 48,7, 547.

[36] D. Mizuno, R.G. Kelly, Corrosion, submitted (Aug, 2012).

[37] D. Mizuno, R.G. Kelly, Corrosion, submitted (Aug, 2012).

[38] J. O. Park, C. H. Paik, Y. H. Huang, R. C. Alkire, *J of The Eletrochemical Society*, 1999, *146*, 517.

[39] R. G. Buchheit, R. K. Boger, M. C. Carroll, *JOM*, 2001, 29.

[40] Z. Chen, F. Cui, R. G. Kelly, *ECS Trans.* 2007, *3*, 443.

[41] Z. Y. Chen, F. Cui, R. G. Kelly, *J. Electrochem. Soc.* 2008, *155*, C360.

[42] T. E. G. Christofer Leygraf, *Atmospheric Corrosion*, Wiley-Interscience, 2000.

[43] F. J. Presuel-Moreno, M. a. Jakab, J. R. Scully, *J. Electrochem. Soc.* 2005, *152*, B376.

[44] Z. Y. Chen, R. G. Kelly, *J. Electrochem. Soc.* 2010, *157*, C69.

[45] F. Cui, F. J. Presuel-Moreno, R. G. Kelly, *Corros. Sci.* 2005, *47*, 2987.

[46] R.-G. Hu, S. Zhang, J.-F. Bu, C.-J. Lin, G.-L. Song, *Prog. Org. Coatings* 2012, *73*, 129.

[47] I. S. Cole, W. D. Ganther, S. a. Furman, T. H. Muster, a. K. Neufeld, *Corros. Sci.* 2010, *52*, 848.

[48] Z. Feng, G. S. Frankel, *Corrosion,* 2014, *70*, 95.

[49] I. S. Cole, W. D. Ganther, J. D. Sinclair, D. Lau, D. a. Paterson, *J. Electrochem. Soc.* 2004, *151*, B627.

[50] E.Schindelholz, R.G. Kelly, *Corros. Rev.* 2012, *30*, 135.

[51] B.E.Risteen, E.Schindelholz, R.G. Kelly*, ECS Transctions,* 2014, *58*, 1.

[52] John W Oldfield, in *NACE Int. Annu. Conf. Expo.*, 1996, p. 512.

[53] R.W.Evitts, in *NACE Annu. Conf. Corros. Show*, 1992, p. 75.

[54] S.M.Sharland, *Corros. Sci.* 1992, *33*, 183.

[55] S.M.Sharland, *Corros. Sci.* 1988, *28*, 621.

[56] S.M.Sharland, *Corros. Sci.* 1987, *27*, 289.

[57] K. B. Deshpande, *Electrochim. Acta.* 2011, *56*, 1737.

[58] F. Thébault, B. Vuillemin, R. Oltra, K. Ogle, C. Allely, *Electrochim. Acta* 2008, *53*, 5226.

[59] N. Murer, R. Oltra, B. Vuillemin, O. Néel, *Corros. Sci.* 2010, *52*, 130.

[60] M. Verhoff, R. Alkire, *J. Electrochem. Soc.* 2000, *147*, 1349.

[61] O. Guseva, P. Schmutz, T. Suter, O. von Trzebiatowski, *Electrochim. Acta* 2009, *54*, 4514.

[62] J. Xiao, S. Chaudhuri, *Electrochim. Acta* 2011, *56*, 5630.

[63] R. Kelly, F. Cui, F. Presuel-Moreno, *ECS Trans.* 2006, *1*, 17.

[64] F. Cui, F. J. Presuel-moreno, R. G. Kelly, *Corrosion Sci.* 2005, *47,* 2987.

[65] A. Proust, G. Girardin, B. Vuillemin, P. Combrade, R. Oltra, COMSOL Conference, 2006.

[66] K. B. Deshpande, *Corros. Sci.* 2012, *62*, 184.

[67] M. Stratmann, H. Streckel, *Corros. Sci.* 30, 1990, *6/7*, 697

[68] N. Okada, M. Matsumoto, K. Nishihara, M. Kimoto, T. Kudo, S. Fujimoto, *ISIJ International.* 2010, *50, 5* 743

[69] Ashely Lucente, PhD Dissertation, University of Virginia, 2008

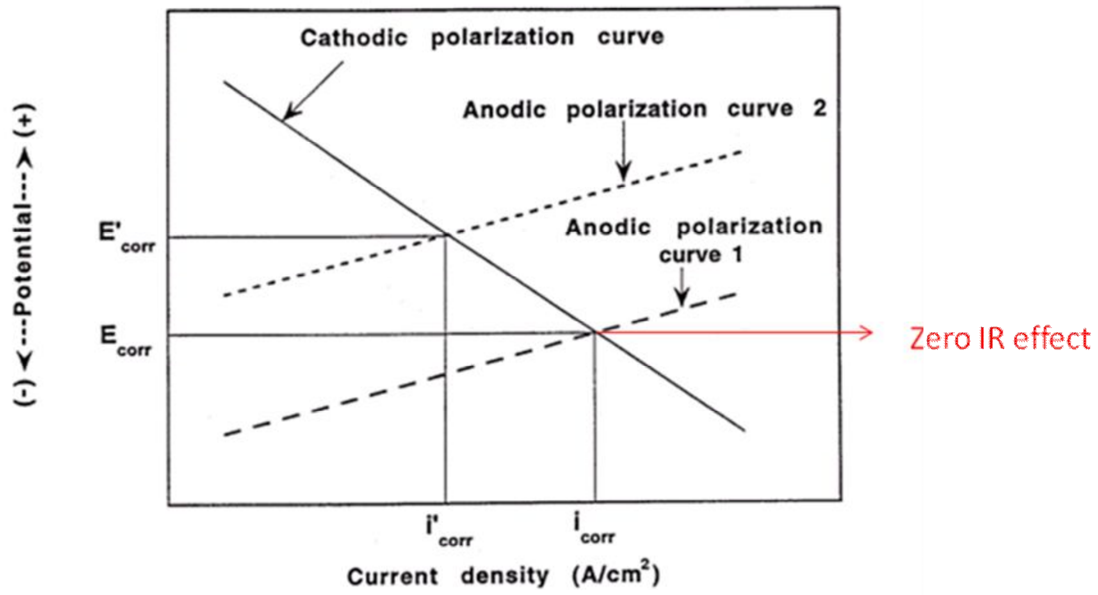

Figure 1.1: Schematic demonstration of mix potential theory and the effect of IR ohmic drop

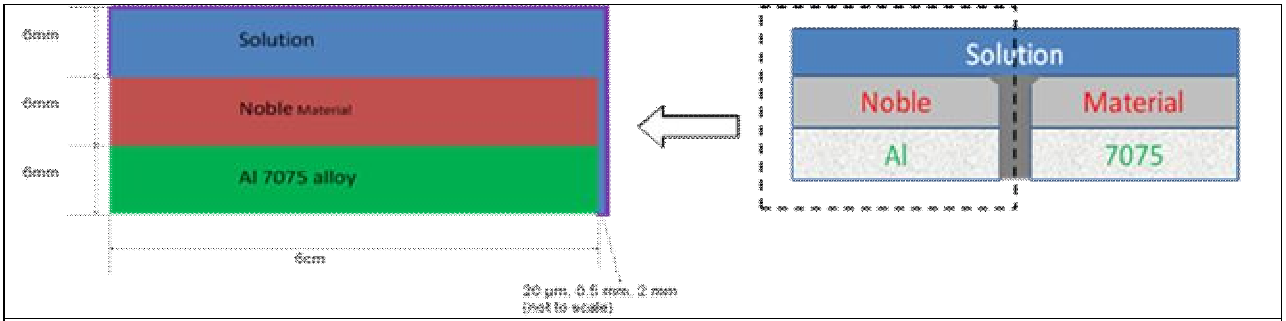

Figure 1.2- Fastened joint geomerty of AA7075-T6 and noble materials coupled system

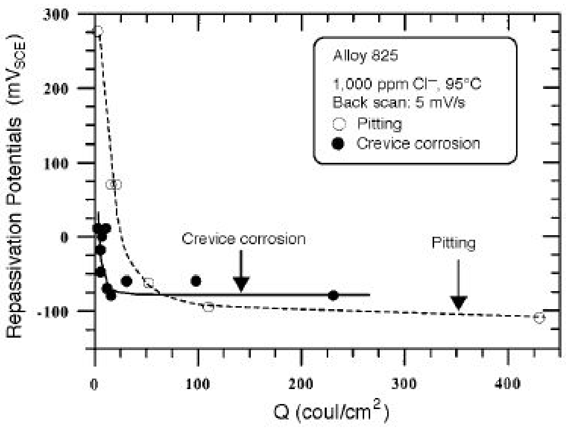

Figure 1.3-a: The E_{rp} vs charge density for Alloy 825 in 1000ppm [Cl$^-$] at 95^{o}C held at 100mV below E_{rp}[18]

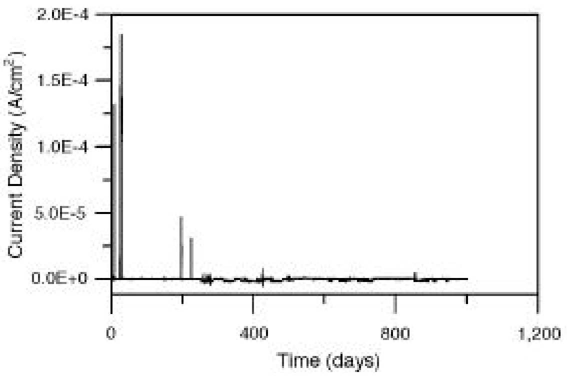

Figure 1.3-b: The current density for Alloy 825 in 1000ppm [Cl$^-$] at 95^{o}C held at 100mV below E_{rp}[19]

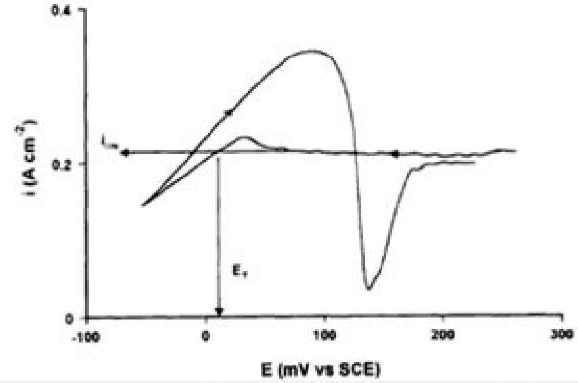 	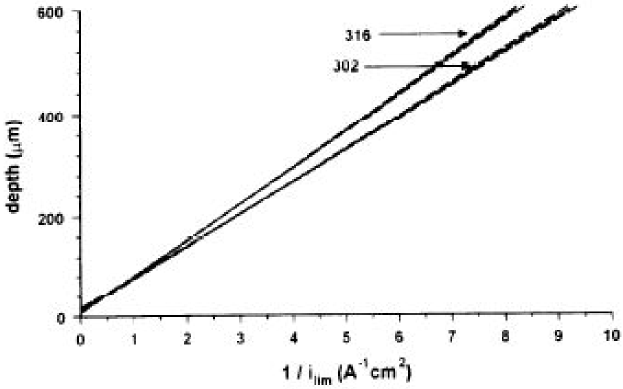
Figure 1.4: Current Density vs Potential during potential sweep experiment for a 50um diameter, 302 SS artificial pit in 0.1M NaCl, showing the definition of E_T. [21]	Figure 1.5: Pit depth plotted against the reciprocal of the limiting current density for 302 and 316 SS 50um diameter aterifical pits grown under diffusion control in 1M NaCl[21]

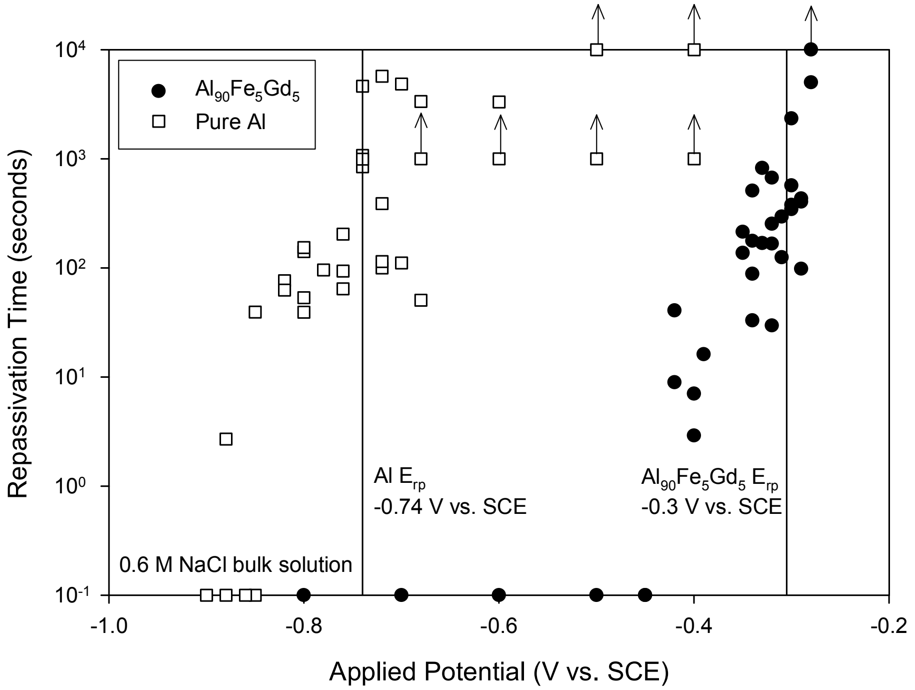

Figure 1.6: Plot of repassivation time with respect to applied potential for amorphous $Al_{90}Fe_5Gd_5$ and high purity polycrystalline Al. In each case the potential was held at +1 V vs SCE for 1000 seconds prior to stepping to the given potential. Bulk solution 0.6 M NaCl. [69]

Chapter 2: The stability criteria for localized corrosion of AA7075

The chapter discusses the controlling mechanism of the localized corrosion of AA7075 and quantifies the criteria that can be used to predict its stability. Two criteria, E_{rp} and i*x were measured. The effectiveness of E_{rp} was verified by current decay tests. The artificial pit technique was used to determine the value of i*x assuming pit propagation kinetics in one dimension. The correlation between E_{rp} and i*x was discussed.

2.1. General Introduction

2.1.1. Background: Two stability criteria: Repassivation Potential E_{rp} and Stability Product i*x

In this chapter, the stability criteria for AA7075-T6 in a given salt solution were sought, and measured. As discussed in Chapter 1, two criteria, the repassivation potential E_{rp}[1–3] and Galvele's pit stability product i*x [4–7] have been used to determine and predict the conditions under which the corrosion propagation is stabilized. The repassivation potential and the i*x stability products for AA7075 and Pure Al in salt solution were measured via different techniques from previous research [8–13]. The connections between E_{rp} and i*x of pure Al was also established by Lucente and Scully's work using artificial pit sample[10] .

For both criteria, it is commonly agreed that an aggressive acidified local chemistry with high salt concentration is required to support the growth of pits for the stable corrosion propagation. The required salt concentration of the pit solution was investigated by Newman and Alkire *et al.* [14,15]. It was found in single-pit Al alloy samples that the experimentally measured current density was in quantitative agreement with its calculated value with which the corrosion rate was controlled by the dissolution of a salt film under the mass transport limited condition. Beck [15] further confirmed the existence of a salt film from polarization tests on an Al electrode in saturated $AlCl_3$. By polarizing the Al alloy in the $AlCl_3$ solution, he observed a current density peak that indicate the formation and dissolution of AlCl3 salt film. By calculating the concentration using the measured current density, he comfirmed that a continuous $AlCl_3$ film formed when the $AlCl_3$ concentration was greater than 80% of saturation, which required high anodic potentials.

2.1.2. The scientific question to be answered in this chapter.

From the above literature, the question of the mechanism of the pit growth stability of AA7075-T6 remains open. The present research attempts to 1) determine the values of the stability criteria of AA7075-T6 and 2) unite the above different theories to clarify the controlling mechanism of the pit growth stability in the alloy. The following research was carried out in order to meet the goals:

1) Determine E_{rp} of AA7075-T6 in 0.6 M NaCl and examine the existence of a plateau of E_{rp} at large charge densities;
2) Validate the effectiveness of the measured E_{rp} to predict localized corrosion stability under prolonged exposure to aggressive environments;
3) Quantify i*x, the stability products on AA7075-T6 in the salt solution. Specifically, the current density and the critical fraction of solution saturation to sustain the pit growth is sought;
4) Examine the implicit correlation among E_{rp}, and i*x.

2.1.3. Approaches in general used to solve the problem

The general approaches used to solve the question above in section 2.1.2. are described below. . The details of the experimental methods are described in section 2.2.

1) E_{rp} of AA7075-T6 was determined by using the plateau value from potential vs accumulated charge density plots. Samples were potentiostatically held at various applied potentials to generate different accumulated charges and then polarized down until below open circle potential (OCP) .The target potential from downward polarization curve was selected with a given threshold current density.
2) i*x of AA7075-T6 was measured via artificial pit technique which allows the accurate calculation of pit depth assuming 1-D diffusion and Faraday's law.
3) The dissolution kinetics as well as the critical fraction of solution striation to sustain the pit growth were determinedvia potentiodynamic scanning of artificial pit samples in $AlCl_3$ solutions of different levels of saturation.

2.1.4. The brief summary of the results

In this chapter, the E_{rp} of AA7076-T6 in 0.1M and 0.6M NaCl solution were determined for both bulk sample and artificial pit samples. The effectiveness of E_{rp} was validated through current decay tests of artificial pit samples with prolonged exposure at various anodic potentials above and below E_{rp}. The value of i*x for AA7075 in 0.6M NaCl was determined by using 25um-diameter artificial pit samples. The effects of the local cathodic current at the pit surface were considered. Results were also compared with the ones of Pure Al and literature. The connection between E_{rp} and i*x was established and discussed.

Finally, the dissolution kinetics on the corroding surface of artificial pits as a function of the degree of saturation of $AlCl_3$ are used to determine the critical solution needed to support stable corrosion growth inside pits. It was found that about 80% of saturation is required to support a high level of current density, i.e. a high corrosion rate inside the pit.

2.2. Experimental Methods

2.2.1. Materials

2.2.1.1. Materials Composition and Geometry

Rolled AA7075-T6 sheet (0.5cm thick) and AA7075 (hard temper) fine wire, and Pure Al (99.0+ %) fine wire were used in this study. The composition of rolling sheet and fine wire samples of AA7075 is shown in Table 2. 1

The rolling sheets of AA7075-T6 were used for bulk sample testing. The dimension of the rolling sheet samples was 2.5cm x 2.5cm x 0.5cm and rolling direction is shown in Figure 2. 1. The fine wire with 25μm diameter was used for artificial pit sample testing. The microstructure of fine wire samples of AA7075 via SEM are showed in Figure 2. 2.

2.2.1.2. Specimen Preparation

The rolled sheets of AA7075-T6 were mounted in epoxy with the LS surface exposed, then polished with sand paper to 800 grit and cleaned with methanol before any exposure to the solution.

Pure Al wire and AA7075 wire, 25μm in diameter, were mounted in epoxy as shown in Figure 2. 3. The cross-section of the wire constitutes the sample surface on the one end, and the wire is connected to an insulated wire on the other end to serve as an electrical connection. The mounted samples were polished with sand paper to 800 grits and cleaned with methanol before any exposure to the solution.

2.2.2. Solutions

Two types of solutions were used for the work presented in this chapter. To simulate the bulk solution as the external environment, 0.6 M NaCl and 0.1M NaCl were prepared. $AlCl_3$ solutions with a range of saturation (100%, 80%, 60% and 40%) were prepared to simulate the acidic pit solution.

Deionized water was used for solution preparation. For all the solutions, room temperature with aerated and quiescent condition was applied.

2.2.3. Apparatus

A Gamry Potentiostat was used for electrochemical signals controlling and processing.

2.2.3.1. Flat Cell Set Up

A glass corrosion cell was used for all the bulk sample full immersion electrochemical tests. It allows up to three electrodes in the system. The schematic illustrations are shown in Figure 2. 4. The bulk sample is fixed on the one end of cell with a constant exposure area ($1cm^2$). It served as the working electrode. A platinum grid is fixed on the other end of cell as the counter electrode. A Saturated Calomel Electrode (SCE) was used as the reference electrode. These three electrodes were connected to Gamry Potentiostat. During the test, the solution is filled in the body of flat cell. The electrochemical signals are controlled, monitored and acquired by Gamry Potentiostat.

2.2.3.2. Beaker Cell for Full Immersion Test

To measure the electrochemical characteristics inside a single pit, artificial pit sample was immersed in a 500mL beaker with the selected electrolyte solution. The surface of the wire was upward. A Pt counter electrode and SCE reference electrode were set at the other end of the beaker to form a three-electrode cell system. The details of the setting are shown in Figure 2. 5. All the artificial pit samples in this study were tested in this system.

2.2.4. Procedures

2.2.4.1. Potentiodynamic Scans of E_{rp} for Artificial Pit and Bulk Samples

2.2.4.1.1. Bulk Sample Measurement

Bulk samples of AA7075 were used in this measurement. The exposure surface is LS, the edge of the plate. The bulk samples of AA7075 were immersed in a flat cell with sodium chloride solution (0.1M NaCl or 0.6M NaCl). A potential well above the pitting potential was applied to generate a defined pit depth. Various accumulated charges were generated by the varying the holding time and the holding potential. Six holding potentials (vs. SCE): -0.35V, -0.4V, -0.5V, -0.6V,-0.65V were selected with the holding time varying from 30sec to 12hrs. After the pits were generated, the potential was scanned towards more negative potentials with a scanning rate of 0.5mV/s. A Gamry Potentiostat PCI-4 was used to control the potential/current for the above tests. The E_{rp} value was identified as that potential at which the current density was just below 250 μA/cm^2.

2.2.4.1.2. Artificial pit sample measurement

E_{rp} measurements were conducted on artificial pit samples using the same method as in section 2.2.4.1.1. The artificial pit with an inert epoxy wall forms and grows under 1-D diffusion control. Multiple pits are thus avoided and only the behavior of the active pit surface is monitored. The charge density therefore can be translated into the depth of pit directly according to Faraday's law.

2.2.4.2. Potentiodynamic scans for i*x for both Al and AA7075

Artificial pit samples of Pure Al and AA7075 wire with 25μm diameter were used for this measurement. Samples were immersed in a beaker with 0.6M NaCl and polarized to +1V (vs SCE) for 1020 seconds. A fast scanning rate (25mV/s) was then applied to lower the potential (vs SCE) to different levels of potential for potentiostatic scanning (from -0.3V to -1V (vs SCE)). Samples were held at each holding potential for 100 seconds respectively. The applied current was recorded by Gamry potentiostat and converted into accumulative charges. The depth of pit (x) at the holding potential was calculated by Faraday's Law. The i*x at the certain potential level was thus equal to the average current density (i) at the level of holding potential multiplied by the calculated depth (x).

2.2.4.3. Local cathodic current measurements

In order to calculate the i*x of artificial pit sample more precisely, the local cathodic current must be taken into account. The proportion of cathodic current of both pure Al and AA7075 was quantified on artificial pit samples. The samples were held in 0.6M NaCl at 1V (vs SCE) for 1000sec. The recorded current density was converted into pit depth via Faraday's Law. Cross-sectioning and optical microscopy examinations were performed immediately after the exposure to measure the actual depth of the corroded pit. The effect of local cathodic current was then determined by comparing the calculated depth and the actual depth. More details of the results are discussed in 2.4.1.

2.2.4.4. Current decay measurements

Artificial pit samples of both Pure Al and AA7075 wire with 25μm diameter were used for this measurement. The solution used here was 0.6M NaCl. Samples were held at -0.2V to 0V (vs SCE) for 30 minutes to generate a pit with depth >100 um. The potentials (vs SCE) were then stepped down to a range from -0.3V to -0.95V (vs SCE). For each potential level, the sample was held for >100000seconds. Current was monitored during the entire potentiostatic hold. The change of current over the time was plotted for the further discussion.

2.2.4.5. Anodic kinetics in simulated pit solutions

Artificial pit samples of AA7075 were immersed in the pit solution simulants to study the dissolution kinetics at the bottom of the pits. Two types of solutions were used to simulate the pit chemistry in the pure Al and AA7075, respectively. For the pure Al, $AlCl_3$ solution was used with a saturation of 100%, 80% 60% and 40%. For AA7075, additional of $MgCl_2$, $CuCl_2$, $ZnCl_2$ was added into $AlCl_3$ solution with a saturation of 100%, 80% 60% and 40%. The amount of

$MgCl_2$, $CuCl_2$, and $ZnCl_2$ is proportional to the alloying atomic weight percentage of Mg, Cu and Zn in AA7075.

The polarization scanning started 1V (vs SCE) with a scanning rate of 0.5mV/s until -1V vs SCE. E-Log(i) curves were plotted for the further discussion.

2.3. Results: The E_{rp} Measurement

2.3.1. E_{rp} Measurement for Bulk and Artificial Pit Samples

Repassivation potential (E_{rp}) measurements were conducted for both bulk and artificial pit samples of AA7075 in 0.1M and 0.6M NaCl solution under the full immersion condition. The samples were held at a potential well above the OCP for various lengths of time in order to accumulate different charges (depths) and then scanned down below the OCP. The detailed experimental process was described in the section 2.2.

Figure 2. 6, Figure 2. 7, Figure 2. 8, and Figure 2. 9 show the polarization curves for both bulk and artificial pit samples during the potentiodynamic scans after the potentiostatic holding at the various potentials. In order to identify E_{rp}, two sets of threshold current density, $50\mu A/cm^2$ and $250\mu A/cm^2$ were selected as the criteria. $50\mu A/cm^2$ is known as a threshold widely used by Dunn and Sridhar [2] in their research of stainless steel. In this research, E_{rp} was identified by using the higher current density criteria ($250\mu A/cm^2$) because this given E_{rp} is closer to the transition potential observed from i*x measurement as well as the results from current decay measurement. More details are discussed in the section 2.4 and 2.5.

Figure 2. 6 and Figure 2. 7 show the results for 0.6M NaCl solution. The polarization curve of artificial pit sample is shown in Figure 2. 6. The measured E_{rp} of artificial pit sample is -0.85V vs SCE given 50μA/cm^2 and -0.90V vs SCE given 250μA/cm^2. In Figure 2. 7, the E_{rp} for bulk sample is similar, measured as -0.89V for 50μA/cm^2 and -0.85V for 250μA/cm^2. Figure 2. 8 and Figure 2. 9 show the results in 0.1M NaCl solution. In Figure 2. 8, the E_{rp} for artificial pit sample is -0.84V and -0.80V for 50μA/cm^2 and 250μA/cm^2, respectively. In Figure 2. 9, the E_{rp} for bulk sample is -0.82V and -0.75V for 50μA/cm^2 and 250μA/cm^2, respectively.

Figure 2. 10 shows the variation of E_{rp} as a function of the accumulated charge for both bulk samples and artificial pit samples for the 250μA/cm^2 criterion for E_{rp} determination. The effect of [Cl^-] is also presented in the figure. For bulk samples in 0.1M NaCl (black squares), the E_{rp} first decreases as the charge density increases. Above a charge density of 10 C/cm^2, the value of the E_{rp} appears to plateau at approximately -0.73V to -0.80V (vs SCE). This type of E_{rp} versus charge density relationship is consistent with the observations on localized corrosion of stainless steel by Dunn and Sridhar[2]. For bulk samples in 0.6M NaCl solution (orange triangles), a similar trend is observed, although with a lower bound for E_{rp} at a range of -0.82V to -0.94V (vs SCE). The lower bound of E_{rp} decreased with the increase of [Cl^-]. A similar effect of [Cl^-] was also observed in the work of Dunn and Sridhar [2]. Because bulk samples are used, the total charge cannot directly be translated into the pit depth as the dissolution is highly non-uniform across the exposure surface. The data measured from artificial pits samples are also shown in Figure 2. 10. As shown in the Figure 2. 10, the range of E_{rp} measured from artificial pit samples fell into the same range of the results for bulk sample measurement.

Figure 2. 11 shows the E_{rp} as a function of charge density given 50μA/cm^2 criteria. The range of lower bounds for both 0.1M NaCl and 0.6M NaCl are somewhat lower than the ones shown in Figure 2. 10. For 0.1M NaCl, the lower bound for E_{rp} ranged from -0.78V to -0.85V vs SCE. For 0.6M NaCl, the lower bound for E_{rp} ranged from -0.89V to -0.99V vs SCE.

2.4. Results: x*i Measurement

The other stability criterion, x*i, was caculated from measurements using the artificial pit technique as described in section 2.2. An artificial pit sample was first held at an elevated potential (1V (SCE)) to generate a pit with depth ≥ 100μm which took 1,020 secs. The potential was then scanned down to a lower potential at which a potentiostatic test was performed for 100sec. The pit depth and the current density at each holding potential were used for x*i calculation.

2.4.1. Faraday's Law and Local Cathodic Current for artificial pit samples

Faraday's law was used here to convert the current density over the exposure time to the mass loss and then to the depth of the 1-D pit for the artificial pit samples. The equations,

$m= It(A.W.)/nF$ Equation 2.1

$d=m/D/\pi r^2$ Equation 2.2

Where, *m*=mass loss (grams), I=current (amps), t= time (sec), A.W. = atomic weight (grams/mole), F=Faraday's constant (96,498 coulombs/equivalent), d=depth of artificial pit, D=density of materials (g/cm^3), and r=radius of wire, were used in this study. Table 2. 3 shows the parameters used for both pure Al and AA7075.

The effects of local cathodic current were also considered throughout section 2.4 to precisely calculate the i*x value. For the artificial pit sample, a cathodic reaction is likely to occur at the dissolving surface. The measured current density from Gamary potentiostat is therefore the difference between anodic current and cathodic current. In order to calculate the actual pit depth, x, the effect of local cathodic current need to be eliminated, as only anodic current contributed to the pit depth growth. The experimental method was described in section 2.2.

Table 2. 3 shows the parameters used to calculate the percentage of local cathodic current. The calculated depth, d_c is the depth calculated from current density-exposure time curves using Equation 2.1 and 2.2. The measured depth, d_m was measured from the cross-sectioned surface of artificial surface after the exposure. The percentage of local cathode $p_{cathodic}$ was calculated by $(d_m - d_c) / d_m$. For AA7075, the average $p_{cathodic}$ is 11% and for pure Al, the average $p_{cathodic}$ is 14%, which compare well with the results from the previous study[10]. Both of the results were applied to correct the i*x reported in this study.

Figure 2. 12 to Figure 2. 15 show detailed examples of how d_c and d_m were measured.. Figure 2. 12 and

Figure 2. 13 show the calculated depth, d_c and cross-sectioned surface of AA7075 artificial pit wire samples after 1000secs exposure. A value of d_c of 234μm was attained from the current density-time plots in via Equation 2.1 and Equation 2.2. A value of d_m of 267 μm was measured according to

Figure 2. 13. Similarly, Figure 2. 14 and Figure 2.15 show the d_c (227μm) and d_m (266μm) for Pure Al samples.

2.4.2. Current vs time of potentiostatic test at 1V (vs SCE) for both Al and AA7075 artificial pit samples.

The artificial pit samples were held at 1V (vs SCE) for 1020sec for the purpose of generating a deep pit. As shown in Figure 2. 16, both AA7075 and Pure Al samples were tested. The current density of AA7075-T6 reaches a peak at the first 20 sec at a value of 8A/cm^2, then decreased with the time and stabilized at 1A/cm^2 after 200secs. For pure Al, the trend of the current density is similar. The peak current density is slightly higher (12A/cm^2), but the stable current density after 20 secs is lower than found for AA7075. The charge density from integration of current density over the time were converted into pit depth with the given diameter by using equation 2.1 and 2.2. Two examples of depth vs time curves are shown in Figure 2. 17. For AA7075, the overall charge density at the end of the test shown in Figure 2. 16 is 1,132 C/cm^2, which is equivalent to a pit depth of 391μm according to Faraday's law. For pure Al the overall charge density at the end of the test shown in Figure 2. 16 was 643 C/cm^2 , which is equivalent to a pit depth of 227μm. The differences between the pit depths for AA7075 and pure Al after an equivalent time of dissolution at high potential may indicate a more soluble salt film on the corroding surface of the AA7075 during dissolution. The results of repeated potentiostatic testing held at 1V vs SCE for both AA7075 and Pure Al artificial samples are shown in Figure 2. 18. As shown in the Figure 2. 18, at the initial 200secs, AA 7075 has higher current density, i.e., higher dissolution rate to support the pit growth, while some fluctuations were observed for Pure Al samples.

2.4.3. Current vs Time of the potentiostatic test with lower holding potential (-0.3V to -0.9V SCE) for both pure Al and AA7075 artificial pits samples

After holding at 1V (vs SCE), the artificial pit samples were polarized down to a lower potential for a 100sec potentiostatic test. A scan rate of 25mV/s was used to retain the critical chemistry inside the pit. The holding potential is ranged from -0.3V to -0.9V (vs SCE). Examples of current density vs. time at different holding potentials are shown from Figure 2. 19 to Figure 2. 29. Figure 2. 19 to Figure 2. 24 show the current density vs time for AA7075 at the holding potentials of -0.3Vto -0.8V (vs SCE). The current density fluctuates somewhat during the holding time, but decreases with the decrease of the potential. In Figure 2. 19, at -0.3V, the fluctuation range is 0.18 A/cm^2 to 0.32 A/cm^2. In Figure 2. 20 and Figure 2. 21, at -0.4V and -0.5V, the fluctuation range is 0.12 A/cm^2 to 0.18 A/cm^2 and 0.09 A/cm^2 to 0.17A/cm^2, respectively. At -0.6V as shown in Figure 2. 22, the fluctuation range dropped even lower to 0.05A/cm^2 to 0.08A/cm^2. Figure 2. 23 and Figure 2. 24 show the current density range in both -0.7V and -0.8V (vs SCE). The current fluctuation range is 0.06 A/cm^2 to 0.02 A/cm^2, and 0.01 A/cm^2 to 0.009 A/cm^2 respectively.

A similar trend was observed for pure Al artificial pit samples as shown in Figure 2. 25 to Figure 2. 29. The current density also fluctuates over the holding time and decreased with the decrease of holding potential. The average current densities at each holding potential for both Pure and

AA7075 were compared in Figure 2. 30. The magnitude of the average current density at each holding potential is lower for pure Al than for AA7075.

2.4.4. i*x calculation for Al and AA7075 and the comparison

Figure 2. 31 to Figure 2. 33 show an example of how the i*x can be calculated from the potentiostatic hold data for both AA7075 and Pure Al artificial pit samples. Figure 2. 31shows the current density over the holding time at a holding potential of -0.3V (vs SCE). Figure 2. 32 shows the accumulated pit depth over the time, calculated by summing the depth generated at elevated potential (1V vs SCE) and the depth generated through holding at -0.3 V (vs SCE). Figure 2. 33 shows the resulting i*x vs time. For AA7075, the range of i*x is from 0.0125^{-3}A/cm to 0.006A/cm with an average value of 0.008A/cm. For pure Al, the range of i*x is from 0.003^{-3}A/cm to 0.0018A/cm with an average value of 0.002A/cm. The similar magnitude of pure Al samples were observed in Lim's testing when a 50 um diameter of Pure Al was held at 1000secs in 0.6M NaCl for i*x calculation.[Mary Lim's PhD project]. However, this value is lower than the reported threshold of i*x that is able to maintain the pit stability (10^{-2} A/cm).

Figure 2.34 and Figure 2.35 show the reciprocal value of depth 1/x vs the current density i for both AA7075 and Pure with a holding potential at -0.3V. The data for the plots were drawn from Figure 2.31 and Figure 2.32. Despite of the fluctuations, the linear relationship between 1/d and i means that i*x is a constant at -0.3V, which indicate a diffusion controlled pit growth.

2.4.5. i*x vs applied potential for both Al and AA7075 and compared with E_{rp}

Using the approach described in section 2.4.4, i*x values of AA7075 and pure Al at the different holding potential were calculated and plotted as a function of applied holding potential as shown in Figure 2. 36 and Figure 2. 37. Cathodic current correction was applied to all the plots in Figure 2. 36 and Figure 2. 37. Figure 2. 36 shows i*x of AA7075 as a function of applied holding potential. From -0.3V to -0.8V, the i*x decreases slowly from 0.009A/cm to $1x10^{-3}$A/cm. Below -0.8V, the current density drops dramatically by two orders of magnitude. The significant decrease of i*x below this transition potential indicates that the pit lost growth stability. This transition potential is consistent with the E_{rp} measured from section 2.3.1 if a 250µA/cm2 criterion is used. A similar transition was observed for pure Al as shown in Figure 2. 37.

The temperature dependence of i*x over the range of possible room temperatures was investigated for pure Al in Figure 2. 37. Two temperatures, 20^oC and 25^oC were selected. The temperature was controlled through the water bath. At 20^oC, from -0.3V to -0.7V, i*x stabilized at a range between $4x10^{-3}$ A/cm to $1x10^{-3}$A/cm. After -0.7V vs SCE, i*x drops by two orders of magnitude. At -0.8V, i*x value decreases to 10^{-5} A/cm. At 25^oC, from -0.3V to -0.7V, i*x is slightly higher than the ones at 20 ^oC at a range between $5x10^{-3}$ A/cm to $2x10^{-3}$A/cm. After -0.7V vs SCE, a rapid decrease of i*x with applied potential was also observed. At -0.8V vs SCE, i*x value decreases to $2x10^{-5}$ A/cm. Thus, there is little effect of temperature on i*x over this range.

Current Decay Testing

2.4.6. Current vs Time for artificial pit samples from -0.95V to -0.3V

In order to test the pit stability over the time, the current density over 100,000 secs for artificial pit samples held at -0.3V to -0.95Vwas collected and plotted in Figure 2. 38. Prior to the potentiostatic holding at each potential level, the artificial pit samples were already exposed to the same solution at an elevated potential to generate a deep pit (> 100 microns).

As shown in the Figure 2. 38, at the higher potential range (-0.3V to -0.7V), the current density starts with a smooth plateau. After 5000secs, the current density starts to fluctuate at a range of 10^{-3} A/cm^2 to 10^{-1}A/cm^2. The current density remaines in this range until the end of exposure. At potentials of -0.75V and -0.8V, after 5000secs, the current density drops dramatically to 10^{-6} A/cm^2, which indicates the loss of pit stability under these conditions.

At even lower potentials, -0.82V and -0.84V, the current density became negative after 16741secs and 6838secs respectively before becoming positive again near the end (at194,400 sec) of the exposure. The negative (cathodic) current density indicates the complete termination of pit growth.

The repassivation time vs applied potential was plotted in Figure 2. 39. Repassivation time was defined as the time at which the current density became lower than 10^{-4}A/cm^2 , according to the criteria used in Lucente's work[11] This current density was selected in order to be consistent with the threshold current density used for the E_{rp} measurements presented in section 2.3.1. This parameter was used as another evaluation of the stability of pit growth. Arrows on points in Figure 2. 39 indicate that the pit continues to grow at current densities greater than 10^{-4} A/cm^2 to the end of the exposure time (100,000 sec). The repassivation time decreases significantly when the applied potential was lower than -0.8V indicating that the pit will lose stability in a much shorter time period. This transition potential is consistent with the value discussed in section 2.3 and 2.4.

2.5. Results: Anodic Kinetics in the pit simulants solution

2.5.1. Anodic Polarization of AA7075 in pit solution simulants

The anodic kinetics of the dissolving surface of a pit was also studied by using pit solution simulants. The purpose of this test is to quantify the critical solution that supports the stable pit growth with the given stability criteria. During the tests, the $i_{critical}$, identified as the current density at -0.8V (vs SCE) were compared in the different level of $AlCl_3$ saturation. The current density at -0.8V was selected as a figure of merit because this is the value observed as the transition potential for i*x as well as the measured E_{rp} from potential vs charge density plateau in Figure 2. 10 and Figure 2. 11. The higher $i_{critical}$ indicates a higher growth rate of the pit. The artificial pit samples of AA7075 were held at an elevated potential (1V vs SCE) for 50 secs to initiate a shallow pit and then scanned down to -1 V vs SCE.

Four levels of saturation of $AlCl_3$ were used as the simulant solutions. Solutions with and without stoichiometric amounts of the major alloying elements were used. Figure 2. 40 shows the polarization curve of AA7075 in $AlCl_3$ as a function of saturation with the consideration of alloying elements. Both OCP and the $i_{critical}$ for four saturation levels were extracted from the curves and listed in Table 2.5.A zoom-in figure with a potential range of interest from -1V to -0.7V vs SCE is shown in Figure 2. 42. As shown in the Figure 2. 40 and Table 2. 5, overall, OCP decreases when the level of saturation went down. $i_{critical}$ was 0.015 A/cm^2, 0.014A/cm^2 for 100% and 80% saturation respectively and decreased by one order of magnitude from

0.014A/cm^2 to 0.004 A/cm^2 when the saturation level of $AlCl_3$ is at 60%. This value remains low at 0.004A/cm^2 with 40% saturation level, which indicates that below 80% of saturation, the solution is not as aggressive as of higher saturation to support high dissolution rate inside the pit.

Figure 2. 41 shows the polarization curve of AA7075 in $AlCl_3$ as a function of saturation without the addition of the salts of the major alloying elements. The details for a zoom-in potential range is shown in Figure 2. 43. A similar trend was observed and the data were also extracted and listed in Table 2.5. The $i_{critical}$ was 0.023A/cm^2, 0.018A/cm^2 and 0.017 A/cm^2 at 100%, 80% and 60% saturation respectively and decreased to 0.006 A/cm^2 when the saturation is at 40%. As shown in the figure, the $i_{critical}$ of 60% saturation of $AlCl_3$ solution without alloying elements is still at the same magnitude of the one for 100% saturation, and much higher than the one in the solution with alloying element (0.004A/cm^2).

Figure 2. 44 compares the $i_{critical}$ as a function of $AlCl_3$ saturation with and without the addition of alloying elements. The solution with alloying elements is intended to simulate the pit solution of AA7075, whereas the solution without alloying elements is to distinguish the effect of alloying elements in the pit solution on the kinetics. For both of the solutions, the $i_{critical}$ initially decreases slowly with the decrease of the saturation. When it is below a transition saturation point, it then drops rapidly. For the solution with alloying elements, this transition point is 80% of saturation. For the solution without alloying elements, this transition point is 60% of saturation. This difference of transition point indicates that the saturation required to support the same amount of dissolution rate for AA7075 is affected by the alloying elements, with the

alloying elements leading to increased pit stability (i.e., the ability to maintain rapid dissolution in less saturated solutions).

2.6. Discussion: The correlation between selected stability criteria

2.6.1. The effect of [Cl-] on E_{rp}

The repassivation potential is identified as a potential threshold below which the pit propagation can no longer be sustained. The understanding and quantification of this potential provide a powerful criterion to predict the corrosion stability of alloys in the long term as the measurement of electrochemical is feasible in practice.

In the present study, E_{rp} (around -0.8V vs SCE) measured from the plateau of potential vs accumulated charge density is consistent with previous research [13,16,17]. Figure 2. 10 shows E_{rp} is [Cl^-] dependent and appears lower value with higher [Cl^-].Due to Newman et al, the E_{rp} is described as follows [18]:

$$E_{rp}=E_{corr}+ \Delta E_{act}+\eta_{IR} \qquad \text{Equation 2.3}$$

Where E_{corr} is the corrosion potential with a given solution, ΔE_{ac} is the overpotential, and η_{IR} is the ohmic drop inside the pit. With higher [Cl^-], the E_{corr} at the bottom of pit as well as the ohmic resistance of the pit solution is lower. Consequently, E_{rp} is lower. Knowing this effect of the solution concentration on E_{rp} provides the insights to predict the pit stability in the actual application with knowing environmental parameters.

2.6.2. i*x value of AA7075 and Pure Al

The i*x value for both AA7075 and Pure Al is measured and compared with the previous research. The value for both materials is comparable to the previous research with the consideration of statistic deviation[10][19].

In Figure 2. 36 and Figure 2. 37, the plateau of i*x over the applied potential above E_{rp} indicate the diffusion controlled pit growth. This diffusion control is verified by the linear relationship of 1/x and i for both AA7075 and Pure Al as shown in Figure 2. 34 and Figure 2. 35. The observation of diffusion controlled pit growth is consistent from the previous research[14,15].

During the i*x measurements in 2.4.3, a 25mV/s scanning rate was used for the polarization scanning down after the potentiostatic holding to remain the aggressive chemistry inside the artificial pit. The similar scanning rate was used by Lucente[19] in her test of pure Al.
In order to evaluate the effect of scanning rate, more tests was run by direct stepping down instead of using scanning rate for the same test. All the results were plotted in Figure 2.36. According to the calculated standard deviation, the results did not make big difference with different scanning down method.

2.6.3. E_{rp} value vs i*x of AA775-T6

The effectiveness of E_{rp} is verified by three ways. First, with current decay testd, as shown in Figure 2. 39, the repassiviation time, identified by when the current density is less 10^{-4} A/cm^2 , drops dramatically after the potential is below -0.8V vs SCE. This shortened time duration indicates the long term stability of the pit growth is lost.

Second, with i*x plotted as an applied potential discussed in section 2.4, a remarkable drop of i*x value was observed when the potential is below -0.8V vs SCE as shown in Figure 2. 36. A plateau of i*x at a higher applied potential in Figure 2. 36 indicate a diffusion controlled pit growth, which is verified by the linear relationship of 1/x vs i plots in Figure 2. 34. When i*x decreases with the applied potential below -0.8V vs SCE, the diffusion controlled pit growth is no longer supported. The pit solution is diluted faster than the dissolution rate at the bottom of the pit can replace it. Consequently, the stabilization of pit growth is lost due to the loss of aggressive pit chemistry. This explains the repassivation process as observed above. i*x and E_{rp} is connected with the consideration as the dissolution rate at the bottom of the pit to maintain the critical pit chemistry is potential dependent.

Third, as shown in Figure 2. 40 and Table 2.5, with the given E_{rp} at -0.8V vs SCE, the corresponding current density of AA7075 decrease remarkably when the saturation is less than 80%. This indicates 80% of saturation of $AlCl_3$ is required to support the stability of pit. This value agreed with the finding from Beck [15].

2.6.4. E_{rp} from saturation $AlCl_3$

According to Table 2.5, the OCP of AA7075 in 100% saturated $AlCl_3$ is -0.92V vs SCE when obtained at a high scan rate. This OCP represents the most conservative E_{rp}, which assumes that pit growth stability can only be maintained with a salt film present at the corroding surface at the bottom of the pit. However, as seen in Table 2.5 and Figure 2. **40**, the significant drop of current density occurred when the saturation is below 80%, which indicates the stability of pit can be maintained even without a saturated layer of salt film. At 80% $AlCl_3$, the OCP is -0.87V vs SCE, higher than the -0.92V for the saturated solution.

2.6.5. The oscillation from potentiostatic holding for artificial pit samples.

As shown in Figure 2. 18 to Figure 2. 21, oscillations over time were observed during the potentiostatic holding of artificial pit samples. This oscillation is likely due to the formation of an unstable salt film. During the potentiostatic holds at potentials well above OCP, the dissolution of Al ion may saturate at the corroding surface, and then a salt film forms. That film can cause a potential drop due to its inherent resistivity which lowers the potential at the interface. The decreased potential lowers the dissolution rate, leading to a lowering of the solution concentration below saturation and subsequent dissolution of the salt film. The potential thus goes back to a higher level and the current spikes until the solution is saturated. The repetition of this process causes the current to oscillate at a constant holding potential. It is also possible that the instability of the current could be due to a surface that is only partially activated. A smaller exposed surface may result in a smoother potential curve over time. However, it is very difficult to further reduce the diameter of wire due the availability of facilities from the manufacturer.

Reference

[1] D. S. Dunn, N. Sridhar, G. a. Cragnolino, *Corrosion* 1996, *52*, 115.

[2] D. S. Dunn, G. A. Cragnolino, N. Sridhar, 2000, 90.

[3] A. Anderko, N. Sridhar, D. S. Dunn, *Corros. Sci.* 2004, *46*, 1583.

[4] G. S. Frankel, *J. Electrochem. Soc.* 1996, *143*, 1834.

[5] G. S. Frankel, *J. Electrochem. Soc.* 1998, *145*, 2186.

[6] G. S. Frankel, *Mater. Sci. Forum* 1997, *247*, 1.

[7] G. S. Frankel, *Corros. Sci.* 1990, *30*, 1203.

[8] N. Birbilis, M. K. Cavanaugh, R. G. Buchheit, *Corrosion Sci.* 2006,48,12,4202.

[9] A. M. Lucente, J. R. Scully, *Corros. Sci.* 2007, *49*, 2351.

[10] A. M. Lucente, J. R. Scully, *J. Electrochem. Soc.* 2008, *155*, C234.

[11] J. Galvele, *Corros. Sci.* 1981, *21*, 551.

[12] S. T. Pride, *J. Electrochem. Soc.* 1994, *141*, 3028.

[13] A. B. Cook, D. L. Engelberg, R. C. Newman, *ECS Transctions*, 2012, *41,25, 121.*

[14] K. P. and richard C. A. Wong, *J. Electrochem. Soc.* 1990, *137*, 3010.

[15] T. R. Beck, N. W. Way, *Electrochimica Acta* 1983, *29,4,485.*

[16] T.-S. Huang, G. S. Frankel, *Corrosion* 2007, *63*, 731.

[17] Z. Zhao, G. S. Frankel, *Corros. Sci.* 2007, *49*, 3064.

[18] N. J. Laycock, R. C. Newman, *Corros. Sci.* 1997, *39*, 1771.

[19] A. M. Lucente, PhD. Thesis, University of Virginia, 2008

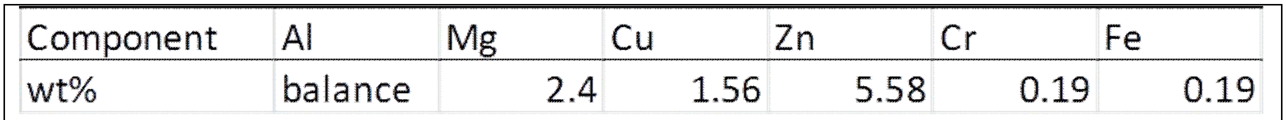

Component	Al	Mg	Cu	Zn	Cr	Fe
wt%	balance	2.4	1.56	5.58	0.19	0.19

Table 2. 1

Alloying composition of AA7075-T6 Rolling Sheet (based on the data from Marta Jakab

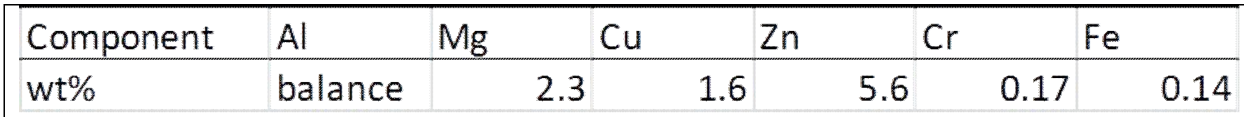

Component	Al	Mg	Cu	Zn	Cr	Fe
wt%	balance	2.3	1.6	5.6	0.17	0.14

Table 2. 2

Alloying composition of AA7075-Hard Temper, fine wire (based on the data from California Wire)

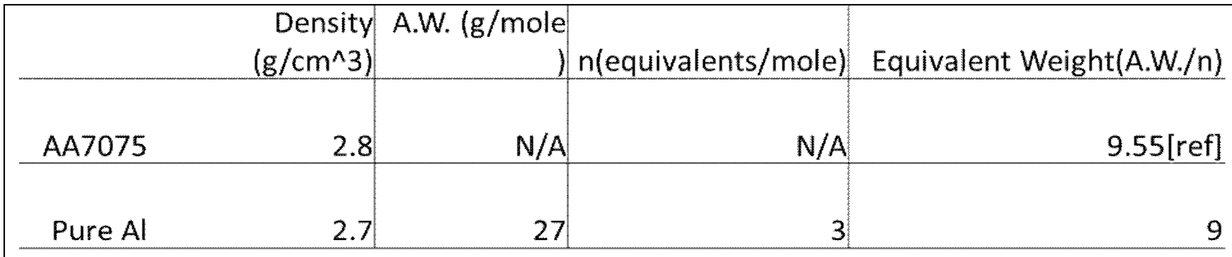

	Density (g/cm^3)	A.W. (g/mole)	n(equivalents/mole)	Equivalent Weight(A.W./n)
AA7075	2.8	N/A	N/A	9.55[ref]
Pure Al	2.7	27	3	9

Table 2. 3

Parameters for current density-pit depth calculation.

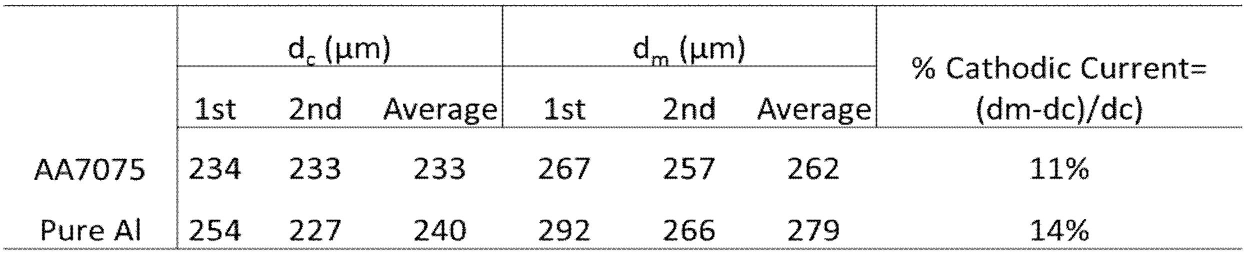

	d_c (µm)			d_m (µm)			% Cathodic Current= (dm-dc)/dc)
	1st	2nd	Average	1st	2nd	Average	
AA7075	234	233	233	267	257	262	11%
Pure Al	254	227	240	292	266	279	14%

Table 2. 4

Parameters for the Calculation of % Cathodic Current

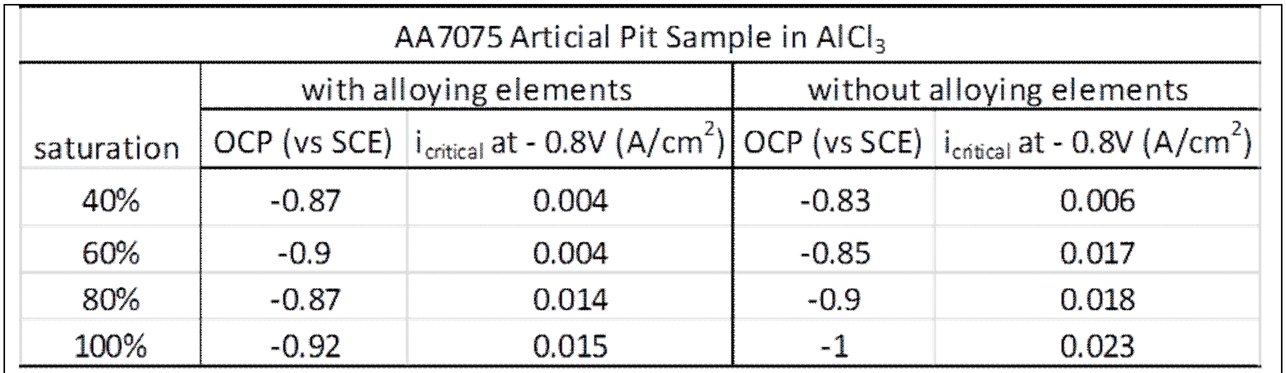

AA7075 Articial Pit Sample in $AlCl_3$				
	with alloying elements		without alloying elements	
saturation	OCP (vs SCE)	$i_{critical}$ at - 0.8V (A/cm^2)	OCP (vs SCE)	$i_{critical}$ at - 0.8V (A/cm^2)
40%	-0.87	0.004	-0.83	0.006
60%	-0.9	0.004	-0.85	0.017
80%	-0.87	0.014	-0.9	0.018
100%	-0.92	0.015	-1	0.023

Table 2. 5

Electrochemical Characteristics of Artificial Pit Samples in Anodic Polarization for AA7075

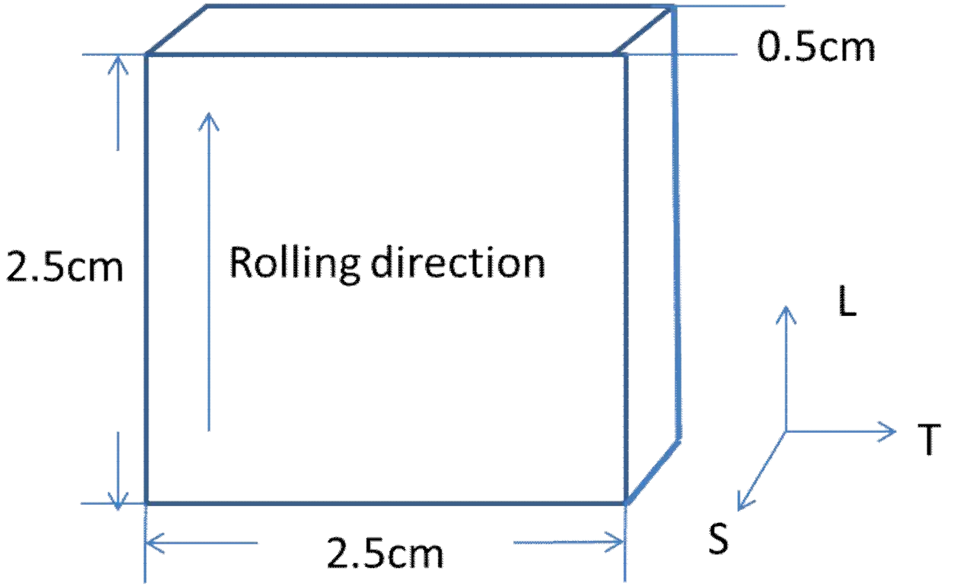

Figure 2. 1

Schematic of the bulk sample of AA7075 (will add a etched microstructure pic)

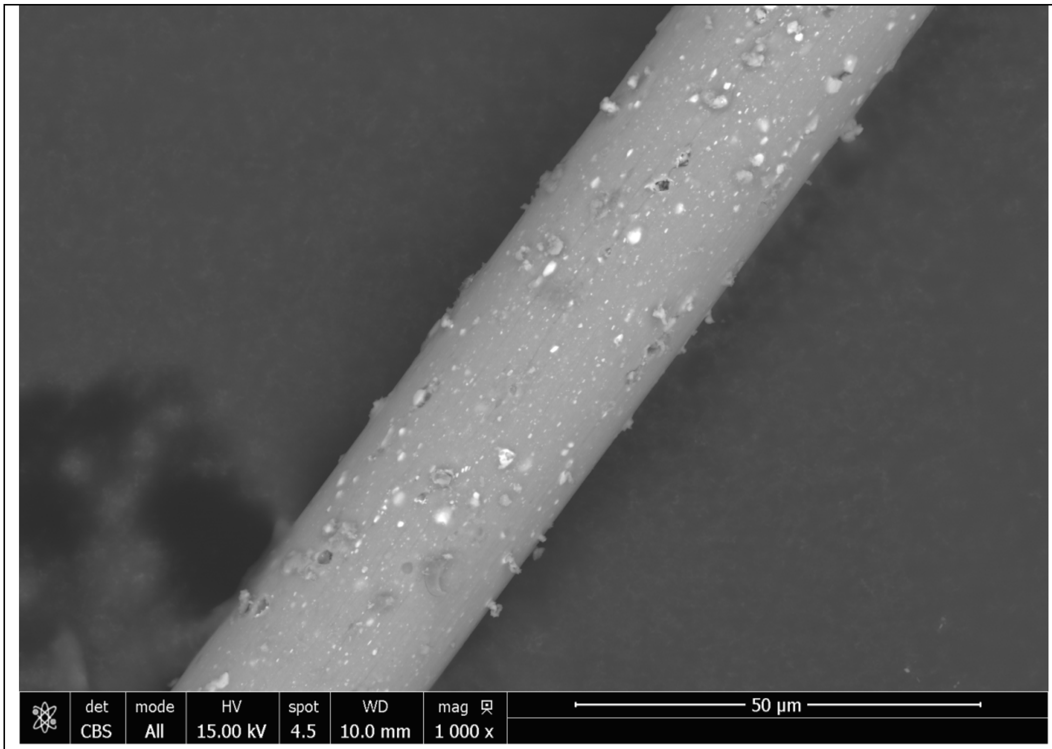

Figure 2. 2

SEM micrograph of AA7075 fine wire with 25 µm diameter

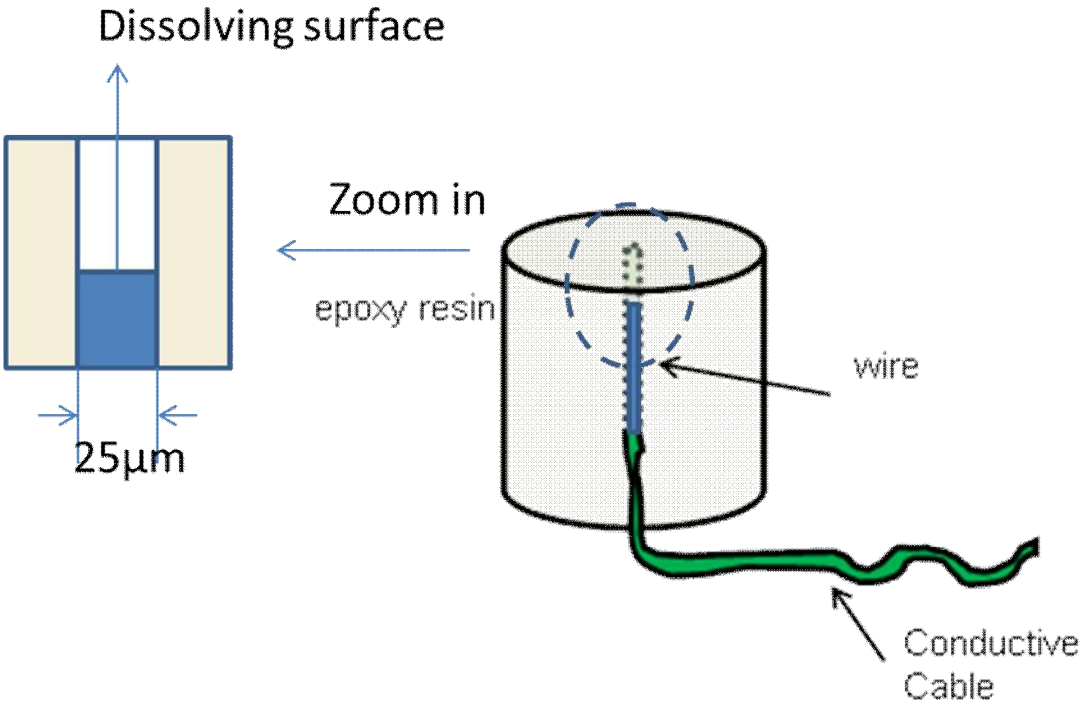

Figure 2. 3

Schematic of the artificial pit sample. Courtesy of Jayendran Srinivasan,

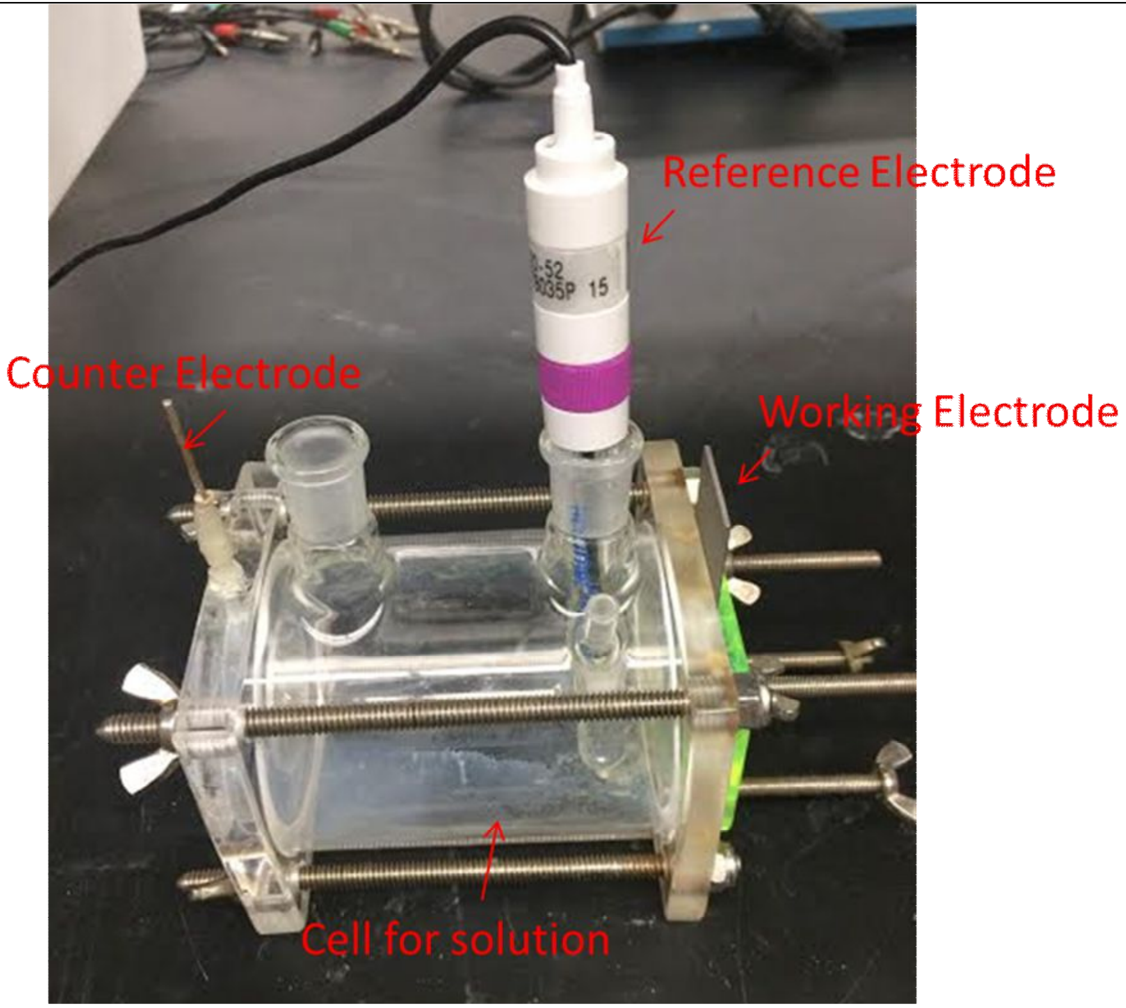

Figure 2. 4

Flat corrosion cell structure with three electrodes

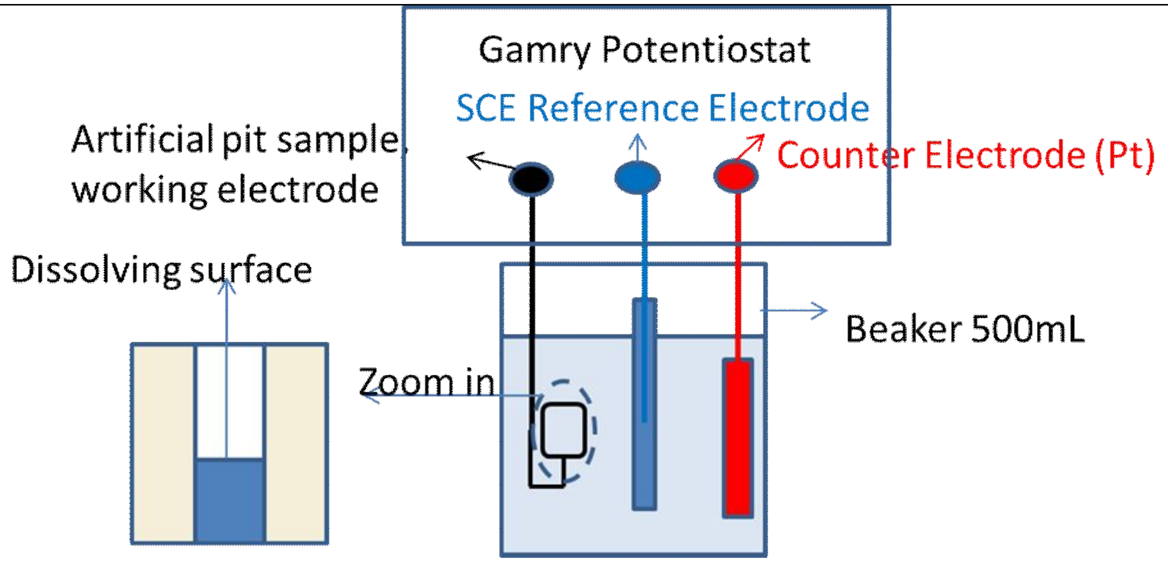

Figure 2. 5

Schematic of the artificial pit sample full immersion test system

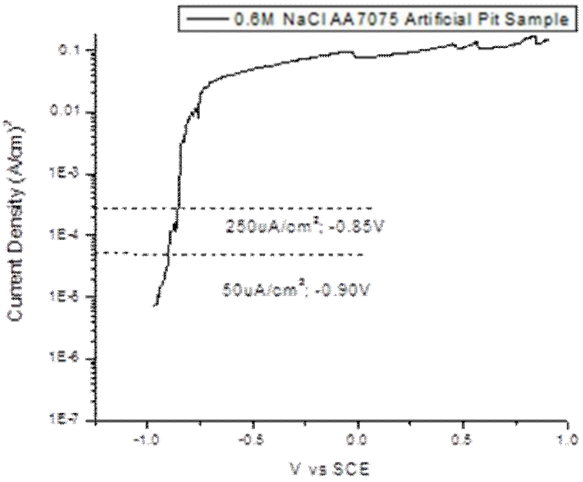

Figure 2. 6

Polarization curve of AA7075 artificial pit in 0.6M NaCl with 275C/cm^2 accumulated charge density from the previous exposure

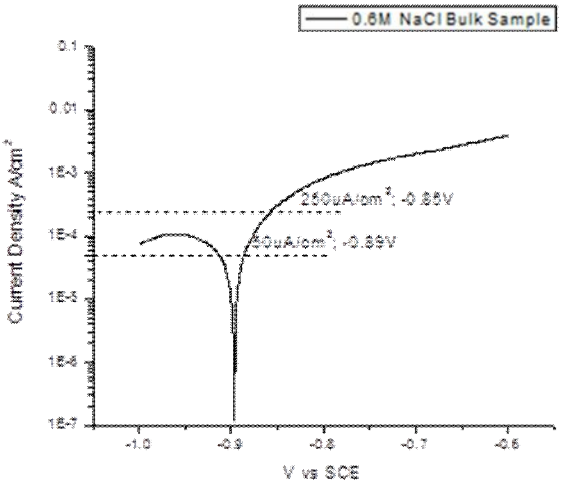

Figure 2. 7

Polarization curve of AA7075 bulk sample in 0.6M NaCl with 103 C/cm^2 accumulated charge density from the previous exposure

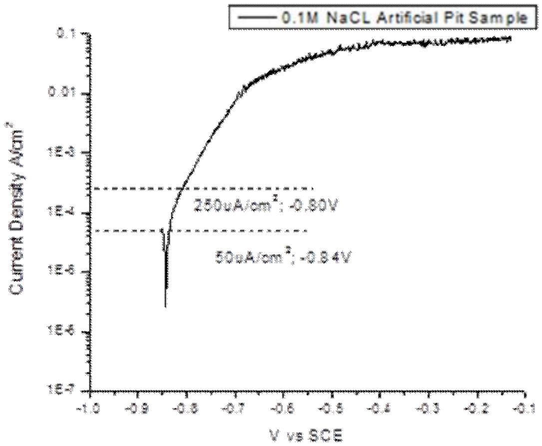

Figure 2. 8

Polarization curve of AA7075 artificial pit in 0.1M NaCl with 213 C/cm^2 accumulated charge density from the previous exposure

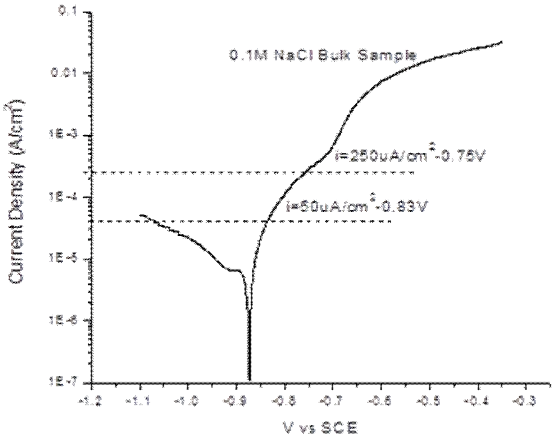

Figure 2. 9

Polarization curve of AA7075 bulk sample in 0.1M NaCl with 52.6 C/cm^2 accumulated charge density from the previous exposure

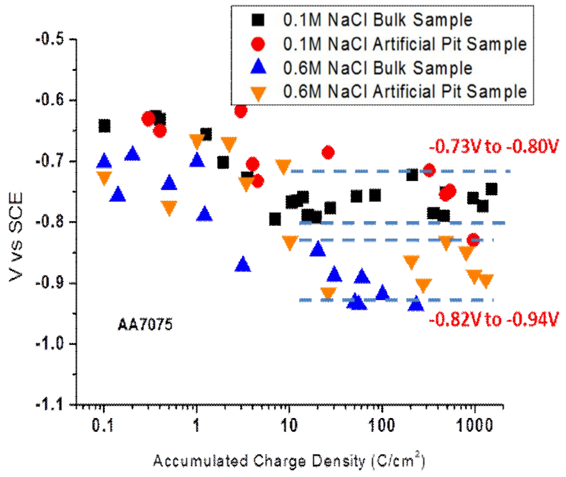 Figure 2. 10	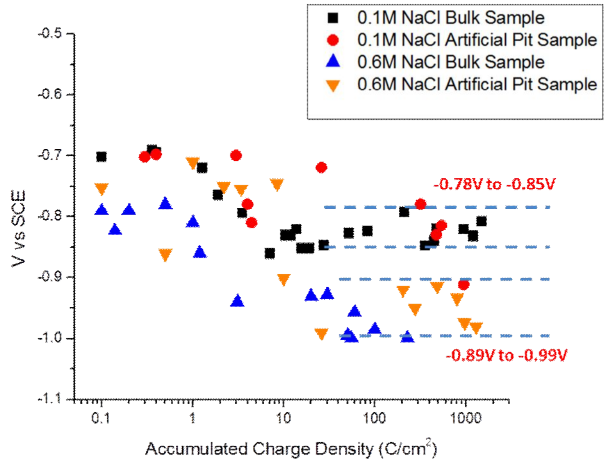 Figure 2. 11
E_{rp} measurement for AA7075 with threshold current density 250 uA/cm^2. Both bulk and artificial sample in 0.1M and 0.6M NaCl are used.	E_{rp} measurement for AA7075 with threshold current density 50 uA/cm^2. Both bulk and artificial sample in 0.1M and 0.6M NaCl are used.

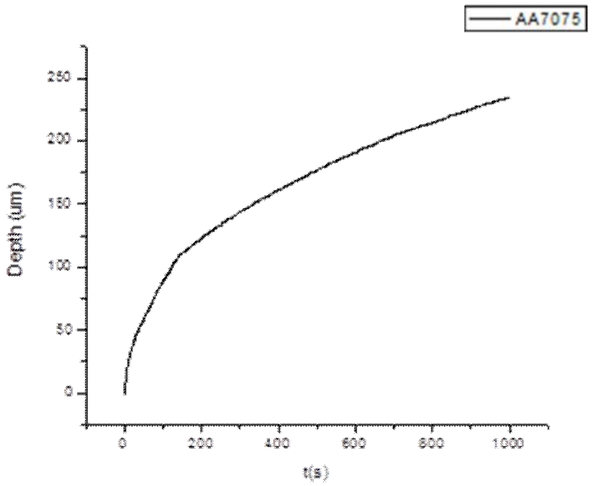 Figure 2. 12	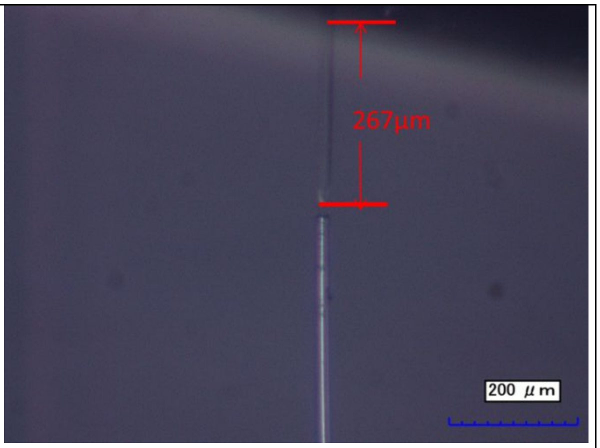 Figure 2. 13
Current density vs time for AA7075 artificial pit sample. The sample is held in 0.6M NaCl at 1V vs SCE for 1000sec.	Depth measure after exposure for AA7075 artificial pit sample. The sample is held in 0.6M NaCl at 1V vs SCE for 1000sec.

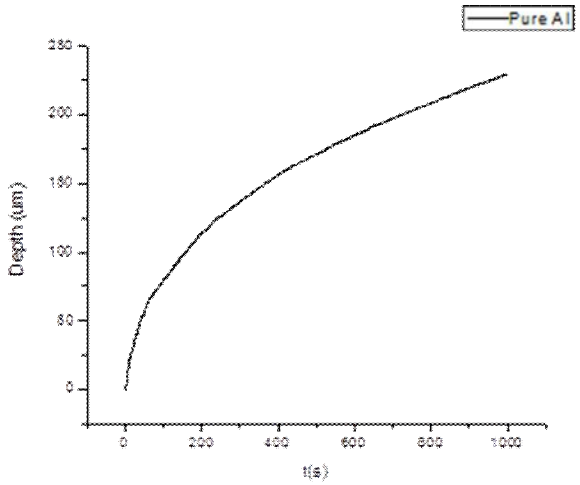 Figure 2. 14	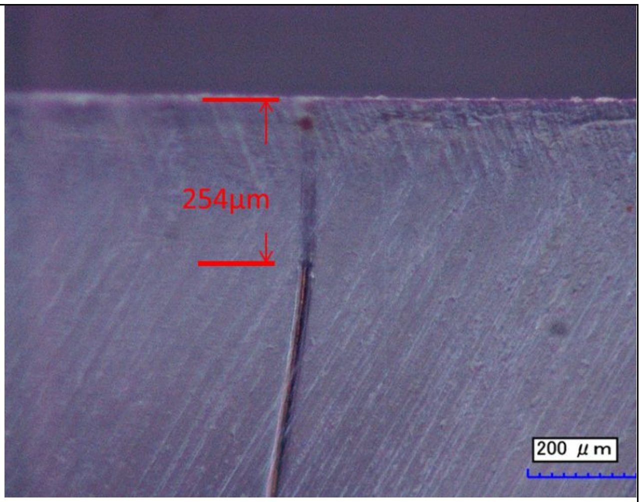 Figure 2. 15
Current density vs time for Pure Al artificial pit sample. The sample is held in 0.6M NaCl at 1V vs SCE for 1000sec.	Depth measure after exposure for Pure Al artificial pit sample. The sample is held in 0.6M NaCl at 1V vs SCE for 1000sec.

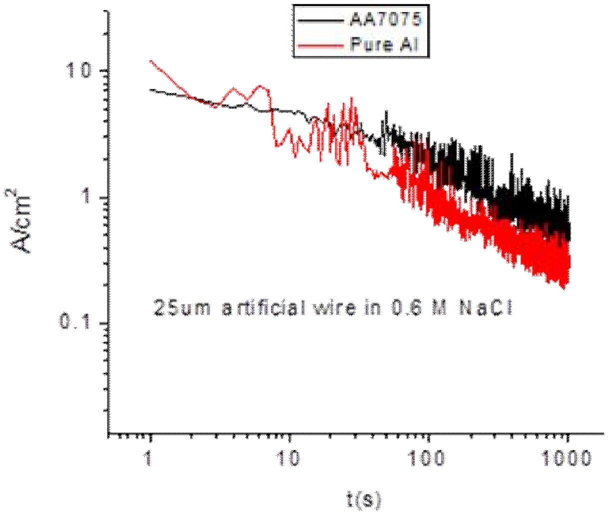

Figure 2. 16

Current Density vs Time at 1V (vs SCE) in 0.6M NaCl for both AA7075 and Pure Al artificial pit samples. The samples were held at 1V vs SCE for 1020 secs.

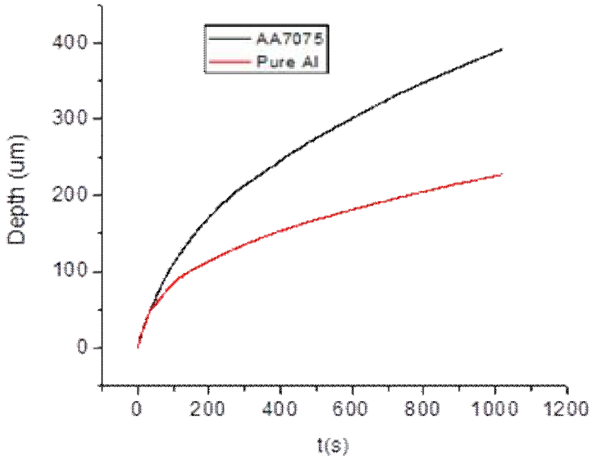

Figure 2. 17

Pit Depth vs Time at 1V (vs SCE) in 0.6M NaCl for both AA7075 and Pure Al artificial pit samples. The samples were held at 1V vs SCE for 1020 secs.

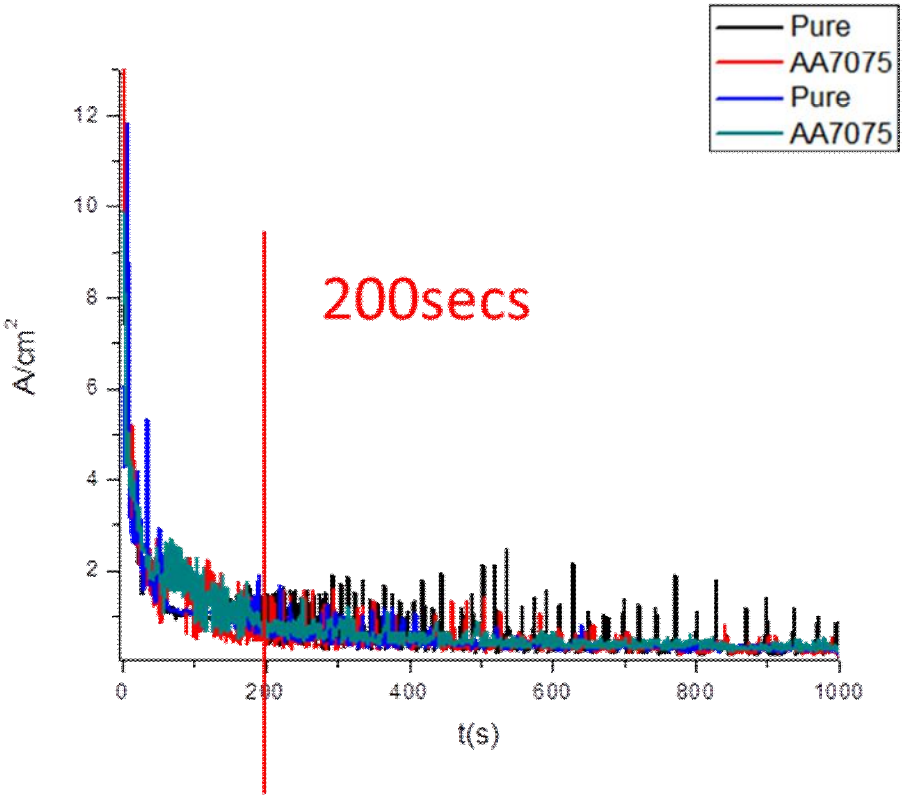

Figure 2. 18

Current Density vs Time for both AA7075 and Pure Al artificial samples in 0.6M NaCl. The samples were held at 1V vs SCE for 1020 secs.

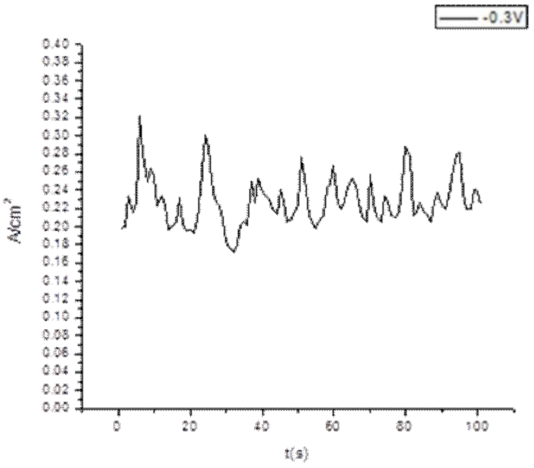 Figure 2. 19	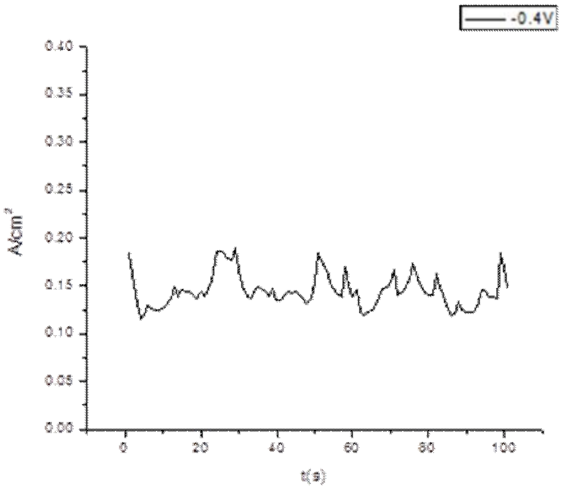 Figure 2. 20
Current Density vs time for AA7075 artificial pit sample with potentiostatic holding at -0.3V in 0.6M NaCl. Sample was previously exposed in the same solution at 1V vs SCE for 1020secs.	Current Density vs time for AA7075 artificial pit sample with potentiostatic holding at -0.4V in 0.6M NaCl. Sample was previously exposed in the same solution at 1V vs SCE for 1020secs.
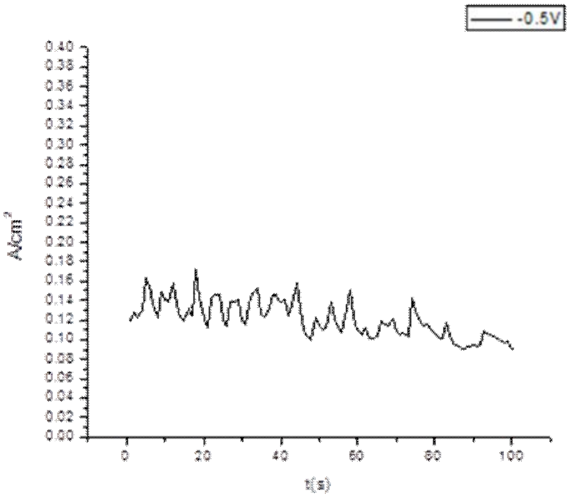 Figure 2. 21	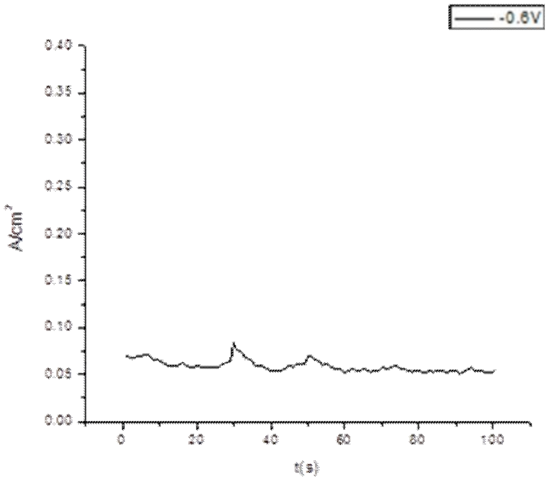 Figure 2. 22
Current Density vs time for AA7075 artificial pit sample with potentiostatic holding at -0.5V in 0.6M NaCl. Sample was previously exposed in the same solution at 1V vs SCE for 1020secs.	Current Density vs time for AA7075 artificial pit sample with potentiostatic holding at -0.6V in 0.6M NaCl. Sample was previously exposed in the same solution at 1V vs SCE for 1020secs.

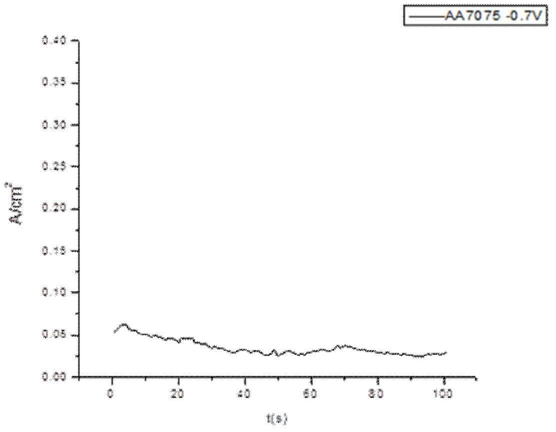 Figure 2. 23	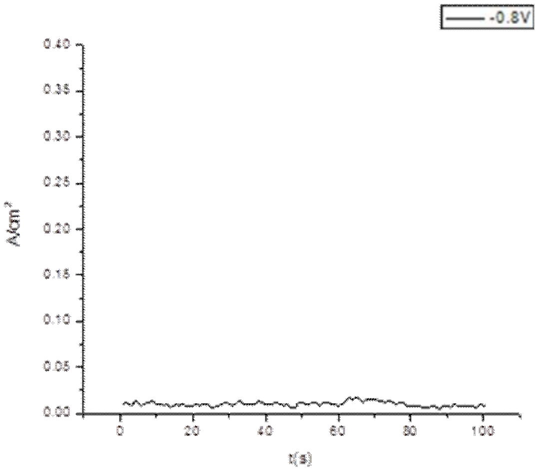 Figure 2. 24
Current Density vs time for AA7075 artificial pit sample with potentiostatic holding at -0.7V in 0.6M NaCl. Sample was previously exposed in the same solution at 1V vs SCE for 1020secs.	Current Density vs time for AA7075 artificial pit sample with potentiostatic holding at -0.8V in 0.6M NaCl. Sample was previously exposed in the same solution at 1V vs SCE for 1020secs.

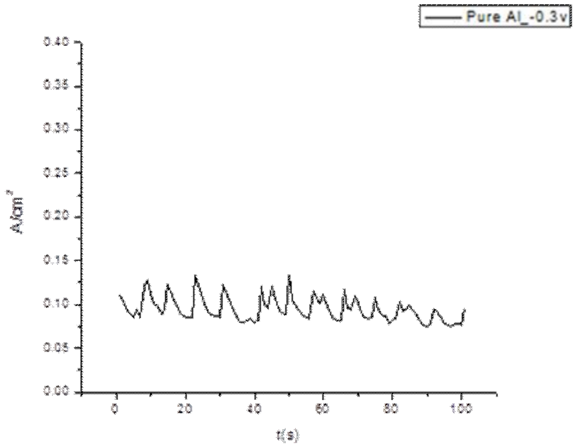 Figure 2. 25	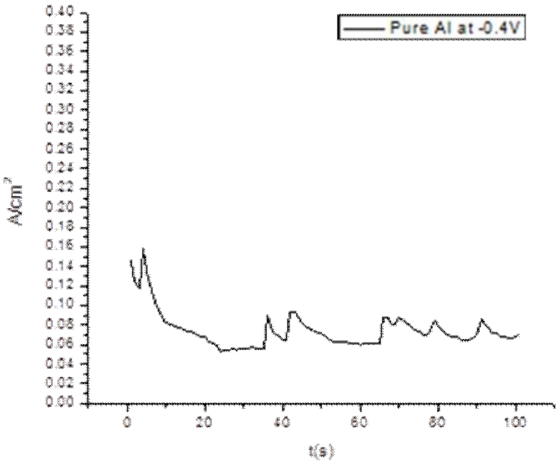 Figure 2. 26
Current Density vs time for Pure Al artificial pit sample with potentiostatic holding at -0.3V in 0.6M NaCl. Sample was previously exposed in the same solution at 1V vs SCE for 1020secs.	Current Density vs time for Pure Al artificial pit sample with potentiostatic holding at -0.4V in 0.6M NaCl. Sample was previously exposed in the same solution at 1V vs SCE for 1020secs.
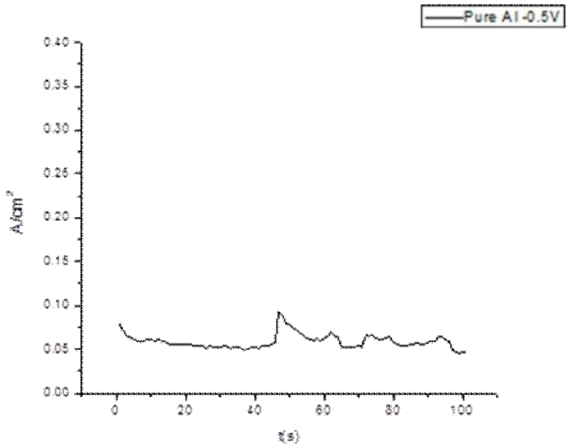 Figure 2. 27	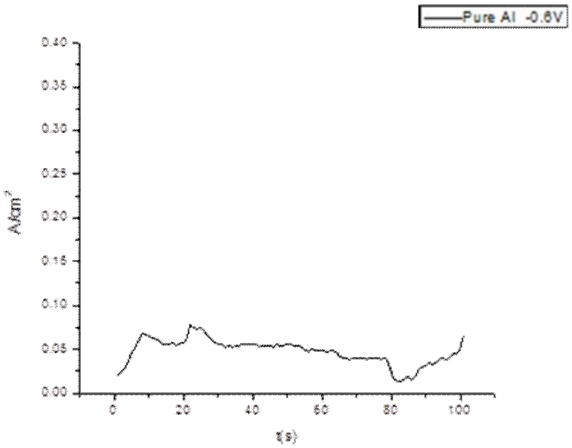 Figure 2. 28
Current Density vs time for Pure Al artificial pit sample with potentiostatic holding at -0.5V in 0.6M NaCl. Sample was previously exposed in the same solution at 1V vs SCE for 1020secs.	Current Density vs time for Pure Al artificial pit sample with potentiostatic holding at -0.6V in 0.6M NaCl. Sample was previously exposed in the same solution at 1V vs SCE for 1020secs.

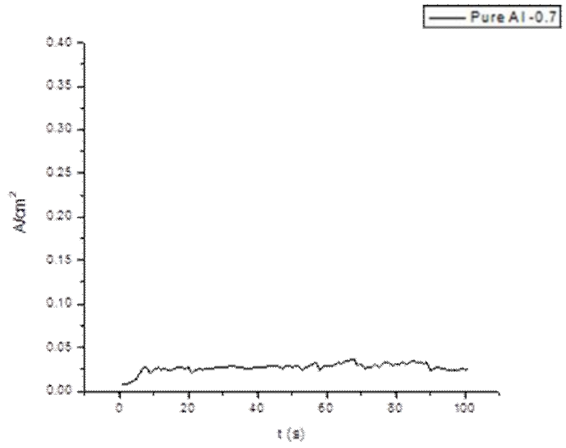

Figure 2. 29

Current Density vs time for Pure Al artificial pit sample with potentiostatic holding at -0.7V in 0.6M NaCl. Sample was previously exposed in the same solution at 1V vs SCE for 1020secs.

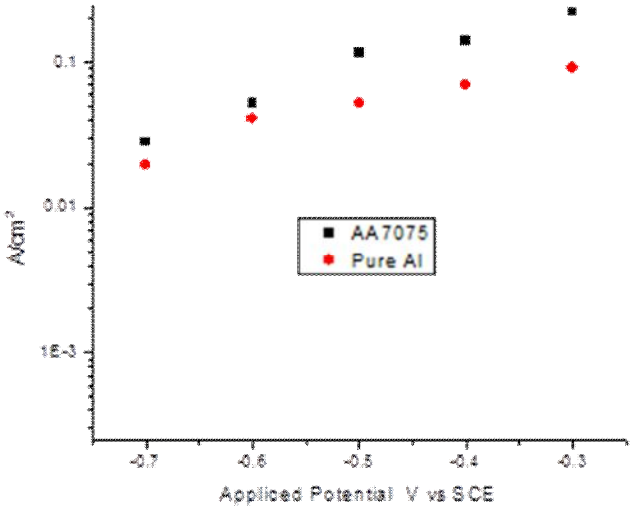

Figure 2. 30

Average current density at each holding potential for both AA7075 and pure Al artificial samples through the potentiostatic holding in 0.6M NaCl. Sample was previously exposed in the same solution at 1V vs SCE for 1020secs.

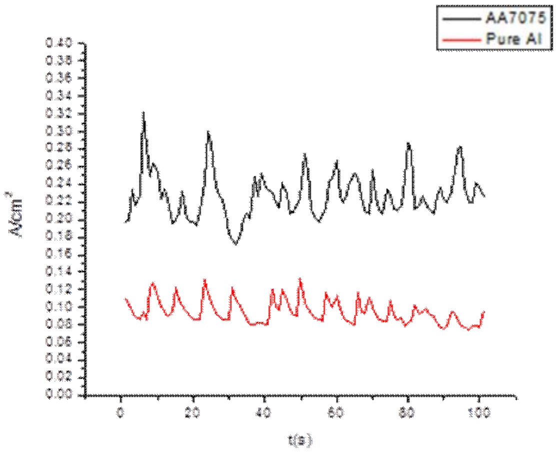 Figure 2. 31	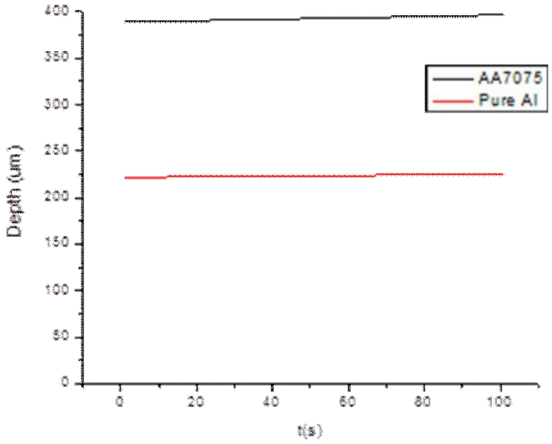 Figure 2. 32
Current density vs time for AA7075 and pure Al artificial pit samples potentiostatic holding at -0.3V vs SCE. Sample was previously exposed in the same solution at 1V vs SCE for 1020secs.	Pit Depth vs time for AA7075 and pure Al artificial pit samples potentiostatic holding at -0.3V vs SCE. Sample was previously exposed in the same solution at 1V vs SCE for 1020secs.
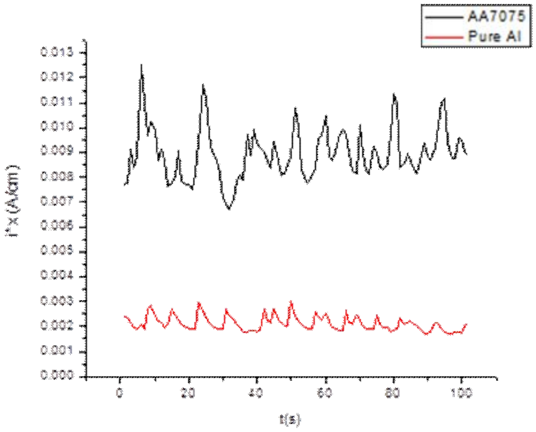 Figure 2. 33	
i*x vs time for for AA7075 and pure Al artificial pit samples potentiostatic holding at -0.3V vs SCE. Sample was previously exposed in the same solution at 1V vs SCE for 1020secs.	

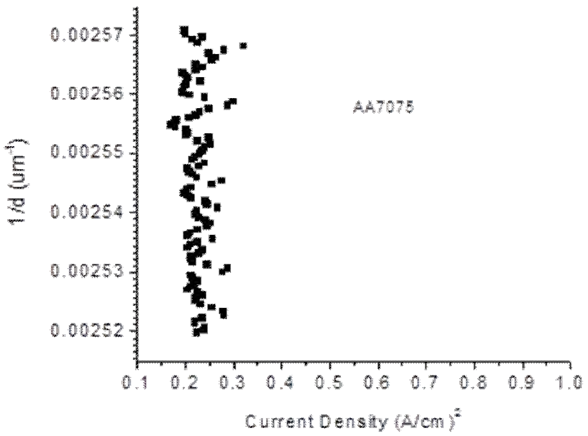 Figure 2. 34	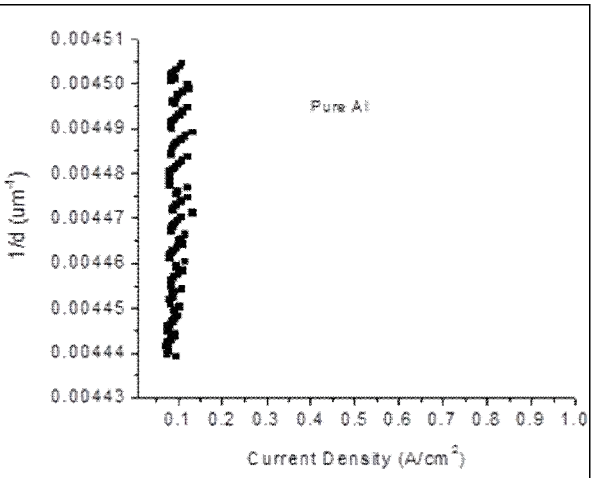 Figure 2. 35
i/d vs current depth for for AA7075 artificial pit samples potentiostatic holding at -0.3V vs SCE. Sample was previously exposed in the same solution at 1V vs SCE for 1020secs.	i/d vs current depth for for pure Al artificial pit samples potentiostatic holding at -0.3V vs SCE. Sample was previously exposed in the same solution at 1V vs SCE for 1020secs.

<table>
<tr>
<td>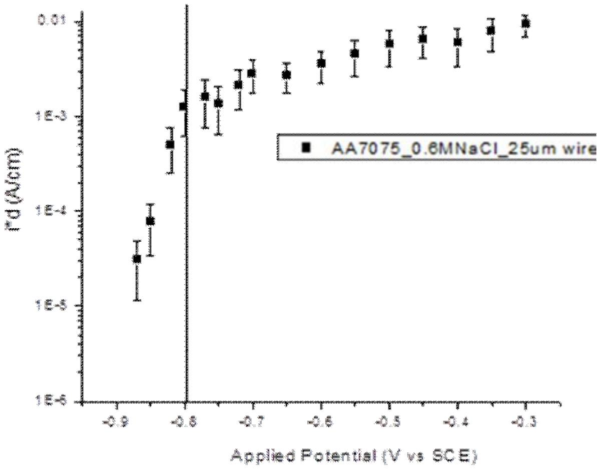

Figure 2. 36</td>
<td>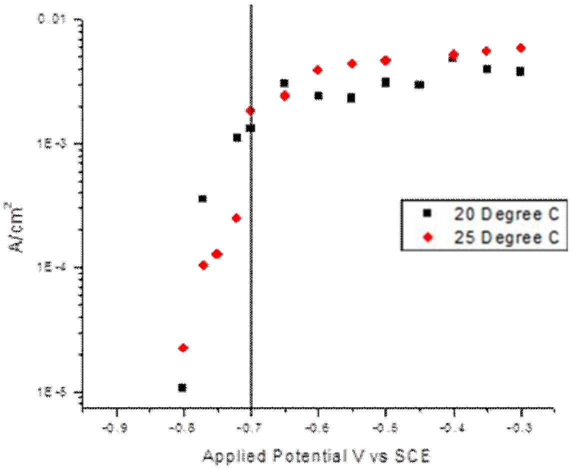

Figure 2. 37</td>
</tr>
<tr>
<td>i*x vs applied potential for AA7075 in 0.6M NaCl</td>
<td>i*x vs applied potential for Pure Al in 0.6M NaCl</td>
</tr>
</table>

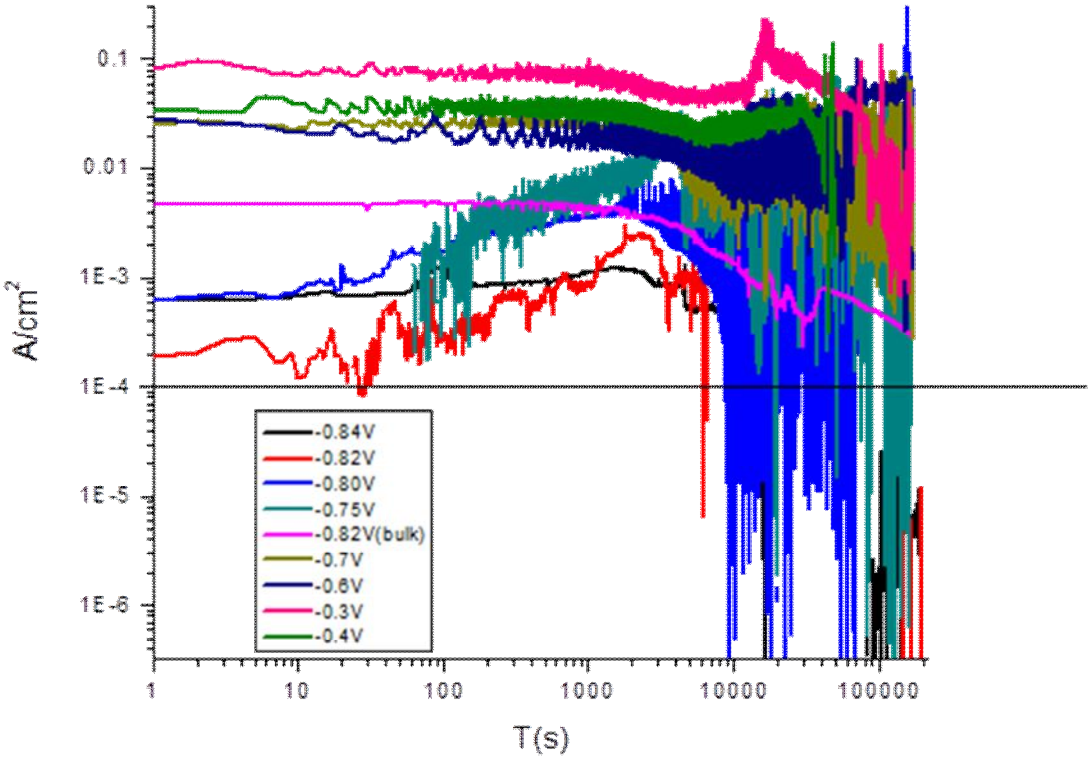

Figure 2. 38

Current vs Time for AA7075 artificial pit samples from -0.95V to -0.3V in 0.6M NaCl

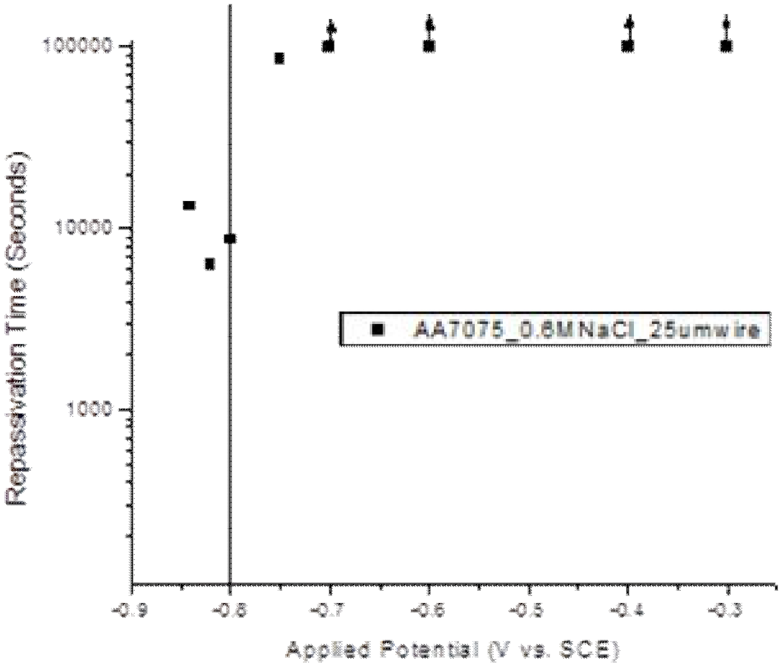

Figure 2. 39

Repassivation Time as a function of applied potential for AA7075 in 0.6M NaCl

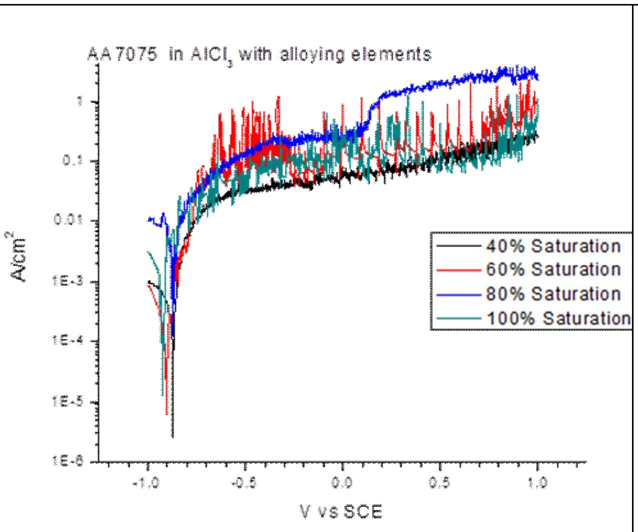

Figure 2. 40

Anodic polarization of AA7075 with alloying elements in $AlCl_3$

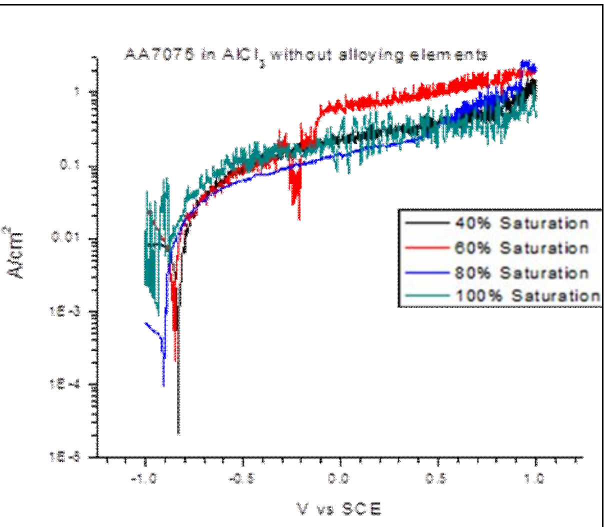

Figure 2. 41

Anodic polarization of AA7075 without alloying elements in $AlCl_3$

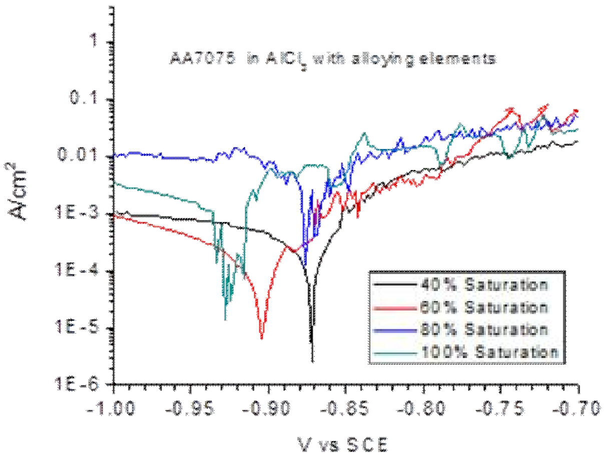

Figure 2. 42

Anodic polarization of AA7075 with alloying elements in $AlCl_3$, zoom-in

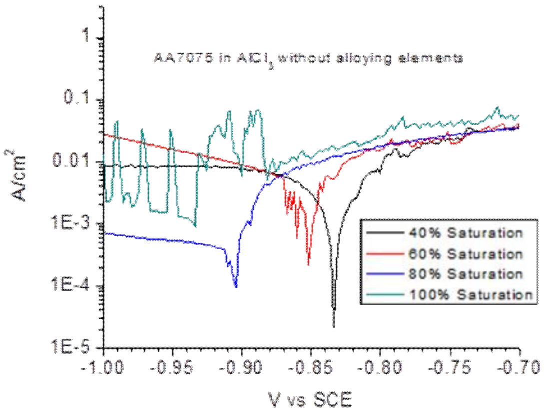

Figure 2. 43

Anodic polarization of AA7075 without alloying elements in $AlCl_3$,zoom-in

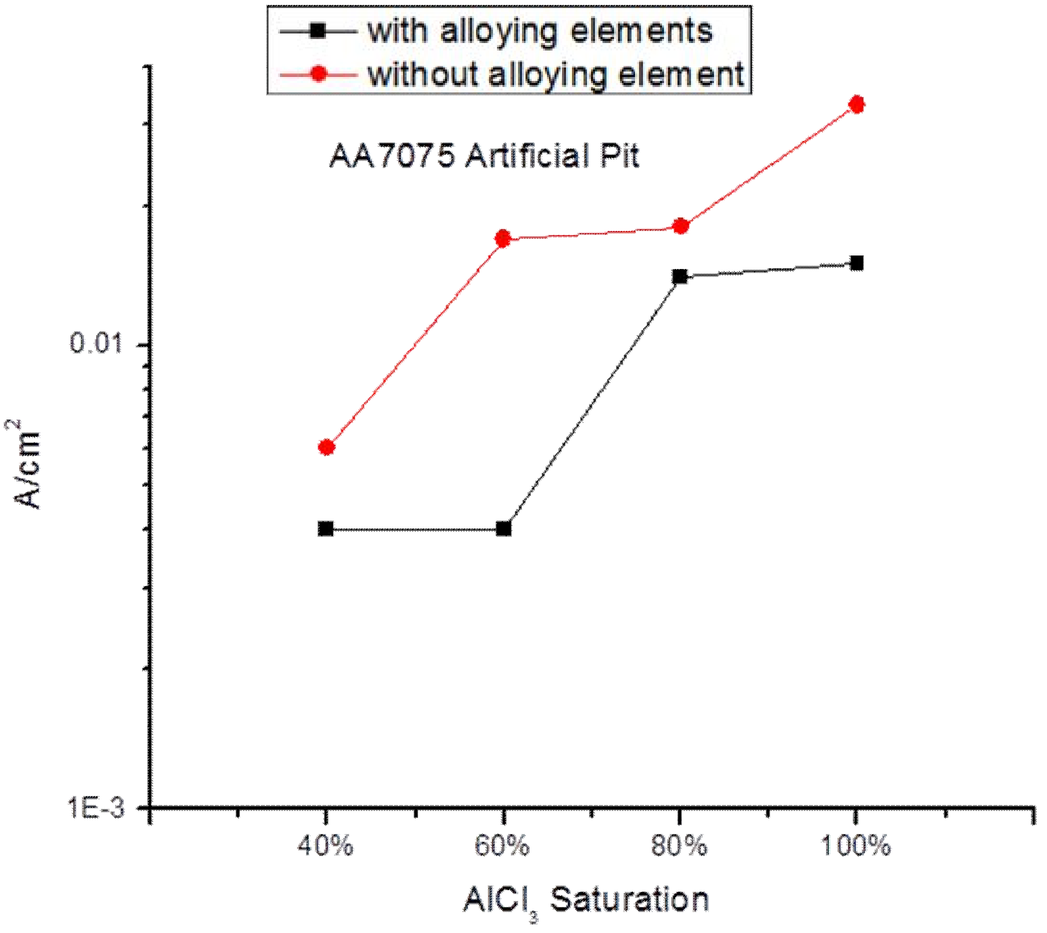

Figure 2. 44

$i_{critical}$ vs $AlCl_3$ concentration of AA7075 artificial pit samples

Chapter 3 Galvanic Coupling under Difference Exposure Conditions

In this section, the galvanic corrosion of AA7075-T6 coupled with noble materials in both full immersion and under atmospheric condition was investigated. The results from full immersion tests with and without an external cathode were also conducted on AA7075-T6. In the tests without external cathode, the damage morphology as a function of holding potential was studied. In the galvanic coupling test, the corrosion damage responses to the change of coupling condition such as the [Cl^-], the cathode-to-anode area ratios as well as the selection of external cathode were studied.

The noble material-AA7075-T6 galvanic system was also exposed under the atmospheric conditions as a function of the choice of noble material, relative humidity (RH), cathode-to-anode area ratio, and the exposure time duration. The interfacial potential along the coupling surface was measured by the Scanning Kelvin Probe (SKP) technique. The damage along the coupling surface was also examined by optical microscopy after cross-sectioning. The resulting potential dependent damage evolution was used to validate the effectiveness of E_{rp} measured from Chapter 2 on the atmospheric condition.

3.1. General Introduction

3.1.1. Background:

A great deal of literature [1–5] has shown that the effect of a galvanic cell can be strongly influenced by both the environmental parameters (*i.e.*, pH, species concentration, etc.) and geometry parameters (*i.e.*, cathode-to-anode area ratio, distance between the anode/cathode area, and shapes of the anode and cathode).

In the present study, a simulated fastener geometry of AA7075-T6 with a noble material coating is of importance due to its use in aerospace and applications as well as the additional complexity of the galvanic interaction between the noble material coating layer and the Al alloy substrate. Mizuno [6] has studied the galvanic corrosion of Steel-AA5083 under atmospheric conditions both experimentally and computationally. His study was focused on a simple planar configuration of the coupling system. Feng and Frankel[7] studied a similar fastener geometry for an Al alloy coating panel with noble material fasteners and determined the number and location of noble fastener material on the galvanic interaction under atmospheric exposure. However, the study for a galvanic corrosion of predicting of its stability under both full immersion and atmospheric condition using stability criteria is still very limited. Chen and Kelly [8] also establish an analytical model that linked localized corrosion to environment condition, including RH, electrolyte thickness, which can be used to predict the stability of localized corrosion under simple geometry. However, a stability prediction for a complex galvanic interaction still needs some improvement.

3.1.2. The scientific problems to be addressed in this chapter

In this study, questions of interest focus on two conditions, full immersion and atmospheric exposure. The problems to be addressed in the present study include:

1) To determine how the environmental factors such as the species concentration of electrolyte, cathode-to-anode area ratio, the nature of materials affect the galvanic coupling system of noble materials-AA7075-T6 for a full immersion condition.

2) To determine the effect of exposure condition, such as the Relative Humidity (RH), the water layer thickness, as well as the exposure time on the galvanic coupling interactions for an atmospheric condition.
3) To validate the effectiveness of E_{rp} for the galvanic coupling condition.

3.1.3. General approach used to solve the problem

For the full immersion galvanic tests, the samples were immersed in a beaker cell system as described in section 3.2.3. The potential during the galvanic coupling was recorded in order to characterize the electrochemical kinetics. The corrosion damage along the cathode-to-anode interface was examined with optical microscopy after cross-sectioning in order to distinguish the effect of environmental factors.

For the atmospheric exposure, the samples were mounted in a planar epoxy configuration and exposed in a desiccator containing different saturated salt solution at the bottom of the container in order to control the RH to the desired level. The corrosion damage was examined under optical microscopy after cross-sectioning. The interfacial eletrochemical potential was measured through SKP, converting the surface work function into the eletrochemical potential via a calibration curve.

3.1.4. Brief summary of the results

For the full immersion condition, the corrosion damage as a function of holding potential (-0.67V to -0.55V vs SCE) for the AA7075-T6 without external cathode was plotted to illustrate the effect of holding potential on the corrosion damages. Corrosion damage does not develop until -0.64V and higher holding potentials. IGC damages presents at higher holding potential.

Also, the damages from galvanic coupling under full immersion conditions were plotted as a function of cathode-to-anode arear ratio (1:1, 30:1, 60:1, 100:1) and the nature of cathode (Ni and BMI) in both 0.6M NaCl and 2.8M NaCl. The coupling potential and the electrochemical kinetics after the exposure were characterized to rationalize the effects of different environmental conditions. The damages from different cathode materials do not change a lot. The damages increase with the increase of cathode-to-anode area ratio, and then reached a plateau at higher cathode-to-anode area ratio. The average depth of damage for exposure solution with higher [Cl^-] is deeper if the rest of conditions remain the same.

Similarly, the damages from galvanic coupling under atmospheric exposure were compared under two different RH (98% and 90%) with different cathode-to-anode area ratio (1:1, 30:1, 60:1, 100:1) for 33hrs, 66hrs and 100hrs exposure, respectively.. The damage is most severe at the sites where anode is connected with the cathode. Less corrosion attacks are found in the anode sites where is distant from cathode.

In addition, interfacial electrochemical potential were measured during the above exposures via SKP. The potential at the damage free region along the coupling interface were compared with E_{rp} from chapter 2 to validate the effectiveness of this stability criterion.

3.2. Experimental Methods

. Two cathode materials, pure Ni and BMI were used for the tests. The electrochemical characteristics and corrosion morphology of AA7075 were investigated under both full immersion and atmospheric exposures with the change of solution concentration and relative humidity.

3.2.1. Materials and Specimen Preparation

Rolled sheet of AA7075-T6 was used as the anode material in this chapter. The composition and dimension was the same as in section 2. 2.1.

Pure Ni (99.9%) and BMI materials were used as cathode materials. BMI is a composite consisting of carbon fiber reinforcements in a bismaleimide resin. A microstructure of BMI was shown in Figure 3. 1

.

For full immersion tests, bulk samples for both anode (AA7075) and cathode (Ni and BMI) were polished with 800 grit and cleaned with methanol before any exposure. For atmospheric tests, AA7075-T6 and cathode materials were mounted in epoxy with a copper tape set at the back of the sample to ensure the conductivity between the two pieces. The schematic configuration is shown in Figure 3. 2. The cleaning and polishing process was the same as for the cathode materials. In both test conditions, the cathode's area was changed accordingly to create the desired cathode-to-anode area ratio condition.

The post-exposure samples were cross sectioned, mounted in the epoxy and polished until a mirror finish. Optical microscopy was used to examine the corrosion damage from the different experimental conditions.

3.2.2 Solutions and Environments

Sodium Chloride (NaCl) solutions with various concentrations were prepared for full immersion tests. 0.6M and 2.8M NaCl were used for the full immersion galvanic tests in test 3.2.4.2 to 3.2.4.3.

Two relative humidities (RH), 90% and 98%, were selected for the atmospheric exposure. RH 98% and 90% were selected to be equivalent to 0.6M and 2.8M NaCl from the full immersion condition. A glass desiccator and saturated K_2SO_4 solution (for RH98%) and saturated $BaCl_2$ solution (RH90%) were used to maintain the target RH. Three deposition densities, 3.5g/m^2 , 5.25g/m^2 and 7g/m^2, were selected to control the water layer thickness with the given solution concentration. Given the deposition density and the exposure area, the amount of NaCl solution and its thickness for the exposure surface can be calculated. The solution was then measured and transferred to the exposure surface by micro pipette. In order to maintain a constant water layer thickness, the same amount of NaCl solution was added upon the surface every 12 hours to prevent the drying out of the exposure surface. Corrosion products were accumulated along the cathode-to-anode interface. The surface was not rinsed when adding new NaCl solution in order to avoid the removal of the corrosion products layer.

De-ionized water was used for solution preparation. All the solutions were prepared and used at room temperature with aerated condition.

3.2.3 Apparatus

3.2.3.1 Beaker Cell for Galvanic Full Immersion

A three-electrode system was set up with a 500mL beaker for full immersion galvanic tests. Bulk samples of AA7075 (anode) and Ni and BMI (cathode) were immersed in a beaker and connected via Gamry Potentiostat and the galvanic corrosion module of the software was used. An SCE reference electrode was used in this test. The schematic illustration of the experiment set up is shown in Figure 3. 3.

3.2.3.2 Scanning Kelvin Probe Measurement Set Up

A Model SKP5050 Corrosion Package (RHC020, KP Technologies) with a 0.5-mm diameter gold-coated probe was used to measure the work function of the metal under the thin electrolyte layer. 50 gradients was used. SKP measures the work function on a conductive surface and then convert it into the surface potential. Prior to each test, reference metal samples (Pt, Zn and Iron) were used for calibration to establish a converting linear function between the measured work function and the electrochemical potential.

A humidity chamber attached to SKP (RHC020, KP Technologies) with atmospheric condition controlling system was used in the experiment to achieve the RH during the SKP scanning. The RH was the same as the ones used in the atmospheric exposure in the desiccator.

3.2.4 Procedures

3.2.4.1 Potentiostatic Full Immersion Test

AA7075 bulk samples were immersed in a flat cell in 0.6M NaCl solution and potentiostatically held at a potential ranging from -0.55 V to -0.67V (vs SCE) for up to 3hours. The post-exposure samples were prepared and polished based on procedures listed in session 3.2.1. The optical microscopy was used to examine the corrosion damage. The cross-section aims to inspect the most severely corroded area. The deepest corrosion depth was measured to quantify the damage. This method is consistent for all the corrosion damage measurements in this chapter.

3.2.4.2 Galvanic Full Immersion Test

Bulk samples of AA7075 were used as the anode for the galvanic system. The cathode materials selected here is Ni and BMI. The anode to cathode nominal area ratio selected for the tests are 1:0; 1:1; 1:30; 1:60; 1:100. The solution for the full immersion test was either 0.6M NaCl and 2.8M NaCl. The anode and cathode was immersed in a beaker cell stated in session 3.2.3.1.

During the test, a Gamry potentiostat PCI-4 was used to monitor the galvanic current and potential. The duration of all the tests was 100 hours. After 100 hours, the samples were cross-sectioned in preparation for optical microscopy analysis. The corrosion damage was examined under optical microscopy and the deepest corrosion damage was measured and plotted as a function of experiment condition.

3.2.4.3 Polarization Test after Full Immersion Exposure

Anodic polarization tests on AA7075 were also conducted at the end of some full immersion tests. The test set up from session 3.2.3.1 was used for the full galvanic immersion. The anode to cathode area ratio was 1:1. The polarization scanning was taken after a full immersion exposure period of 33hrs, 66hrs and 100hrs respectively. The scanning started from from 1V to -1V (vs SCE) with a scanning rate of 0.5mV/s.

3.2.4.4 Galvanic Coupling Test in Atmospheric Condition

Bulk samples of AA7075 as the anode and Ni or BMI as the cathode were used for atmospheric testing. To be consistent to the full immersion test, the cathode –to-anode area ratios were chosen as 1:1, 30:1, 60:1, 100:1. The samples were prepared in epoxy according to the procedure in session 3.2.1.

The samples were removed from the desiccator after 33hours, 66hours, or 100 hours of atmospheric exposure to prepare for the damage morphology measurement. The distributions of corrosion damage along the anode surface were captured by optical microscopy. The deepest damage was measured and plotted as a function of experimental conditions.

3.2.4.5 SKP Measurement for the Potential Distribution on the Coupling Interface

The coupling samples, under RH98% exposure, were scanned under the SKP after 33hrs, 66hrs, and 100hrs exposure. The scanning was started at the interface of cathode/anode and completed at the end of anode exposure surface as shown in Figure 3. 4. A constant gradient of 50, which represents the distance between the SKP tip and the measured surface, was applied for all the potential measurements. The surface potential converted from work function was plotted as a function of the distance from anode/cathode interface. A example of work function calibration is shown in Figure 3. 5. This measurement aimed to characterize the potential changes along the anode surface when it is distant from the cathode.

3.3. Galvanic Coupling Test in full immersion condition

3.3.1. Damage morphology in potentiostatic full immersion test without external cathode

Full immersion potentiostatic tests of AA7075-T6 were conducted over a range of potential (from -0.55V (vs SCE) to -0.67V (vs SCE)) in 0.6M NaCl. The goal of the experiments was to investigate the damage evolution for the alloy of interest in the absence of an external cathode. Figure 3. 6 to Figure 3. 18 show the optical images of the exposed surface of AA7075-T6 after 3 hours of immersion at a variety of potential levels. The areas with most severe damage were selected and recorded. Figure 3. 6 to Figure 3. 8 show the exposed surface of samples under relatively low holding potentials (-0.67 to -0.65V vs SCE). No remarkable damage was observed under these conditions. As shown in Figure 3. 9 to Figure 3. 12, more aggressive corrosion damage was developed with the increase of potential from -0.64V to -0.61V vs SCE. For Figure 3. 9, under a holding potential -0.64V vs SCE, the deepest damage was measured as 87μm. With the higher potential -0.63V to -0.61V vs SCE, according to Figure 3. 10 to Figure 3. 12, the deepest damage was measured as 105 μm, 150 μm, and 156 μm respectively. Figure 3. 13 to Figure 3. 18 show the corrosion damage under the potential -0.61V and higher. The damage continued to deepen from 140 μm to 200 μm. Intergranular Corrosion (IGC) was also present in Figure 3. 13, Figure 3. 14 and Figure 3. 15.

The corrosion damage evolution as a function of holding potential is summarized in Figure 3. 19. The damage increased rapidly (0 µm to 156 µm) from -0.67V to -0.61V. From -0.60 V to -0.55V (vs SCE), the depth of damage reached a relatively stable regime. The highest depth was 200 µm. According to the images, IGC only occurs at the higher holding potential.

3.3.2. The damage morphology as a function of cathode-to-anode area and the selection of Noble Materials in 0.6 M NaCl

The damage morphology from the galvanic coupling between AA7075-T6 and noble materials was also studied as a function of cathode-to-anode area ratio in the selected solution (0.6M NaCl). The bulk samples of AA7075-T6 were coupled with noble materials (Ni and BMI) and immersed in the 0.6M NaCl for 100hours. Both the coupling potential and coupling current were monitored during the exposure. After the exposure, the cross sections of the exposed samples (AA7075-T6) were examined under optical microscopy to study the effect of different experimental conditions on the corrosion damage morphology and depth. For the given solution (0.6M NaCl) and exposure time (100hrs), the corrosion damage varied with the selection of external cathode (BMI and Ni) and cathode-to-anode area ratio.

Figure 3. 20 to Figure 3. 27 show the damage morphology under optical microscopy as a function of cathode-to-anode area ratio and the selection of cathode materials. Figure 3. 20 is the corrosion damage morphology of AA7075-T6 after 100hrs exposure when it was coupled with BMI at 1:1 cathode-to-anode ratio. Localized corrosion propagated across the exposed surface although the distribution was not uniform. The deepest corrosion pit measured was 114µm. Figure 3. 21 shows the exposed surface of an AA7075-T6 sample without coupling with any

external cathode. In this case, very few corrosion damage sites were observed. Figure 3. 22 to Figure 3. 25 show the corrosion damage of AA7075-T6 coupled to different areas of Ni. The distribution and severity of the localized corrosion changed as the cathode-to-anode ratio increased from 1:1to 100:1. According to Figure 3. 22 and Figure 3. 23, when the cathode-to-anode ratio is below 30:1, the localized corrosion primarily developed in the middle of the exposed sample. The deepest pit as measured was 103µm and 134µm for cathode to anode 1:1 and 30:1, respectively. When the cathode: anode area ratio increased to 60:1 and 100:1, as shown in Figure 3. 24 and Figure 3. 25, more severe corrosion damage developed at both the center and the edge of the sample. The deepest damage from the measurement was 459µm (edge), 156 µm (center) for 60:1, and 564µm (edge) and 169 µm (center) for 100:1, respectively. The aggressive acidic chemistry developed from the confined gap at the epoxy/sample interface likely accelerated the corrosion at the edge of mounted samples.

In terms of the corrosion type, more IGC was present along the exposed surface under the higher cathode-to-anode area ratio. Figure 3. 26 and Figure 3. 27 show the details of IGC presence on the samples from 30:1 and 100:1 Ni to AA7075-T6 condition.

Figure 3. 28 summarizes the corrosion damage from the above images as a function of both the nature of the external cathode and cathode-to-anode area ratio. As shown in the figure, with a cathode-to-anode ratio of 1:1, it is clear that the damage caused by Ni cathode (103 µm) is comparable to the damage from the BMI external cathode (114 µm) This result indicates that the nature of the external cathode does not play a dominant role in the galvanically induced localized corrosion of AA7075-T6 in quiescent solutions.

Cathode-to-anode area ratio played an important role for the corrosion damage development, however. For the damage measured at the center of the sample, the damage increases slightly with the increase of the area ratio, from 103um (1:1) to 169 µm (100:1). At higher area ratios, the crevice corrosion at the edge of the sample caused severe damage, with a depth 459 µm for 60:1 and 564 µm for 100:1 respectively. The severe corrosion damage at the edge of the sample was likely due to the crevice corrosion within the narrow gap between the sample and the epoxy in which it was mounted.

3.3.3. Coupling Potential vs. Time as a function of Cathode/Anode Area Ratio in 0.6M NaCl

For the full immersion galvanic coupling tests discussed in 3.3.2, the coupling potential were monitored for each test condition over the entire exposure time. In Figure 3. 29, the potentials from AA7075-T6 -Ni full immersion galvanic coupling test with four cathode-to-anode area ratio are plotted as a function of exposure time. The initial galvanic potentials for cathode-to-anode area ratios of 1:1, 30:1, 60:1 and 100:1 were similar: -0.79V, -0.785V, -0.78V and -0.75V (vs SCE), respectively. For all the four curves, the potential initially increased with the time before reaching an initial steady-state after ca. 10,000 seconds of exposure. At the steady-state, the plateau potential for the four area ratio was -0.75V, -0.72V, -0.71V, -0.70V (vs SCE), respectively. The galvanic potential is relatively lower for the lower area ratios (cathode to anode 1:1 and 30:1), in agreement with expectations from mixed potential theory. At the higher cathode-to-anode area ratios (cathode to anode 60:1 and 100:1), a remarkable potential drop occurred after 30,000 seconds of exposure. The magnitude of the potential drop and recovery time varied with the area ratio. For the sample with area ratio of 60:1, the potential repeatedly dropped and recovered ranging from -0.70V to -0.8V (vs SCE). For the sample with an area ratio 100:1, the potential dropped to as low as -0.84V before fluctuating in a range of -0.7V to -0.74V (vs SCE).

3.3.4. Coupling Potential/Current Density vs. Time as a function of Cathode/Anode Area Ratio in 2.8 M NaCl

A solution of 2.8M NaCl was also used for full immersion galvanic testing of AA7075-T6 samples to study the galvanic corrosion damage of AA7075-T6 with a change in [Cl^-] with two cathode-to-anode area ratio, 1:1 and 100:1. Ni was used as the external cathode. Samples were exposed in the solution for 100 hours. In addition to measuring the effect of chloride concentration, 2.8M NaCl is the equilibrium chloride concentration for a solution at 90% relatively humidity (RH) , so the galvanic potential and corrosion damage from this test will also be compared with the results from 90% RH atmospheric exposure to validate the equivalency between the full immersion test and atmospheric exposure.

The galvanic current and potential over the exposure time for two area ratio conditions are shown in Figure 3. 30 and Figure 3. 31. Figure 3. 30 compares the galvanic current density between the two area ratios. For the 1:1 area ratio, the current density was initially $1.2x10^{-5}$ A/cm^2 and decreased slightly over the time, ending at $1x10^{-5}$ A/cm^2 after 300,000 sec. Some fluctuations were observed from 35,000secs to 58,000sec. The current density from the 100:1 area ratio was approximately 2 orders of magnitude higher than the one from cathode to anode 1:1, which agrees with the expectations from mixed potential theory. The curve is relatively smooth and no large fluctuation was observed. Figure 3. 31 shows the potential's distribution over the time for the two area ratio. For the lower area ratio (1:1), the initial value of galvanic potential is approximately -0.84V vs (SCE). The potential increased over the time and exhibited fluctuations from 35,000secs to 58,000sec, which matched with the current density fluctuations shown in Figure 3. 30. For the higher area ratio, the galvanic potential is stable at a range of -0.78V (vs SCE), slightly higher than the results from area ratio 1:1. With the longer exposure time, the potentials of 1:1 cathode-to-anode area ratio rose which may be due to a change of local chemistry over time. The galvanic potential and current for the sample with a 100:1 area ratio remained the same which indicate the stabilization of local chemistry through the rapid anodic dissolution.

3.3.5. Corrosion damage in 2.8M NaCl with different exposure times

The corrosion damage was measured using optical microscopy for both cathode-to-anode area ratios (1:1 and 100:1 conditions with Ni). Three exposure durations (33hrs, 66hrs, and 100 hrs) were selected. Both the effect of area ratio and test duration on the corrosion damage were investigated.

Figure 3. 32 to Figure 3. 34 shows the corrosion damage evolution for cathode to anode 1:1 area ratio over the time. As shown in Figure 3. 32, the damage in the initiation stage (33hrs) was not very remarkable. As shown in Figure 3. 33 , after 66hrs, an uneven surface was present due to the dissolution of material on the surface with a depth of 73 µm. The more obvious intergranular corrosion was present on the surface after 100 hours exposure in Figure 3. 34. The deepest pit was measured as 154 µm. Figure 3. 35 to Figure 3. 37 show the corrosion damage evolution over the time at cathode-to-anode area ratio 100:1. According to the images, after 33 hours exposure, the corrosion damage was minimal with the maximum damage being approximately

26 μm. After 66hrs exposure, an uneven exposed surface with a depth of 108 μm developed along the surface and appeared more severe from the 1:1 area ratio condition. After 100hours, more severe damage was observed with the deepest depth measured as 201 μm.

Similar measurements were made on the samples from 0.6M NaCl full immersion condition with the same exposure time intervals for comparison. Figure 3. 38 to Figure 3. 40 show the corrosion damage with Ni: AA7075-T6 1:1 area ratio. The deepest measured damage depth ranges from 0 μm, 44 μm and 88 μm for 33hrs, 66hrs and 100hrs, respectively. The damage in Ni: AA7075-T6 100:1 area ratio are shown in Figure 3. 41 to Figure 3. 43. The damage developed as 30 μm after 33hrs, 73 μm after 66hrs and 197 μm after 100hrs. Comparisons of the damage depth measurement from both 2.8M and 0.6M NaCl shows in Figure 3. 44. According to the figure, with the same exposure duration, the damage responses for different $[Cl^-]$ solution are different. After 33hrs of exposure, for the samples in 0.6M NaCl, almost no damage was observed, whereas for the samples in 2.8M NaCl, the damage is 26 μm and 30 μm for Ni: AA7075-T6 1:1 and 100:1 respectively. After 66hrs of exposure, damage was observed in both 0.6M NaCl and 2.8 NaCl. As shown in the figure, for Ni: AA7075-T6 1:1 condition, damage in 2.8M NaCl is 73 μm , which is much higher than the damage in 0.6M NaCl, measured as 44 μm . For Ni: AA7075-T6 100:1 condition, the damage depth 108 μm in 2.8M NaCl and 73 μm in 0.6M NaCl. After 100hours exposure, for Ni: AA7075-T6 1:1 condition, the depth for 2.8M NaCl and for 0.6M NaCl is 154 μm and 88 μm respectively. For Ni: AA7075-T6 100:1 condition, the depth for the two conditions are closer, measured as 201 μm for 2.8M NaCl and 197 μm for 0.6M NaCl.

3.3.6 Anodic Polarization of AA7075-T6 (with Ni, Cathode-to-anode area ratio: 1:1) in both 0.6M NaCl and 2.8M NaCl after 33hours/66hours/100hour

In order to understand the anodic kinetics of AA7075-T6 during the galvanic exposure (coupled with Ni), anodic polarizations were conducted on samples after the 33hrs, 66hrs and 100hrs in both 0.6M NaCl and 2.8M NaCl. The kinetic parameters extracted from this test will be applied as the boundary condition for the modelling study in chapter 4.

Figure 3. 45 and Figure 3. 46 show the anodic polarization in 2.8M NaCl and 0.6M NaCl. OCP and pitting potential are listed in Table 3.1. The measured OCP of the samples in 2.8M NaCl is -0.81V, -0.82V, and -0.84V (vs SCE) after 33hrs, 66hrs and 100hrs exposure, which is lower than the ones in 0.6M NaCl with the same condition. If compared with the anodic polarization of AA7075 artificial pit samples in $AlCl_3$, as listed in Table 2.5 from Chapter 2, the OCP of the samples in the NaCl is higher in general. These results matched with the galvanic potential observed in session 3.3.4 as it is easier to initiate corrosion on the AA7075-T6 in the higher [Cl^-] solution.

In Figure 3. 45, passive regions limited by pitting potentials were observed for the polarization curves in 2.8M NaCl. For 0.6M NaCl in Figure 3. 46, no passive region and only one pseudo-Tafel slope was present. Table 3.1 summarizes the electrochemistry kinetics parameters for the polarization curves for both 0.6 M NaCl and 2.8M NaCl.

3.4. Galvanic Coupling Testing in Atmospheric Condition

Galvanic coupling tests in atmospheric conditions were also performed. The damage as a function of coupling conditions (the selection of external cathode, the area ratio, exposure time, etc.) as well as the environmental conditions (relative humidity, water layer thickness) was studied. In addition, the SKP technique was used to measure the surface potential of AA7075-T6 after the exposure. The correlation between the corrosion damage and the potential was discussed to validate the applicability of E_{rp} measured under full immersion under the atmospheric conditions.

3.4.1. The Damage morphology as a function of Cathode-to-Anode Area, the selection of noble materials, the water layer thickness in RH 98% and RH 90%

The corrosion damage experienced by AA7075-T6 after galvanic atmospheric exposure was documented using optical microscopy of cross-sections. The results were used to quantify the corrosion damage under different test conditions including the cathode-to-anode area ratio, the selection of noble materials, the relative humidity (RH), and the water layer thickness.

Figure 3. 47 shows the corrosion damage along AA7075-T6 surface after 100hrs galvanic exposure under 98%RH and 90%RH. Ni was used as the external cathode. The cathode-to-anode area ratio 1:1 is discussed here. In both RH conditions, the most severe damage was observed on the interface closer to the cathode. When the position is distant from the cathode, the damage became minimal. For RH98%, the deepest pit measured was 203 μm. For RH90%, the deepest pit measured was 300μm.

The effects of the area ratio are shown in Figure 3. 48 for both Ni and BMI materials. Due to the limited material supplies, at the higher cathode-to-anode area ratio, the size of the anode sample was varied to achieve the desired valuedue to limited availability of some of the cathode materials. Figure 3. 48 shows the corrosion damage along AA7075-T6 surface when the area ratio and the material of external cathode changed. Figure 3. 48a-c show the corrosion damage on AA7075-T6 as a function of area ratio (with Ni). Similar to Figure 3. 47, the corrosion attack in all three cases is more intense at the cathode/anode interface. Both the corrosion damage at the cathode/anode interface and in the center of the samples were measured. In Figure 3. 48a, the corrosion damage depth measured for cathode-to-anode area ratio 100:1 is 723 µm at the interface and 403 µm in the center. In Figure 3. 48b, for cathode-to-anode area ratio 60:1, the damage is 707µm at the interface and 353µm in the center. In Figure 3. 48c, for cathode-to-anode area ratio 30:1, the deepest present in the middle of the sample, measured as 348 µm. Compared with the damage depth for the 1:1 area ratio (203µm), the deeper damage depth at the higher area ratio indicates that the corrosion damages increased with cathode-to-anode area ratio. Figure 3. 48d shows the corrosion damage when AA7075-T6 is coupled with BMI. The deepest corrosion damage measured here is 415µm at the interface and 234 µm in the center.

Figure 3. 49 shows the effect of water layer thickness on the corrosion damage of AA7075-T6 surface after the 100hrs galvanic exposure with Ni. The selected RH was 98% and the cathode-to-anode area ratio was 1:1. As shown in Figure 3. 49a, for 200um water layer thickness condition, the corrosion damage distributed primarily in two positions. One is at the location close to cathode to anode interface with the damage measured as 1054µm. Another is at the middle of exposed surface. The deepest damage is 604µm. For 150µm water layer thickness

condition in Figure 3. 49b, the corrosion damage was also found both at the cathode/anode interface and in the middle of the sample. The deepest depth for the damage at the interface is 345µm. In the middle of the sample, the damage is measured as 129µm. From Figure 3. 49c, the deepest damage from 100um water layer thickness is 203µm. The results indicated that the thicker water layer allowed more damage on the exposed surface. Also, with the thicker electrolyte, the damage was observed farther from the cathode/anode interface than with the thinner electrolyte.

Figure 3. 50 to Figure 3. 52, Figure 3. 53 to Figure 3. 55, and Figure 3. 56 to Figure 3. 58 show the detailed corrosion damage for each water layer condition, 200 µm, 150 µm and 100 µm, respectively. Both the damages at the cathode/anode interface and in the middle of the samples are shown in the figures.

3.4.2. The potential distribution along cathode/anode interface with RH 98%

In this section, two major issues will be addressed. The first issue is the measurement of the galvanic potential profile along the anode surface under the atmospheric exposure via SKP. Second, the measured galvanic potential and the damage morphology are compared to verify the effectiveness of E_{rp} measured from the previous full immersion condition in Chapter 2.

Figure 3. 59 shows the galvanic potential distribution along AA7075-T6 surface for a 1:1 cathode-to-anode area ratio with a water layer of 100 um under RH98%, after 100hours exposure coupled with a piece of Ni. The x-axis is the distance from the cathode/anode interface. As shown in the figure, the potential on the AA7075 decreased with distance from the interface

with cathode. Figure 3. 60 is repeated from Figure 3. 49c in the previous section 3.4.1. According to Figure 3. 60, corrosion damage decreased with distance from the interface with cathode. No damage was observed for areas > 0.5cm from the cathode interface. The corresponding potential (around -0.825 V vs SCE), is close to the E_{rp} measured in 0.6M NaCl. This agreement indicates the effectiveness of E_{rp} to predict the corrosion propagation under the atmospheric condition.

Using a similar approach, Figure 3. 61 to Figure 3. 63 illustrate the correlations between the surface potential and the corrosion damage along the exposure surface of AA7075-T6 when coupled with Ni and BMI external cathode with various cathode-to-anode area ratio. All samples were exposure for 100hrs with RH98%.

Figure 3. 61 a and b show the potential damages distribution along the AA7075-T6 surface coupled Ni with 100:1 area ratio. At the position closer to the cathode/anode interface (<0.05cm), the potential ranged from -0.77V to -0.79V vs SCE which corresponded to the most severe damage on the surface. The potential further decreased to -0.82V vs SCE when the surface is 0.25cm away from the interface. Fewer damages were observed in this lower potential region. Figure 3. 62 and Figure 3. 63 show the potential damage distribution of AA7075-T6 when coupled with Ni with 60:1 and 30:1 area ratio. A similar trend of potential distribution as that shown in Figure 3. 61 was found. In Figure 3. 62, the potential decreases when the surface is away from the exposed interface, as does the damage. In Figure 3. 63, the deepest damage was developed at the position 0.12cm away from the interface.

Figure 3. 64 summarizes the potential distributions as a function of the distance from the interface for galvanic coupling with different area ratios under atmospheric conditions. All samples were exposed to RH98% for 100 hrs. As shown in the figure, in general, the potential decreases with the increase of the distances from the cathode anode interface. The higher surface potential is present at the lower area ratio samples, which would seem to be contradictory with mixed potential theory. This disagreement will be discussed in the following discussion section.

3.4.4. The effect of exposure time on the potential distribution along AA7075 surface

Figure 3. 65 to Figure 3. 67 show the potential distribution along AA7075-T6 anode surface varying with the exposure time. Three cathode-to-anode area ratios (1:1, 30:1 and 60:1) were considered. In Figure 3. 65, after 1000 sec exposure, the higher the cathode-to-anode ratio, the higher potential, as expected from mixed potential theory. After 60 hrs exposure, as shown in Figure 3. 66, the higher ratios have fallen and are similar to one another. Figure 3. 67 shows that after 100hrs exposure, the potentials of the higher area ratio have dropped even more. More details to rationalize this observation will be discussed in the following section.

3.5. Discussion

3.5.1. Using 250uA/cm^2 as a thresholds current density for E_{rp} Measurements

Figure 3. 68 shows the E_{rp} value with different measurement methods. The first four E_{rp} values were measured from full immersion testing, according to Figure 2.10 and Figure 2.11 in Chapter 2. The first two measurements compare the E_{rp} for artificial pit samples with two different threshold current densities. . E_{rp} ranges from -0.82V to -0.93V vs SCE for 250uA/cm^2, and -0.94V to -0.98V vs SCE for 50uA/cm^2, respectively. The next two measurements compare the

E_{rp} for bulk samples with two different threshold current densities, ranging from -0.85V to -0.94V for 250uA/cm^2 and -0.92V to -0.99V for 50uA/cm^2, respectively. The remaining three $E_{rp,}$ were measured for validation purposes, and were attained through current decay testing (Figure 2.39), i*x measurements (Figure 2.37) and SKP measurements of atmospheric exposed sample (Figure 3. 59). The E_{rp} using 250uA/cm^2 as a threshold current density is closer to the values from validation data, which indicates it is a better threshold for identifying $E_{rp.}$

3.5.2. The effect of [Cl$^-$]

Figure 3. 44 shows the corrosion damage for Ni-AA7075-T6 with 1:1 cathode-to-anode area ratio with full immersion condition. For the three exposure time, 33hrs, 66hrs, 100hrs, the corrosion damage in 2.8M NaCl solution is deeper. Similarly, in Figure 3. 69, the corrosion damage in RH90%, which is equivalent to 2.8M NaCl in the full immersion condition, is deeper. The exposure to higher [Cl-] changes the kinetics of localized corrosion and causes more intensive corrosion damage.

In addition, for the full immersion coupling condition, compared the galvanic potential of 0.6M NaCl and 2.8M NaCl in Figure 3. 29 and Figure 3. 31, the galvanic potential under 2.8M NaCl solution, given the same area ratio (1:1) and external cathode (Ni), is lower than the one in 0.6M NaCl. This difference is caused by the lower OCP in the higher [Cl$^-$] solution.

3.5.3. Comparison of corrosion damage for different cathode materials

The effect of the nature of the cathode material is discussed here by comparing the corrosion damage depth of BMI-AA7075-T6 system to that of the Ni-AA7075-T6 system as shown in

Figure 3. 69. For a cathode-to-anode 1:1 area ratio, under full immersion, the maximum damage depth for BMI is 153µm whereas for Ni it is 144 µm. At RH98%, the depth for BMI is 162 µm and for Ni is 139µm. For cathode-to-anode 30:1 area ratio, at RH98%, the depth for Ni is 416µm and for BMI is 415µm. Thus, there are no remarkable differences with the change of cathode material between Ni and BMI regardless of exposure conditions. This similarity is likely due to the similar cathodic kinetics of Ni and BMI at the region of coupling potential. The more detailed cathodic kinetics is characterized in Chapter 4.

The effect of electrolyte thickness

A thin layer of electrolyte was selected to simulate the atmospheric exposure conditions. By knowing the RH and loading density, for a constant exposure area, the desired electrolyte thickness can be achieved by applying 0.6M NaCl on the exposed area.

As shown in Figure 3. 70, with the same RH (RH98%), the damage depths for electrolyte layers of 100µm, 150µm and 200µm are 139 µm, 315 µm, and 523 µm, respectively.

The thicker electrolyte thickness results in a deeper depth of corrosion damage. With a thicker electrolyte at constant RH, the ohmic drop between anode and cathode is reduced. The RH sets the concentration and thus the conductivity, but a thicker electrolyte layer leads to a lower resistance. This lower resistance allows more severe corrosion attacks with the same exposure area. The somewhat greater damage at RH90% vs. RH98% for the 100µm electrolyte layer is due to the increase in solution conductivity at the lower RH (due to the higher chloride concentration).

Two extreme conditions are discussed here to frame the circumstances involved in diurnal cycles. First, when the RH falls, the surface equilibrium is disturbed, the electrolyte on the surface must thin in order to create a more concentrated electrolyte as required by thermodynamics. The decreasing of thickness will cause a higher ohmic drop across the cathode-to-anode exposure surface, which will further lower the potential on the anode site. The higher concentration of electrolyte increase the conductivity of the electrolyte, however, the impact is not as great as the change the thickness. With a thin layer of electrolyte, the cathode reaction of oxygen reduction is diffusion controlled; the diffusion limited current density is a function of the solubility of oxygen in the electrolyte and the electrolyte thickness.

While the thickness increases with an increase in the loading density at a given RH, the resistance of the electrolyte is lowered, and the cathodic reaction is similar to its reaction in the bulk solution.

3.5.4. The comparison of corrosion damage with different cathode-to-anode area ratio

Figure 3. 71 summarize the measured corrosion damages under both full immersion (0.6M NaCl) and atmospheric conditions (RH98%) with different cathode to anode area ratios. These two conditions are compared because 0.6M NaCl is the equilibrium concentration of chloride for an atmosphere of RH98% at room temperature.

As shown in the figure, for both full immersion and atmospheric condition, the depth of corrosion damage increases with an increase of cathode-to-anode area ratio. At higher cathode-to-anode area ratio (≥60), the degree of increase is less than the ones with lower cathode-to-anode area ratio, i.e., a damage depth plateau at the higher cathode-to-anode area ratio is observed. The corrosion products generated during the full immersion condition is likely a controlling factor for the damage depth plateau observed. The potential changes over time in Figure 3. 29 support this rationale. At the higher area ratio, initially, the higher galvanic potential accelerated the corrosion reaction on the sample surface and caused the saturation of the solution with respect to aluminum ions, and the formation of corrosion products. The accumulation of corrosion products covered the exposed surface and created a significant ohmic drop. The big potential drop was thus observed according to Figure 3. 29. Consequently, the corrosion reaction rate slowed due to the potential changes. The dissolution of corrosion products from less saturated solution then removed the ohmic drop and the potential recovered to the higher level. At a higher potential level, the cycle may repeat. This potential drop is more significant for the sample with area ratio 100:1 since the initial potential and corrosion rate are higher. The drop of potential slowed the average corrosion rate and inhibited the corrosion damage, which made the damage comparable to samples with area ration 60:1.

3.5.5. Comparison of corrosion damage for full immersion and atmospheric condition.

According to Figure 3. 71, for the cathode-to-anode condition 30:1, 60:1 and 100:1, the depth caused by corrosion damage with atmospheric condition at RH98% is somewhat deeper than the ones under full immersion condition for 0.6M NaCl.

Similarly, with 1:1 cathode-to-anode area ratio (same electrolyte thickness 100µm), the depth of AA7075-T6 coupled with Ni in 2.8M NaCl, which is shown as 200 µm in Figure 3. 44, is slightly deeper than the one in RH90%, shown as 240µm in Figure 3. 70.

The more severe attacks from the atmospheric condition compared with full immersion condition may be caused by the following reasons. First, the atmospheric condition was a planar geometry under which cathode and anode are connected together. The local chemistry change during the exposure thus may affect the anode site more directly. Second, with a thin electrolyte, the supply of cathode current is stronger and therefore accelerates the anodic dissolution as $i_{cathode}=i_{anode}$ with the same given exposed area. Third, to prevent the solution drying out, more solution was added upon the cathode-anode surface for the atmospheric exposure condition, which may increase the solution concentration for the long-term exposure.

3.5.6. Comparison of corrosion damages with different exposure time

According to mixed potential theory as shown in chapter 1, Figure 1.1, for a given anodic polarization curve, the larger the cathode-to-anode area ratio, the higher the coupling potential. However, for the atmospheric exposure of Ni-AA7075-T6, as shown in Figure 3. 65, Figure 3. 66 and Figure 3. 67, the coupling potential for 30:1, 60:1 and 100:1 cathode-to-anode area ratio varies with the exposure time from 1000s to 100hours.

This disagreement is likely due to the formation of corrosion products, causing the effective area ratio to change, or an increase in the resistance of the solution layer due to the corrosion products. This result also can be used for the boundary condition in the time-dependent modelling study.

3.5.7. Effectiveness of E_{rp} for the galvanic coupling condition

The galvanic potential with different coupling potential under both full immersion and atmospheric condition in this chapter is compared with the E_{rp} measured in Chapter 2 to verify the effectiveness of E_{rp} when AA7075 coupled with noble materials. Mizuno [6] has established a potential-dependent IGC for AA5083 in his recent research, by comparing the damage from cathode-free potentiostatic holding and galvanic coupling tests. He thus also successfully predicts the damage-free region where the potential is lower than E_{rp}. In the present research, the damage from potentiostatic holding -0.67V to-0.65V, shown in Figure 3. 6 to Figure 3. 8, is minimal. The holding potential is much higher than E_{rp} from measurements in Chapter 2. However, under the galvanic condition as shown in Figure 3. 29, the coupling potential with various cathode-to-anode area ratio is lower, ranged from -0.84V to-0.68V vs SCE. The corrosion damages are still developed even under the region the potential is lower than -0.67V. This may be caused by the different exposure time. The duration of potentiostatic holding is 3 hours. While for the galvanic coupling, it is up to 100hours. Incubation time for the potentiostaic holding may be required for a corrosion attack as remarkable as the ones in the galvanic corrosion condition.

The effectiveness of E_{rp} under the atmospheric condition is also validated as shown in Figure 3. 59 and Figure 3. 60, by comparing the highest potential of damage free area with E_{rp}. The application of E_{rp} as a stability criteria and the feasibility of measuring the potential of corroding surface with a thin electrolyte layer benefits the precise predication of atmospheric-related corrosion.

Reference

[1] J. X. Jia, G. Song, a. Atrens, *Adv. Eng. Mater.* 2007, *9*, 65.

[2] N. Murer, R. Oltra, B. Vuillemin, O. Néel, *Corros. Sci.* 2010, *52*, 130.

[3] F. Thébault, B. Vuillemin, R. Oltra, K. Ogle, C. Allely, *Electrochim. Acta* 2008, *53*, 5226.

[4] J. F. Dante, J. Averett, F. Friedersdorf, C. Vestal, *Internal Report*, n.d.

[5] D. A. Jones, B. E. Wilde, *Corrosion Sci.* 1978, *18, 631*

[6] D. Mizuno, R.G. Kelly, Corrosion, submitted (Aug, 2012)

[7] Z. Feng, G. S. Frankel, *Corrosion,* 2014, *70*, 95.

[8] Z. Chen, F. Cui, R. G. Kelly, *ECS Trans.* 2007, *3*, 443.

	OCP (V vs SCE)		Pitting Potential (V vs SCE)	
	0.6M	2.8M	0.6M	2.8M
33hrs	-0.74	-0.81	N/A	-0.76
66hrs	-0.76	-0.82	N/A	-0.58
100hrs	-0.8	-0.84	N/A	-0.58

Table 3. 1

Electrochemistry Kinetics from the anodic polarization in both 0.6 M and 2.8M NaCl. AA7075-Ni, area ratio 1:1

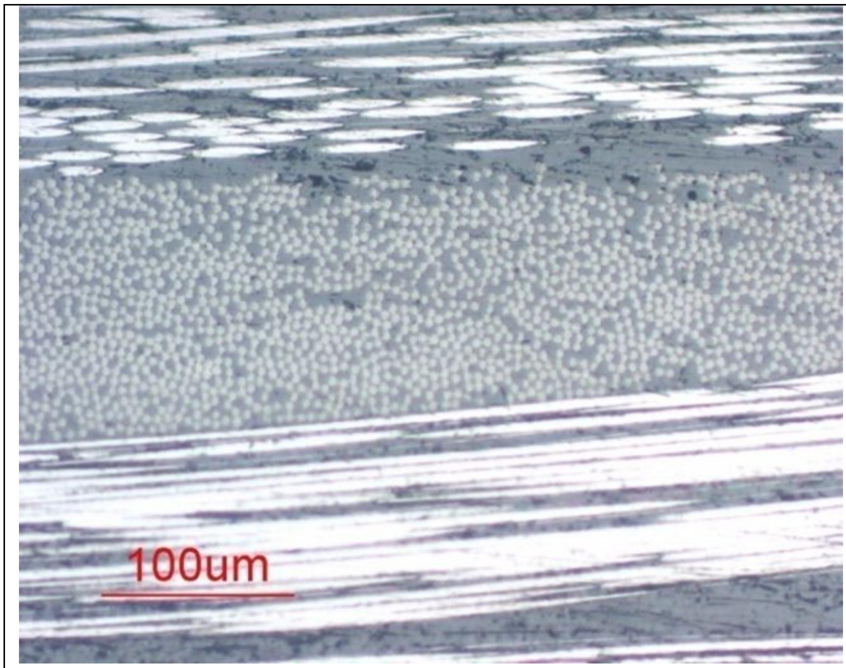

Figure 3. 1

SEM microstructure of BMI, the blue part is the polymer matrix and the white part (two directions) is the carbon fibers.

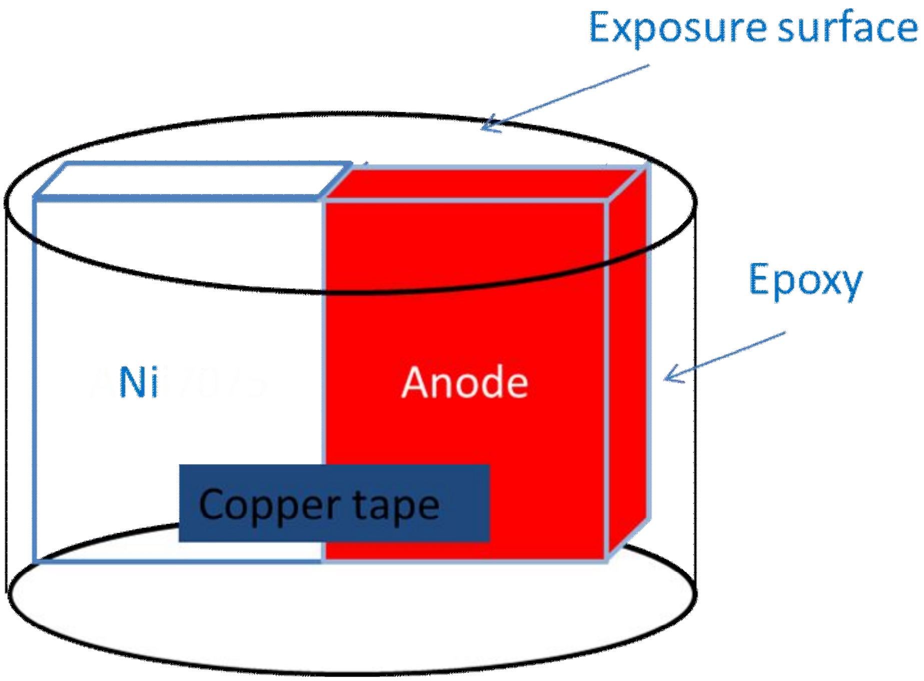

Figure 3. 2

Schematic of the galvanic corrosion atmospheric exposure sample

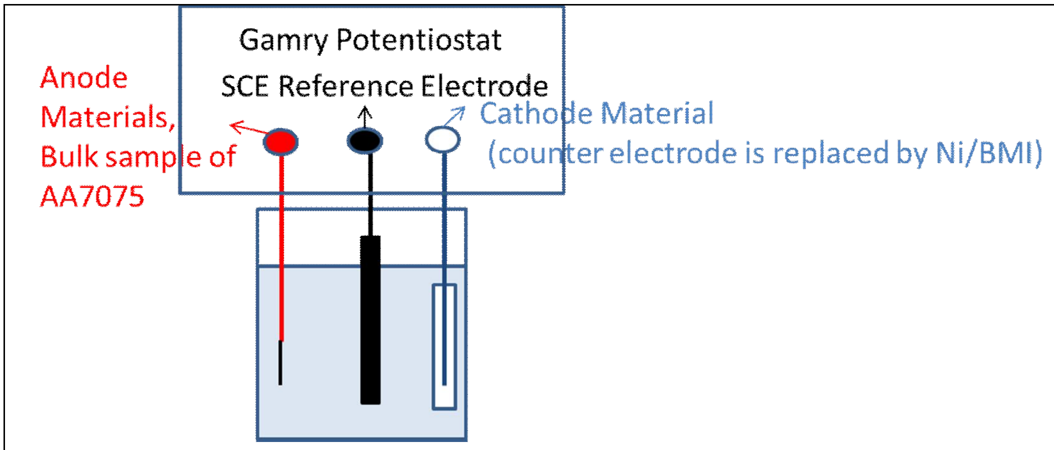

Figure 3. 3

Schematic of the galvanic corrosion full immersion test system, the cathode material replaced the Pt counter electrode that is used in potentiostatic and potentiodynamic polarizations

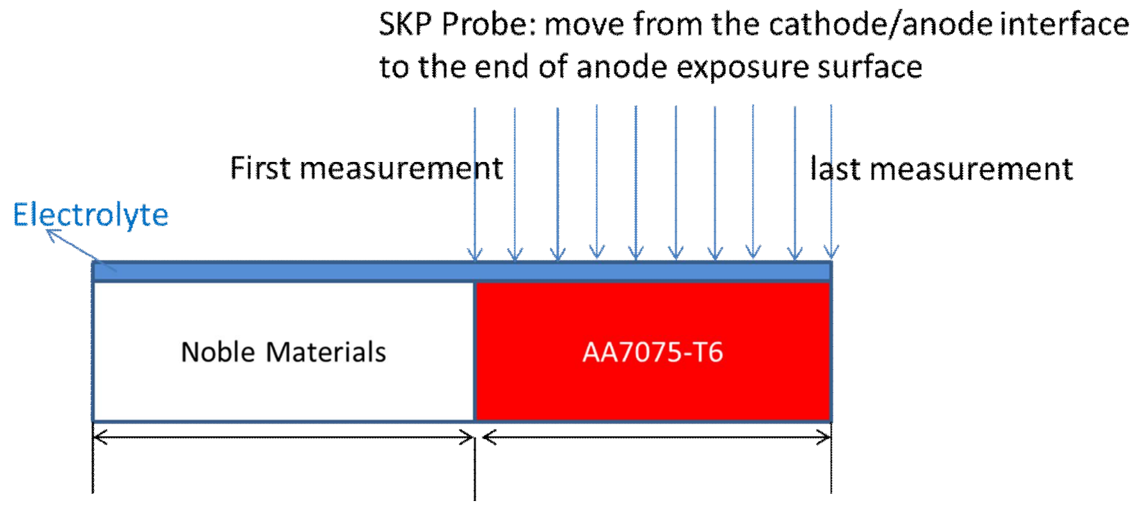

Figure 3. 4

Schematic of the galvanic corrosion atmospheric exposure

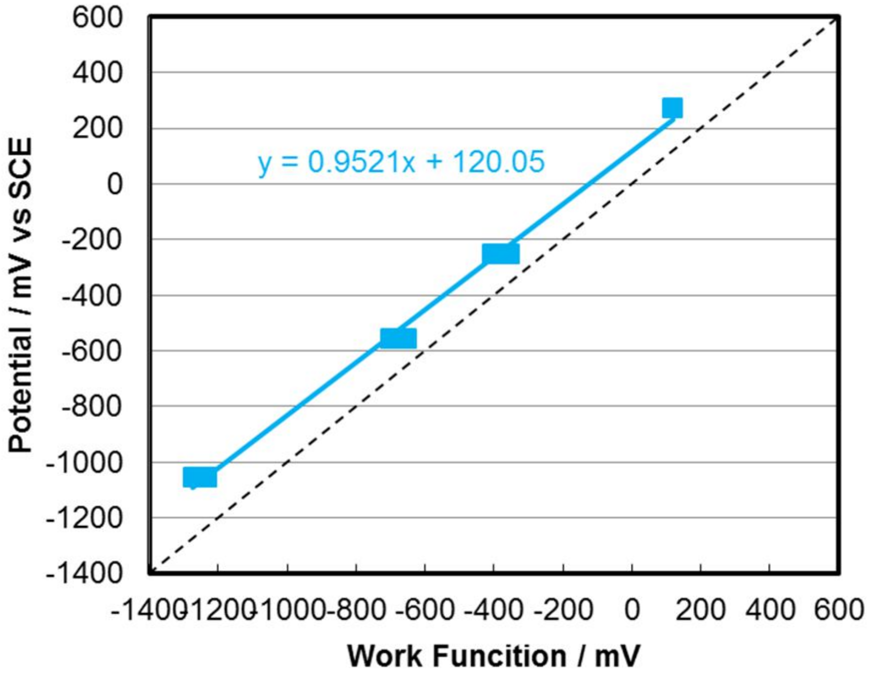

Figure 3. 5

The relationship between corrosion potential and WF through calibration tests

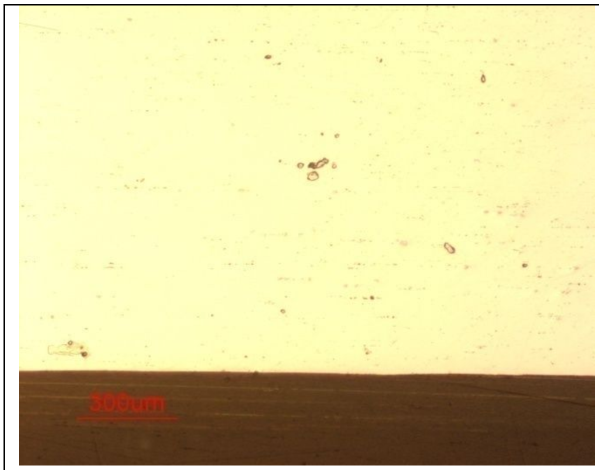 Figure 3. 6	 Figure 3. 7
Corrosion damage on AA7075-T6 under 0.6M NaCl full immersion condition, with potentiostatic holding for 3 hours at-0.67V vs SCE	Corrosion damage on AA7075-T6 under 0.6M NaCl full immersion condition, with potentiostatic holding for 3 hours at-0.66V vs SCE
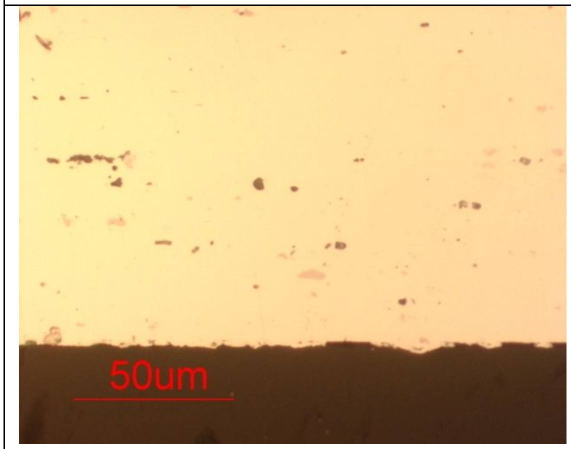 Figure 3. 8	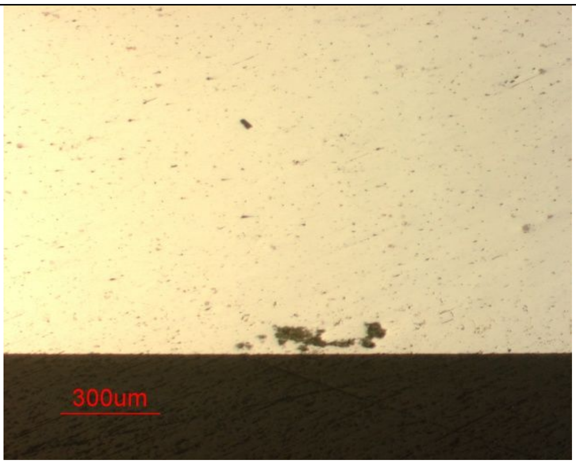 Figure 3. 9
Corrosion damage on AA7075-T6 under 0.6M NaCl full immersion condition, with potentiostatic holding for 3 hours at-0.65V vs SCE	Corrosion damage on AA7075-T6 under 0.6M NaCl full immersion condition, with potentiostatic holding for 3 hours at-0.64V vs SCE

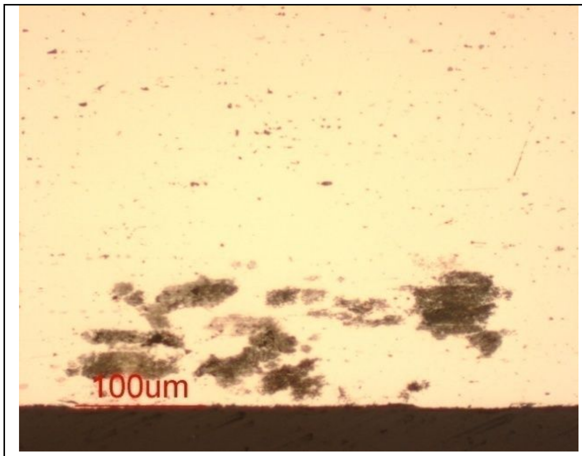 Figure 3. 10	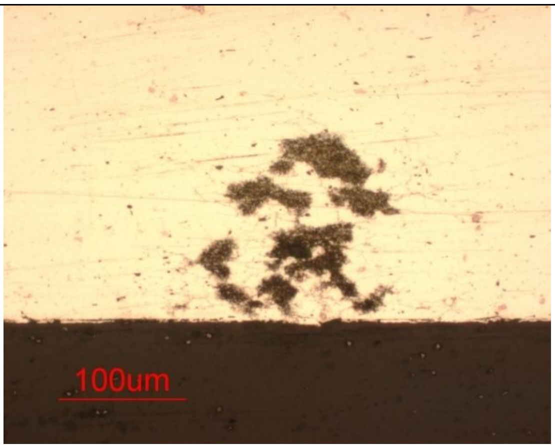 Figure 3. 11
Corrosion damage on AA7075-T6 under 0.6M NaCl full immersion condition, with potentiostatic holding for 3 hours at-0.63V vs SCE	Corrosion damage on AA7075-T6 under 0.6M NaCl full immersion condition, with potentiostatic holding for 3 hours at-0.62V vs SCE
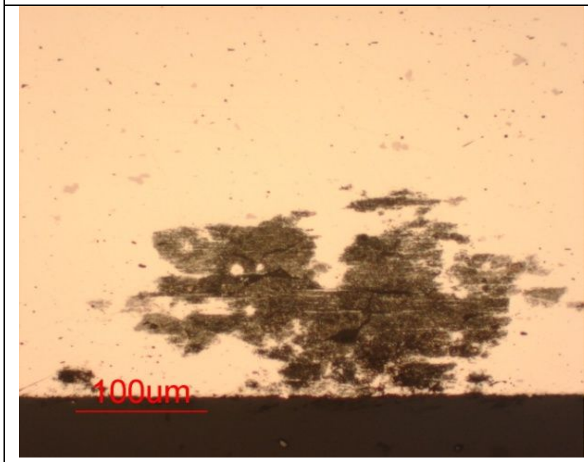 Figure 3. 12	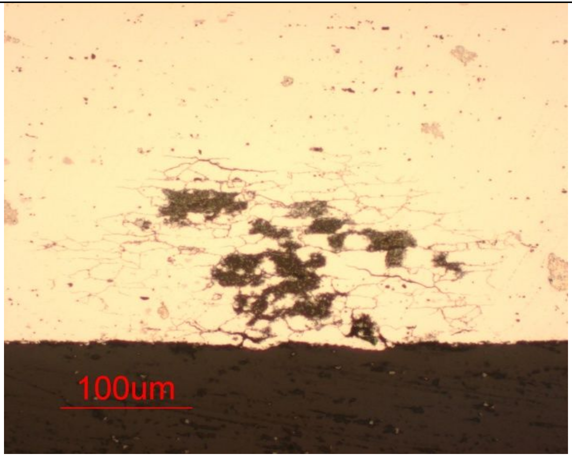 Figure 3. 13
Corrosion damage on AA7075-T6 under 0.6M NaCl full immersion condition, with potentiostatic holding for 3 hours at-0.61V vs SCE	Corrosion damage on AA7075-T6 under 0.6M NaCl full immersion condition, with potentiostatic holding for 3 hours at-0.60V vs SCE

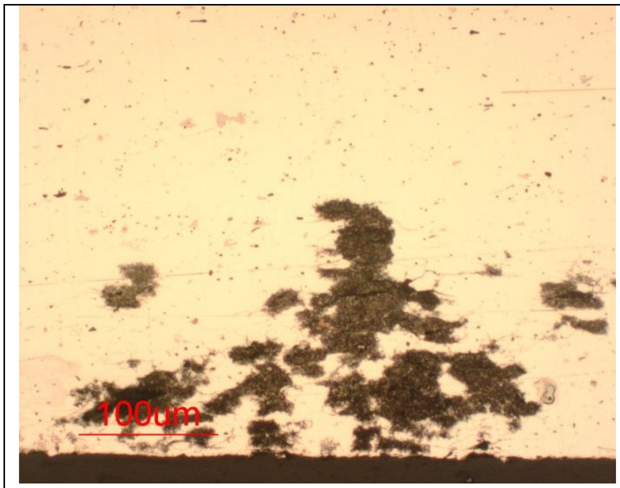

Figure 3. 14

Corrosion damage on AA7075-T6 under 0.6M NaCl full immersion condition, with potentiostatic holding for 3 hours at-0.59V vs SCE

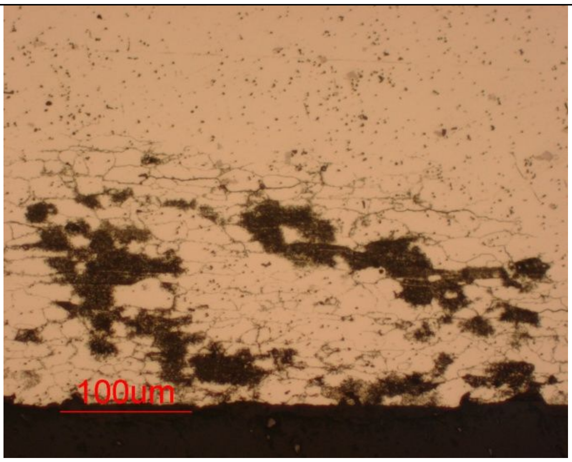

Figure 3. 15

Corrosion damage on AA7075-T6 under 0.6M NaCl full immersion condition, with potentiostatic holding for 3 hours at-0.58V vs SCE

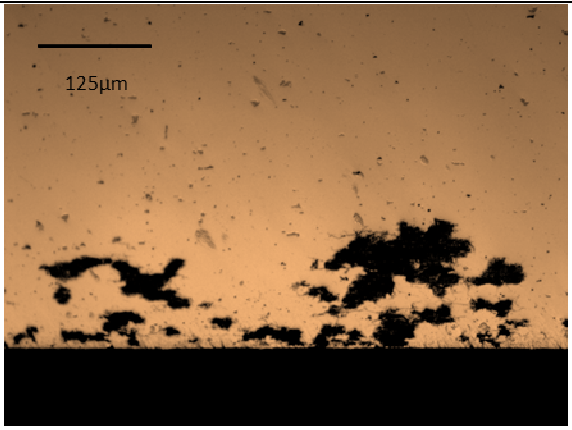

Figure 3. 16

Corrosion damage on AA7075-T6 under 0.6M NaCl full immersion condition, with potentiostatic holding for 3 hours at-0.57V vs SCE

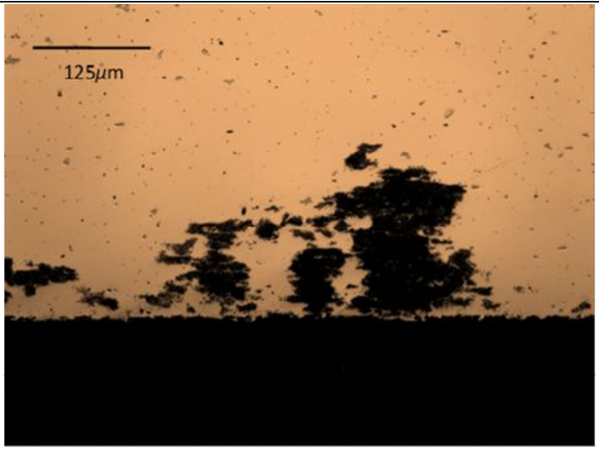

Figure 3. 17

Corrosion damage on AA7075-T6 under 0.6M NaCl full immersion condition, with potentiostatic holding for 3 hours at-0.56V vs SCE

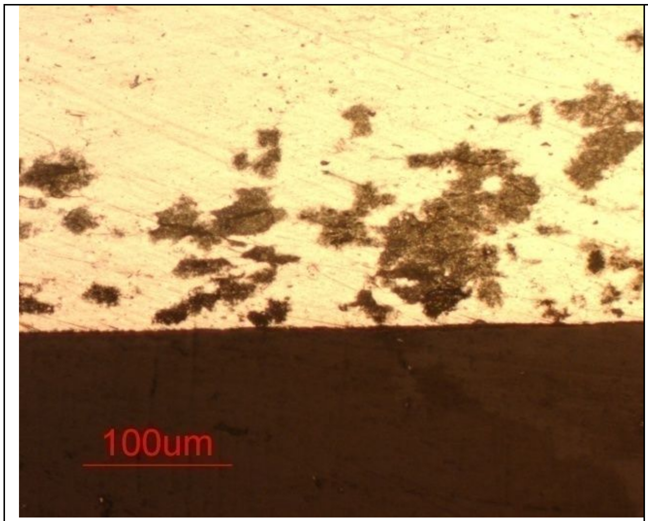

Figure 3. 18

Corrosion damage on AA7075-T6 under 0.6M NaCl full immersion condition, with potentiostatic holding for 3 hours at-0.55V vs SCE

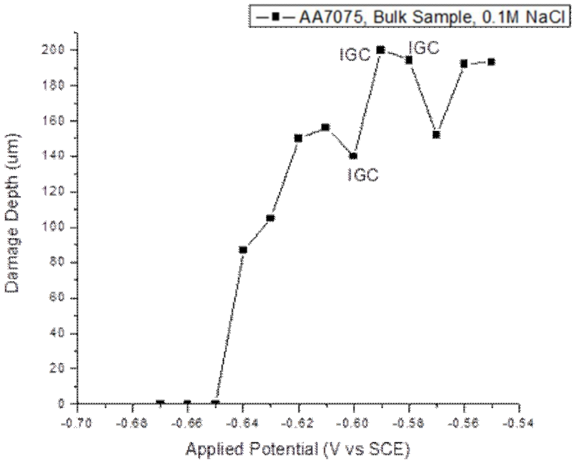

Figure 3. 19

Corrosion damage on AA7075-T6 in 0.6M NaCl condition, with potentiostatic holding for 3 hours, -0.67V to -0.55V vs SCE

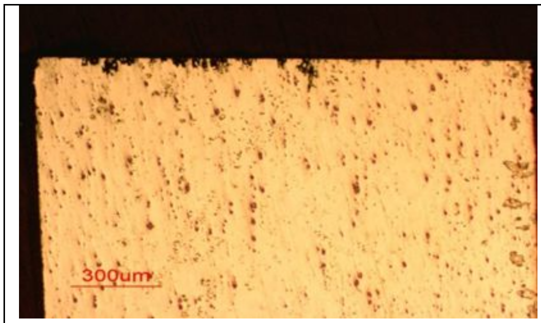 Figure 3. 20	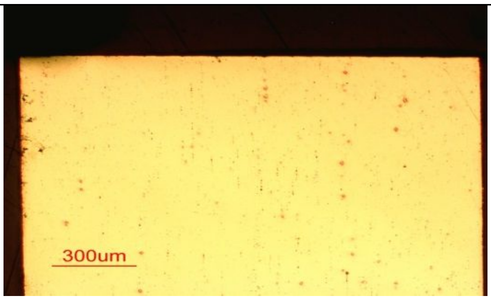 Figure 3. 21
The damage morphology of AA7075-T6 coupled with BMI at 1:1 cathode-to-anode area ratio in 0.6M NaCl after 100 hours exposure.	The damage morphology of AA7075-T6 without external cathode in 0.6M NaCl after 100 hours exposure.
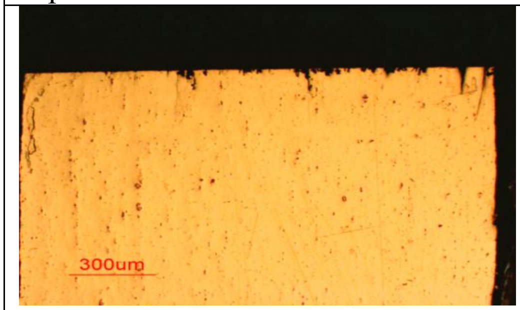 Figure 3. 22	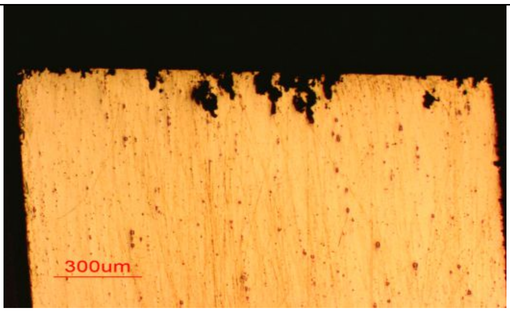 Figure 3. 23
The damage morphology of AA7075-T6 coupled with Ni at 1:1 cathode-to-anode area ratio in 0.6M NaCl after 100 hours exposure.	The damage morphology of AA7075-T6 coupled with Ni at 30:1 cathode-to-anode area ratio in 0.6M NaCl after 100 hours exposure.
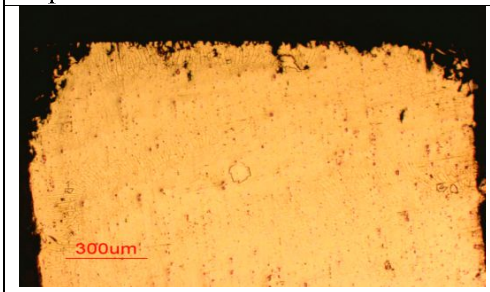 Figure 3. 24	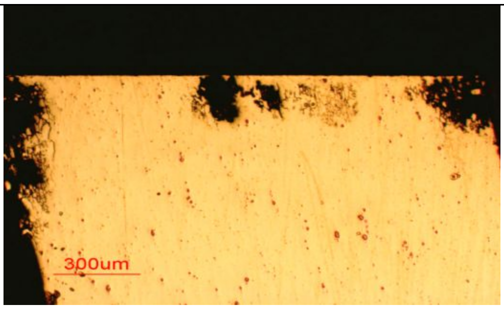 Figure 3. 25
The damage morphology of AA7075-T6 coupled with Ni at 60:1 cathode-to-anode area ratio in 0.6M NaCl after 100 hours exposure.	The damage morphology of AA7075-T6 coupled with Ni at 100:1 cathode-to-anode area ratio in 0.6M NaCl after 100 hours exposure.

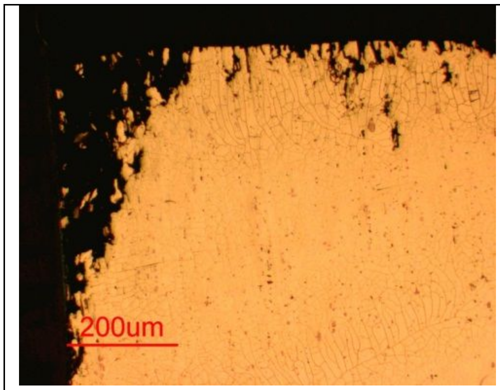 Figure 3. 26	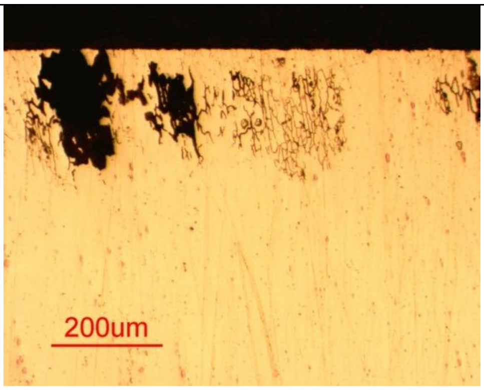 Figure 3. 27
The damage morphology of AA7075-T6 coupled with Ni at 60:1 cathode-to-anode area ratio in 0.6M NaCl after 100 hours exposure, higher magnification.	The damage morphology of AA7075-T6 coupled with Ni at 100:1 cathode-to-anode area ratio in 0.6M NaCl after 100 hours exposure, higher magnification.

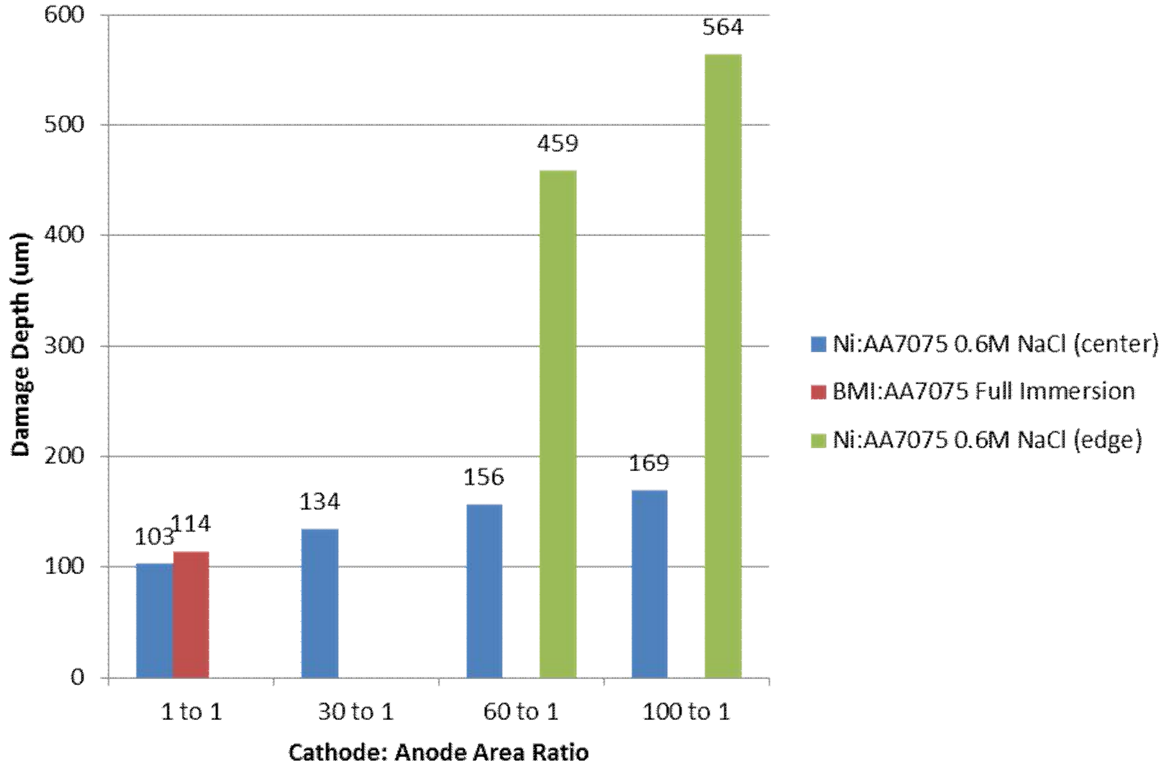

Figure 3. 28

The damage morphology of AA7075-T6 as a function of Cathode/Anode Area and selection of Noble Materials in 0.6M NaCl after 100 hours exposure

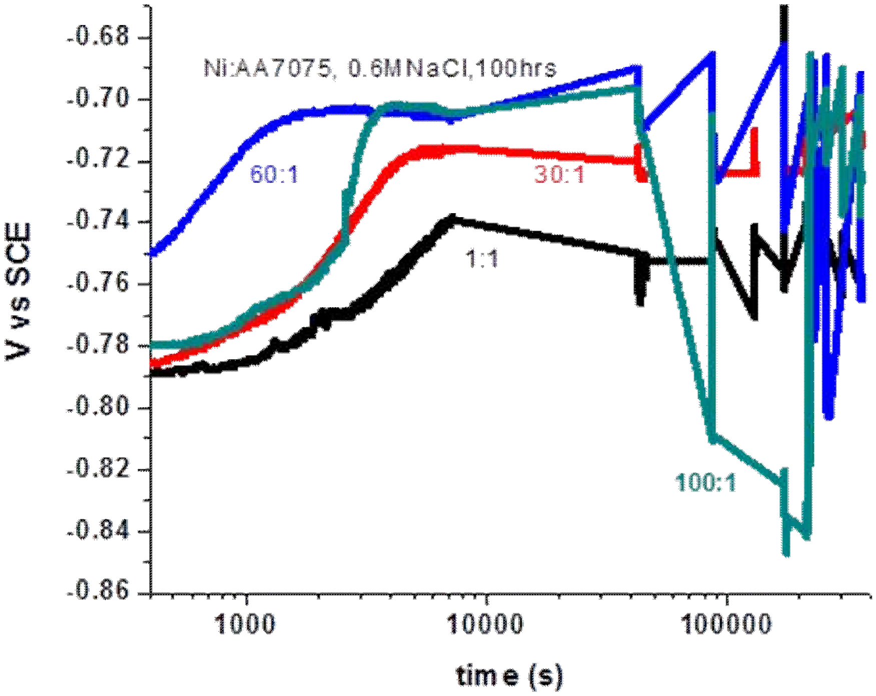

Figure 3. 29

Galvanic potential vs. time as a function of cathode-to-anode area ratio for AA7075-T6 with Ni in 0.6M NaCl, after 100hrs exposure

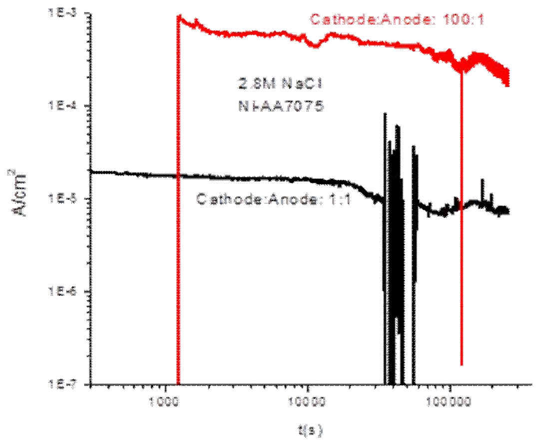

Figure 3. 30

Current density vs. time for A7075-T6 with Ni as a function of Cathode-to-Anode Area Ratio in 2.8 M NaCl

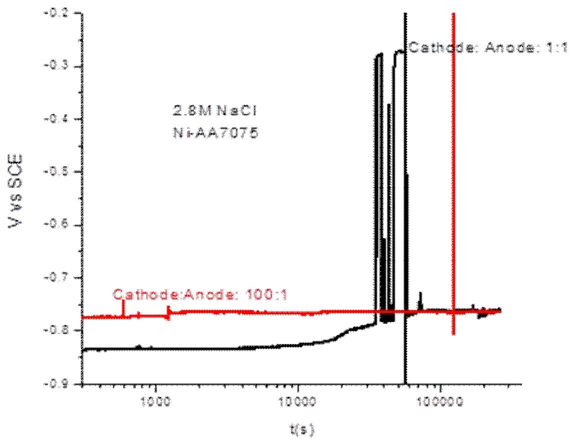

Figure 3. 31

Coupling Potential vs. Time for A7075-T6 with Ni as a function of Cathode-to-Anode Area Ratio in 2.8 M NaCl

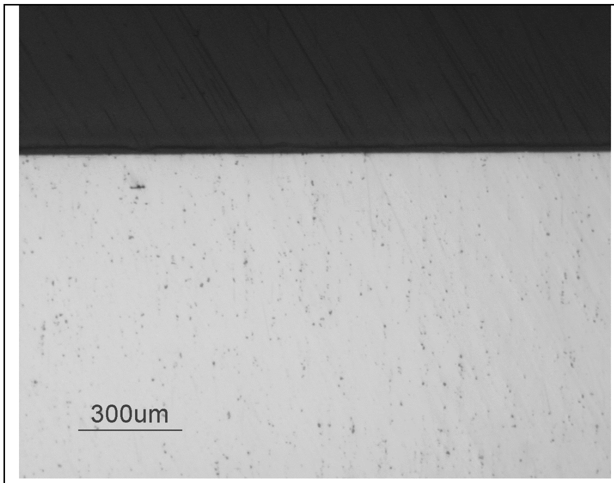 Figure 3. 32	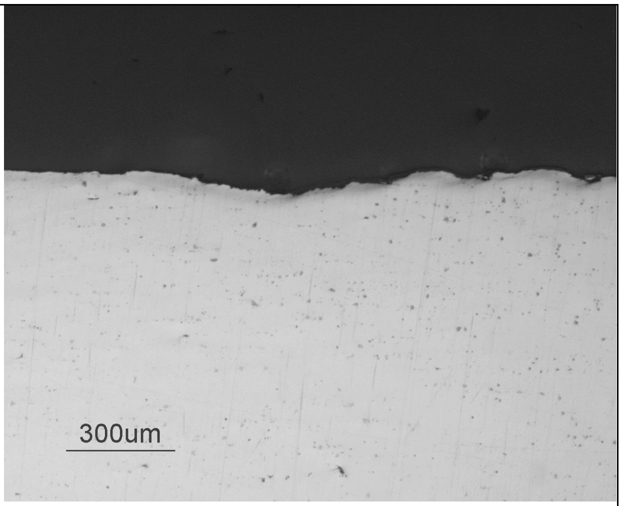 Figure 3. 33
The corrosion damage in 2.8M NaCl with 33hrs exposure for AA7075-T6 with Ni, at 1:1 cathode-to-anode area ratio	The corrosion damage in 2.8M NaCl with 66hrs exposure for AA7075-T6 with Ni , at 1:1 cathode-to-anode area ratio
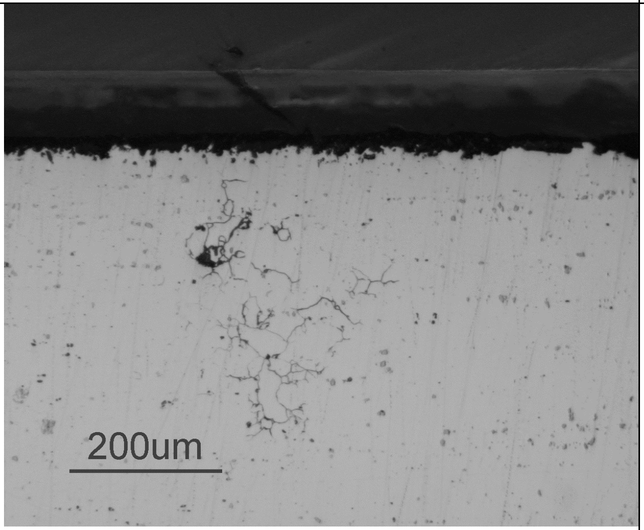 Figure 3. 34	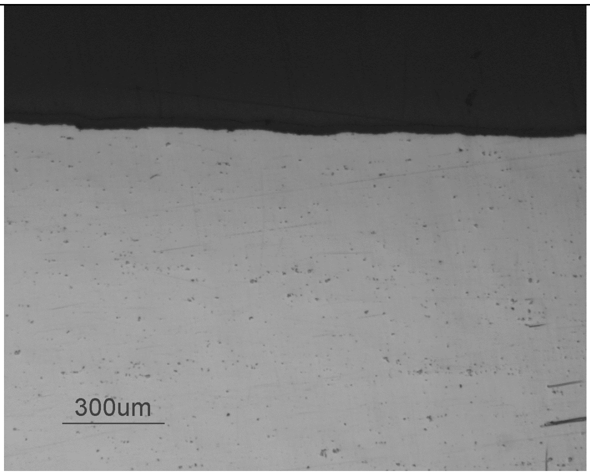 Figure 3. 35
The corrosion damage in 2.8M NaCl with 100hrs exposure for AA7075-T6 with Ni , at 1:1 cathode-to-anode area ratio	The corrosion damage in 2.8M NaCl with 33hrs exposure for AA7075-T6 with Ni , at 100:1 cathode-to-anode area ratio

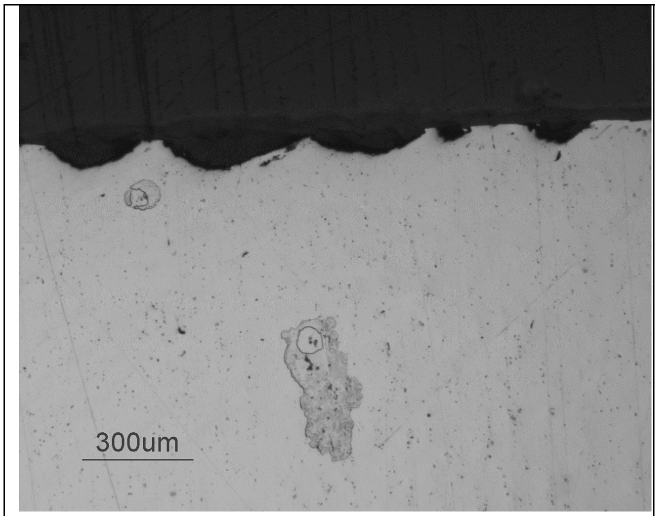 Figure 3. 36	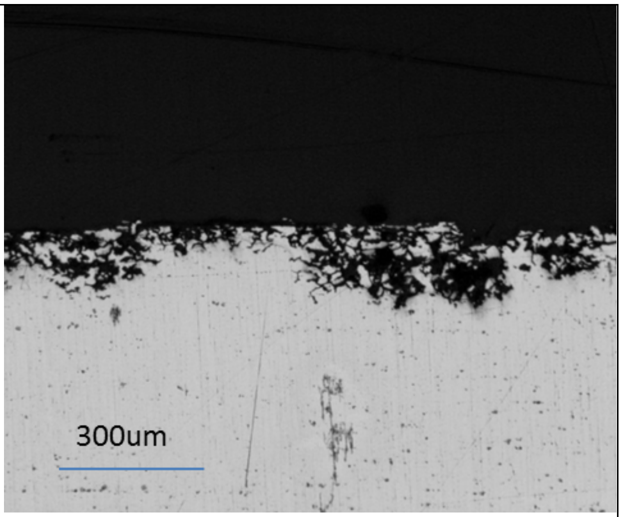 Figure 3. 37
The corrosion damage in 2.8M NaCl with 66hrs exposure for AA7075-T6 with Ni , at 100:1 cathode-to-anode area ratio	The corrosion damage in 2.8M NaCl with 100hrs exposure for AA7075-T6 with Ni , at 100:1 cathode-to-anode area ratio

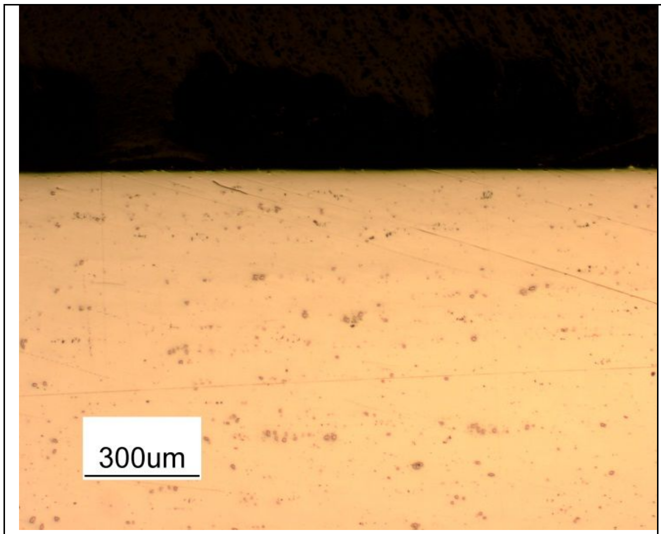 Figure 3. 38	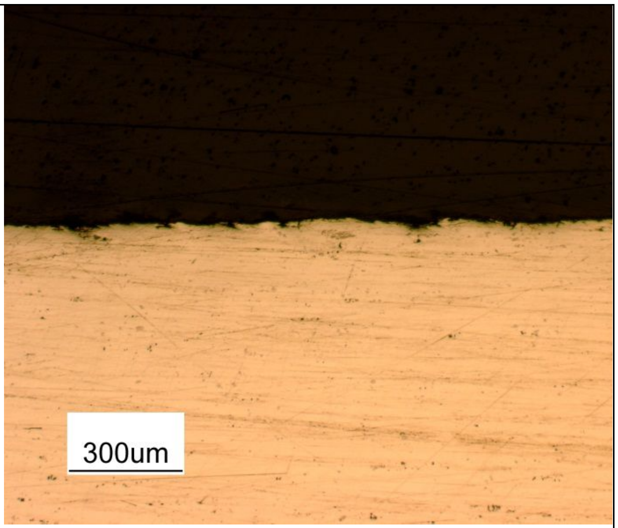 Figure 3. 39
The corrosion damage in 0.6M NaCl with 33hrs exposure for AA7075-T6 with Ni , at 1:1 cathode-to-anode area ratio	The corrosion damage in 0.6M NaCl with 66hrs exposure for AA7075-T6 with Ni , at 1:1 cathode-to-anode area ratio
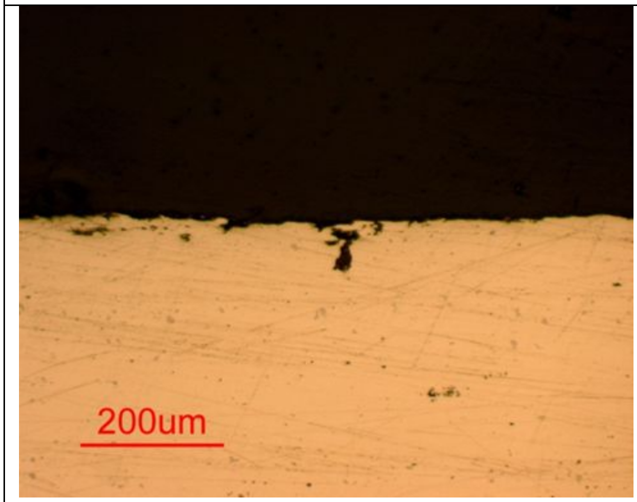 Figure 3. 40	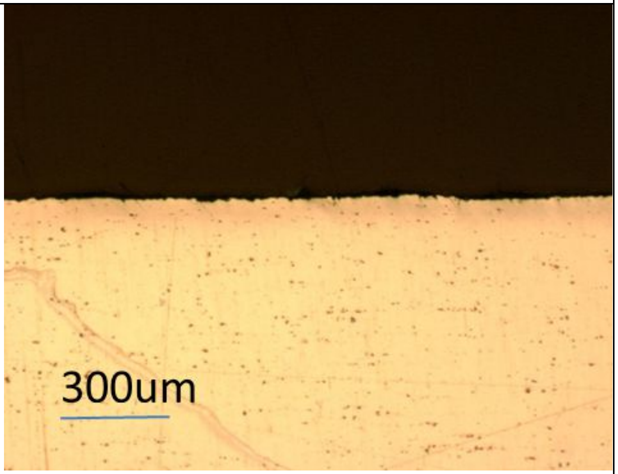 Figure 3. 41
The corrosion damage in 0.6M NaCl with 100hrs exposure for AA7075-T6 with Ni , at 1:1 cathode-to-anode area ratio, higher magnification for illustrate the damage details.	The corrosion damage in 0.6M NaCl with 33hrs exposure for AA7075-T6 with Ni , at 100:1 cathode-to-anode area ratio

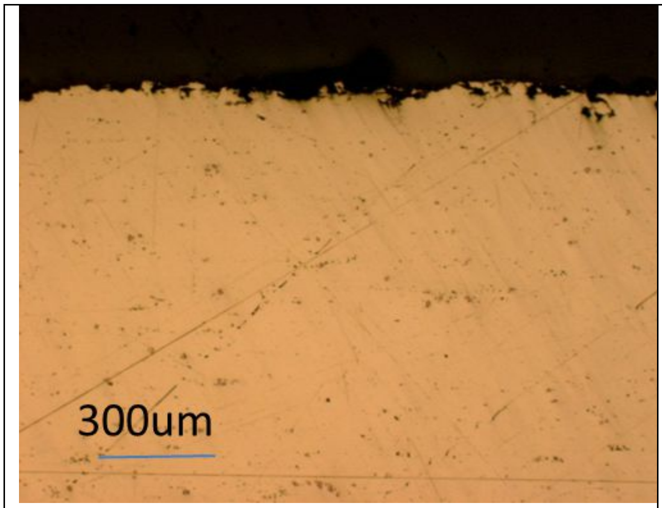 Figure 3. 42	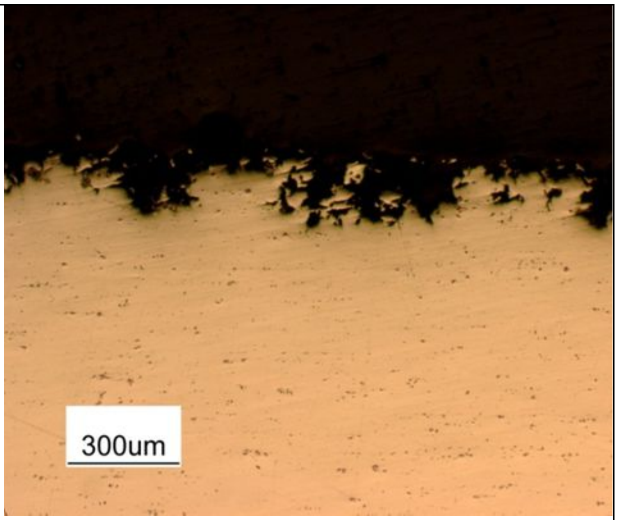 Figure 3. 43
The corrosion damage in 0.6M NaCl with 66hrs exposure for AA7075-T6 with Ni , at 100:1 cathode-to-anode area ratio	The corrosion damage in 0.6M NaCl with 100hrs exposure for AA7075-T6 with Ni , at 100:1 cathode-to-anode area ratio

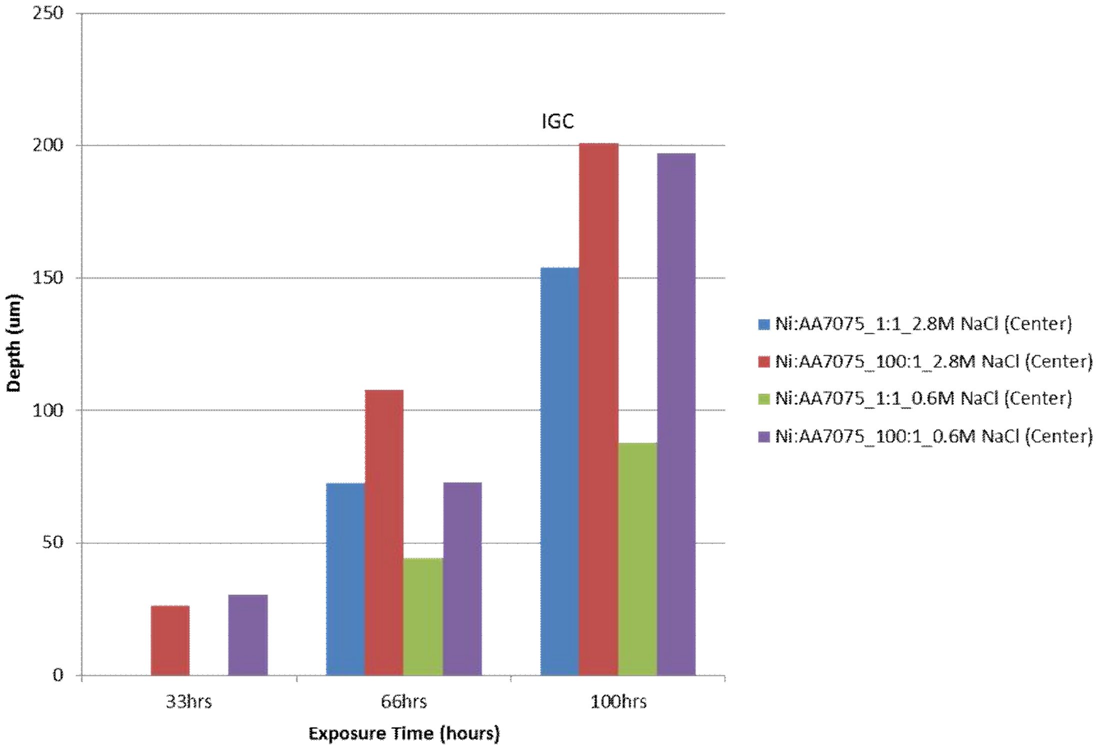

Figure 3. 44

The corrosion damage in 0.6M NaCl with different exposure times for AA7075-T6 coupled to Ni

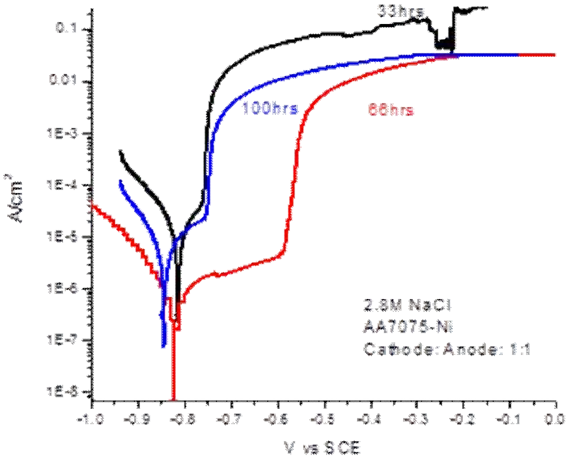

Figure 3. 45

Anodic Polarization of AA7075-T6 (with Ni, Cathode-to-Anode Area Ratio: 1:1 in 2.8M NaCl after 33hours/66hours/100hours

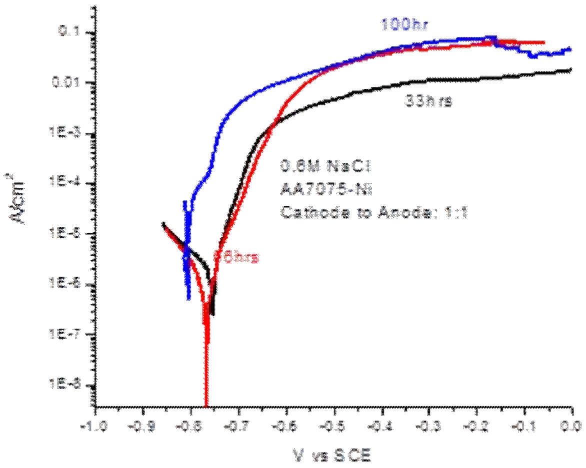

Figure 3. 46

Anodic Polarization of AA7075-T6 (with Ni, Cathode-to-Anode Area Ratio: 1:1 in 0.6M NaCl after 33hours/66hours/100hours

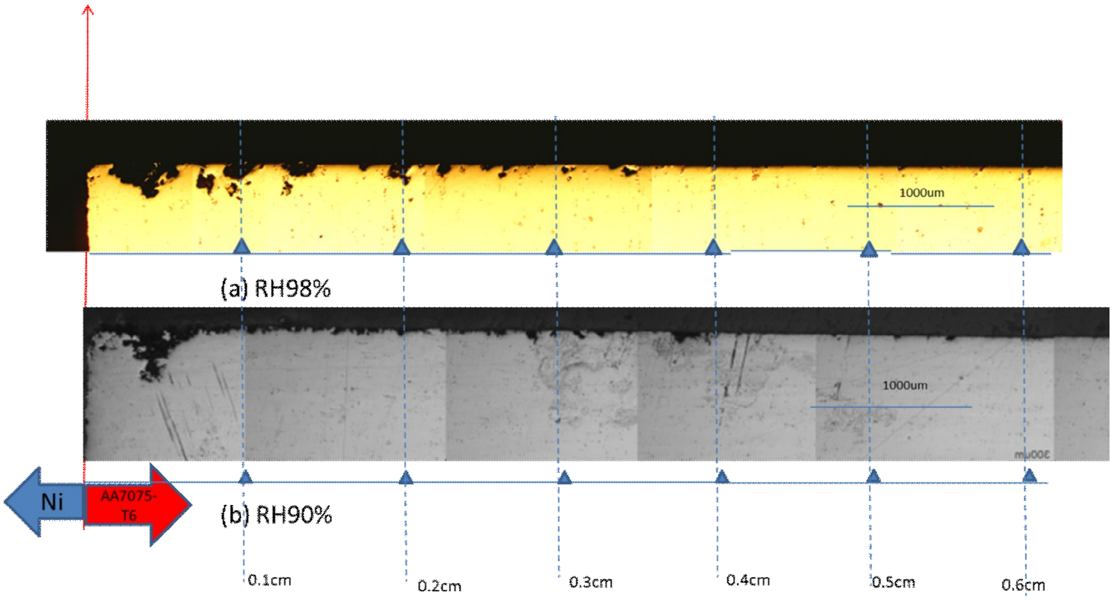

Figure 3. 47

The corrosion damage on the AA7075-T6, after 100hrs exposure, cathode-to-anode area ratio: 1:1, RH 98% and RH90%, 100µm water layer thickness

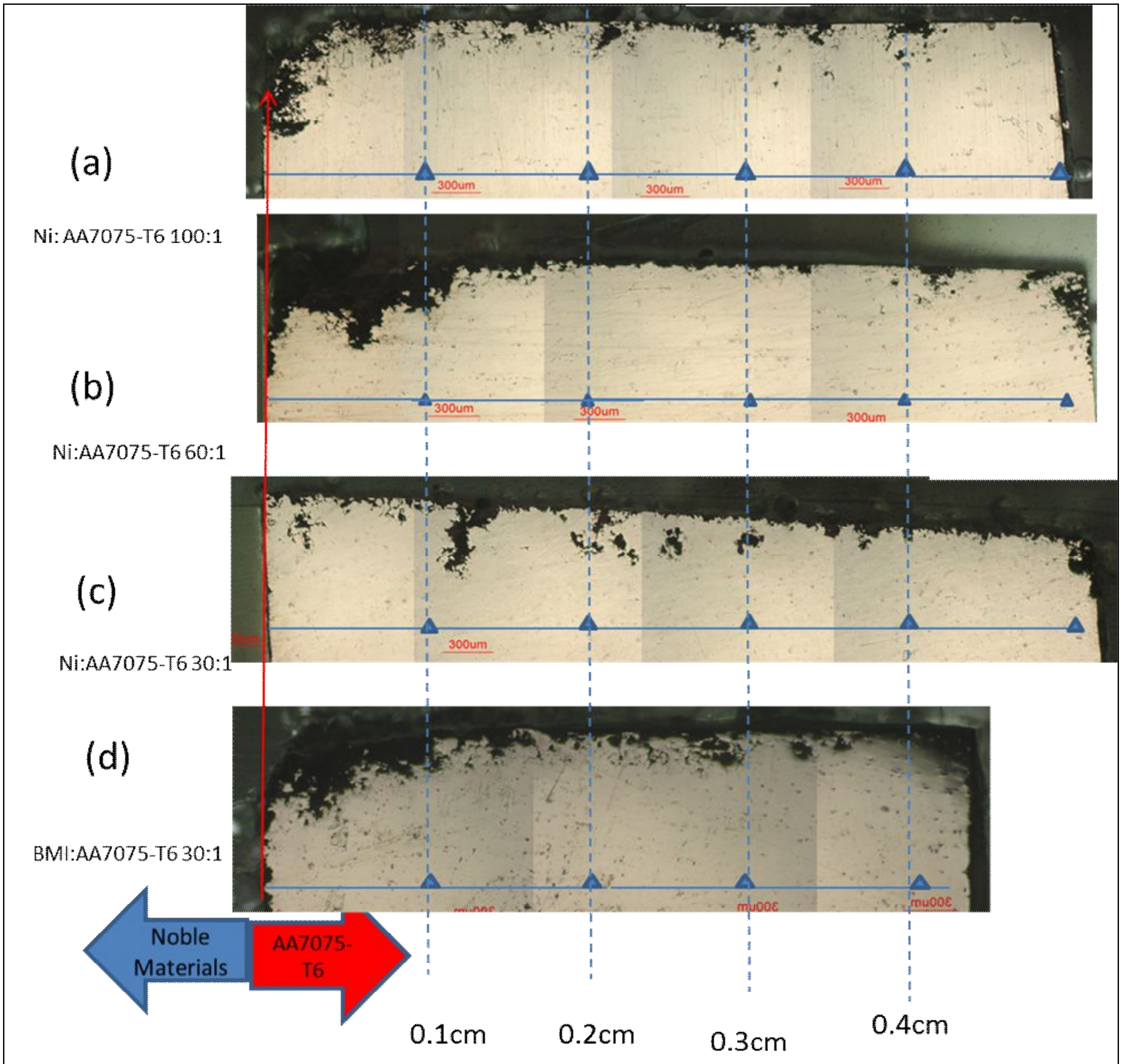

Figure 3. 48

The damage morphology and the quantitative measurement of damage depth on AA7075-T6 as a function of Cathode-to-Anode Area; The selection of Noble Materials (RH 98%), 100μm water layer thickness. a)Ni:AA7075-T6 100:1; b)Ni:AA7075-T6 60:1; c)Ni:AA7075-T6 30:1; d)BMI:AA7075-T6 30:1;

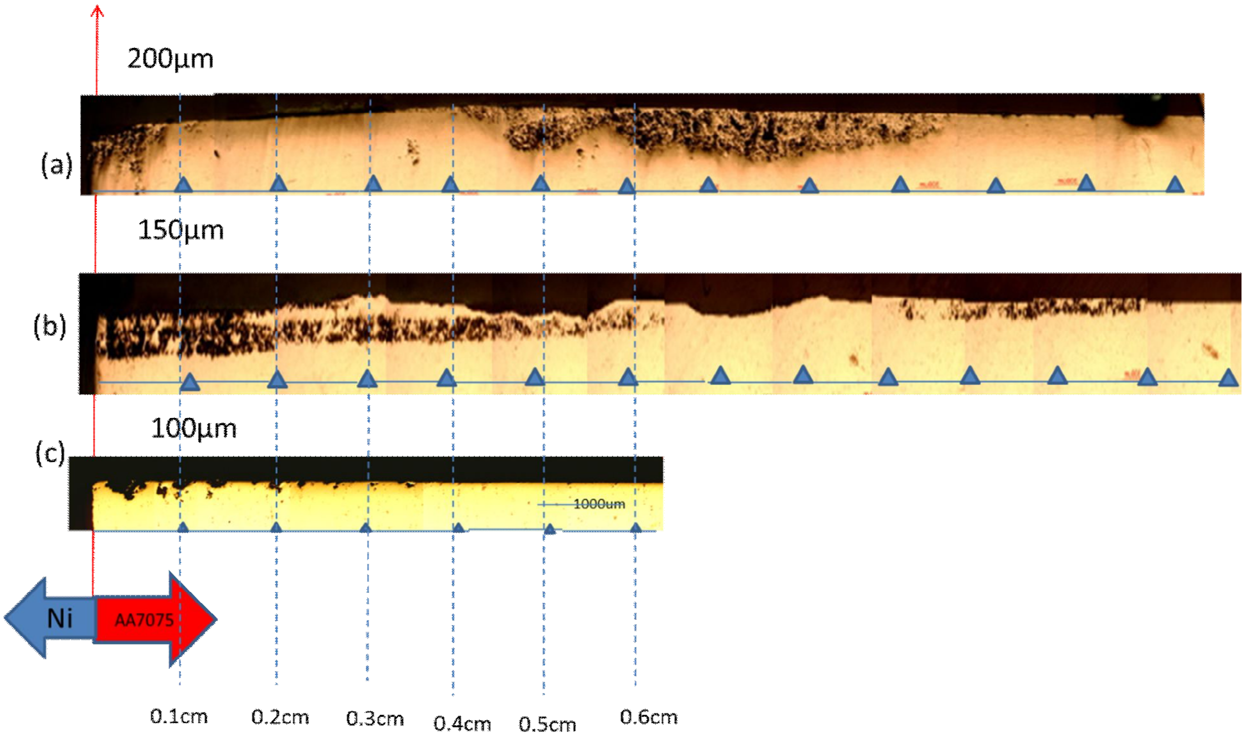

Figure 3. 49

Corrosion damage under different electrolyte thickness in AA7075-T6 with Ni 1:1, RH98%.

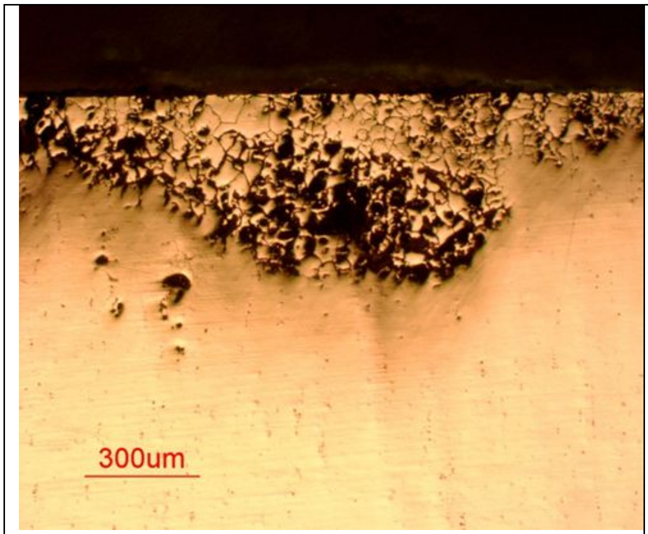 Figure 3. 50	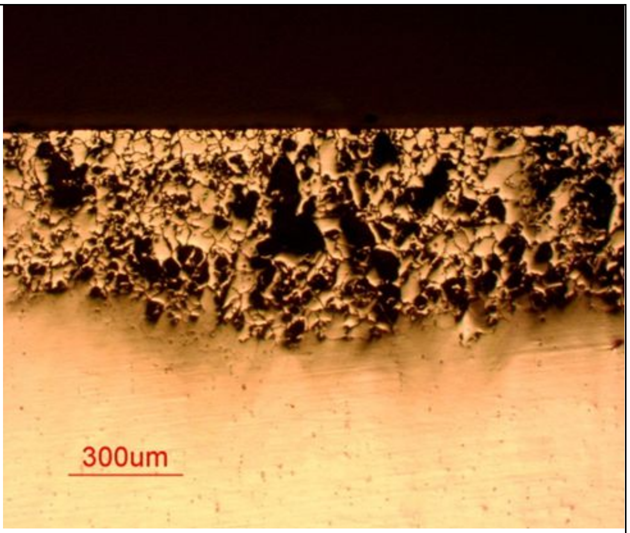 Figure 3. 51
Corrosion damage under 200um thickness in AA7075-T6 with Ni 1:1, RH98%, higher magnification.	Corrosion damage under 200um thickness in AA7075-T6 with Ni 1:1, RH98%, higher magnification.
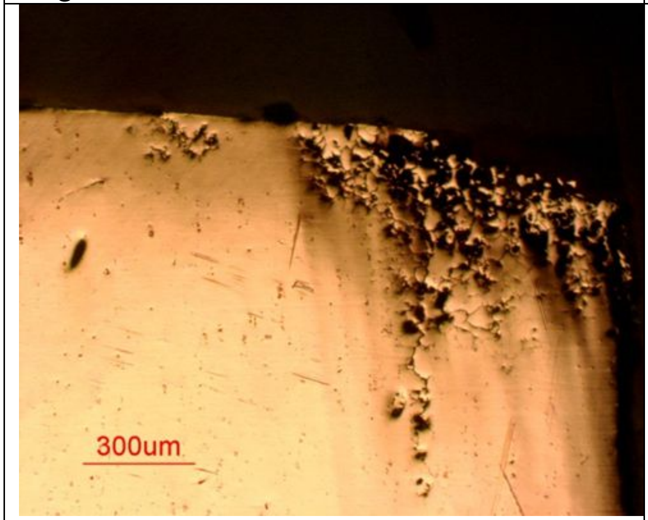 Figure 3. 52	
Corrosion damage under 200um thickness in AA7075-T6 with Ni 1:1, RH98%, higher magnification.	

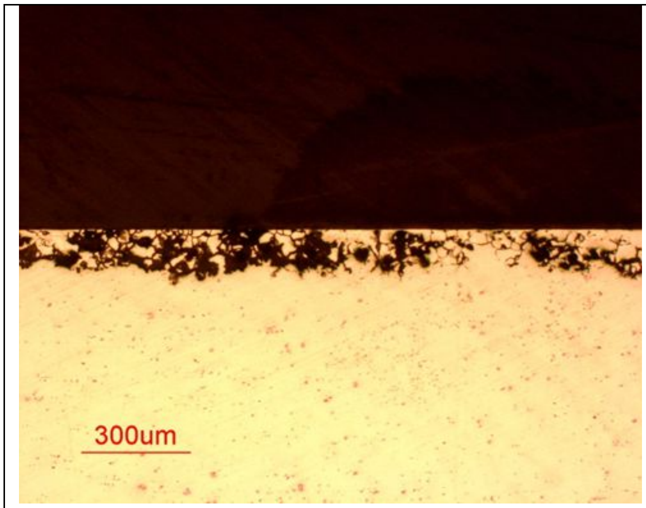 Figure 3. 53	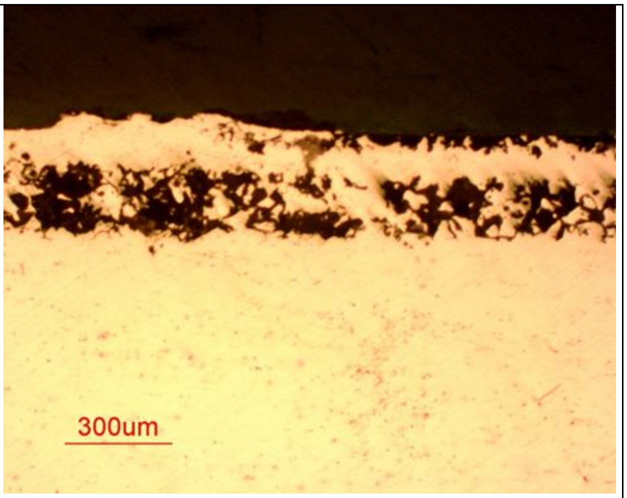 Figure 3. 54
Corrosion damage under 150um thickness in AA7075-T6 with Ni 1:1, RH98%, higher magnification.	Corrosion damage under 150um thickness in AA7075-T6 with Ni 1:1, RH98%, higher magnification.
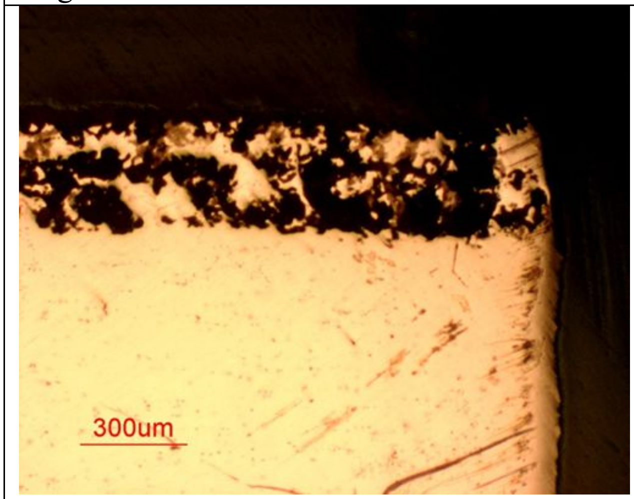 Figure 3. 55	
Corrosion damage under 150um thickness in AA7075-T6 with Ni 1:1, RH98%, higher magnification.	

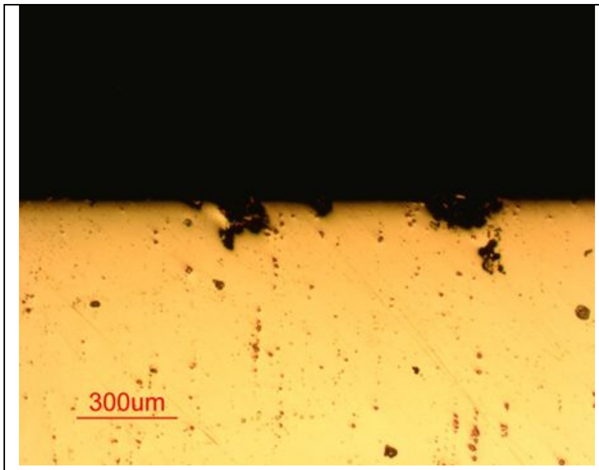 Figure 3. 56	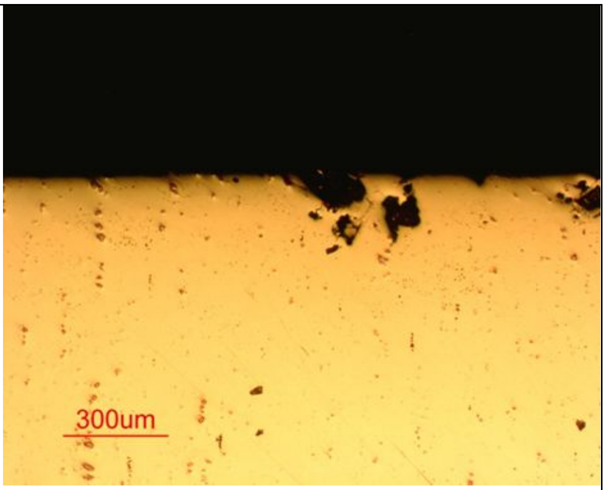 Figure 3. 57
Corrosion damage under 100um thickness in AA7075-T6 with Ni 1:1, RH98%, higher magnification.	Corrosion damage under 100um thickness in AA7075-T6 with Ni 1:1, RH98%, higher magnification.
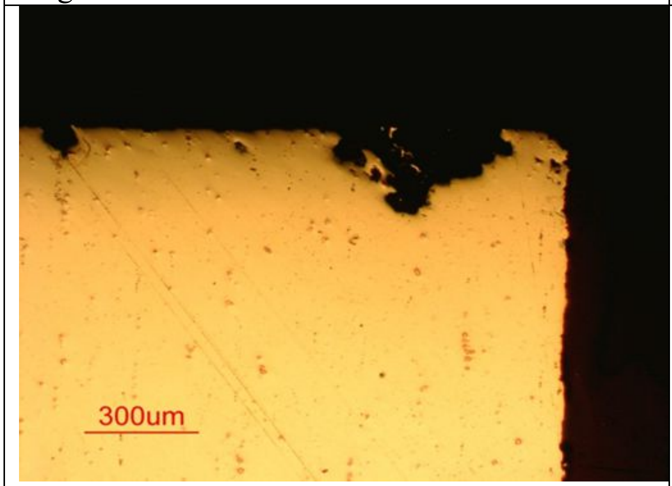 Figure 3. 58	
Corrosion damage under 100um thickness in AA7075-T6 with Ni 1:1, RH98%, higher magnification.	

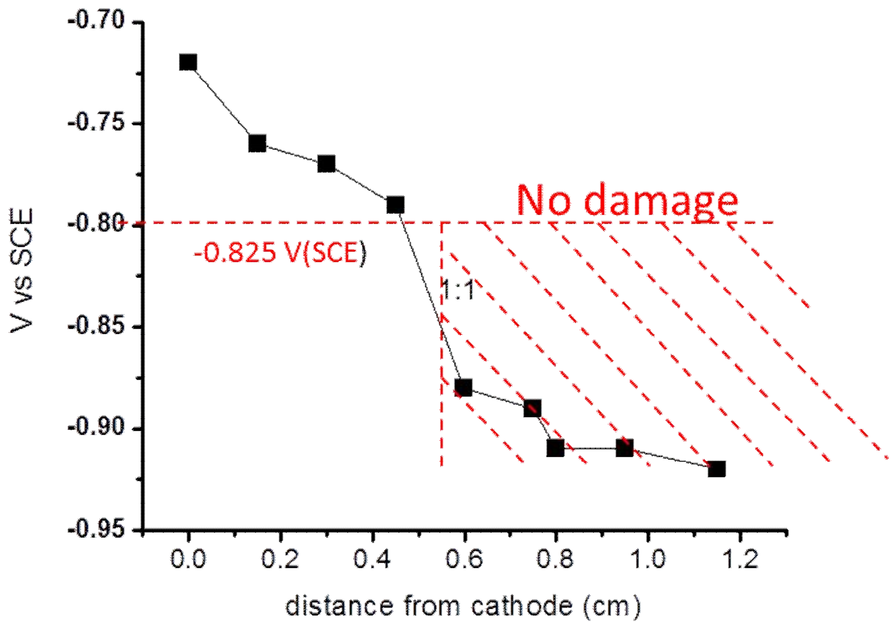

The potential distribution long AA075 after 100hrs exposure with Ni , measured by SKP

Figure 3. 59

The potential distribution along cathode/anode interface (AA7075-T6:Ni 1:1, RH98%, 100µm water layer thickness)

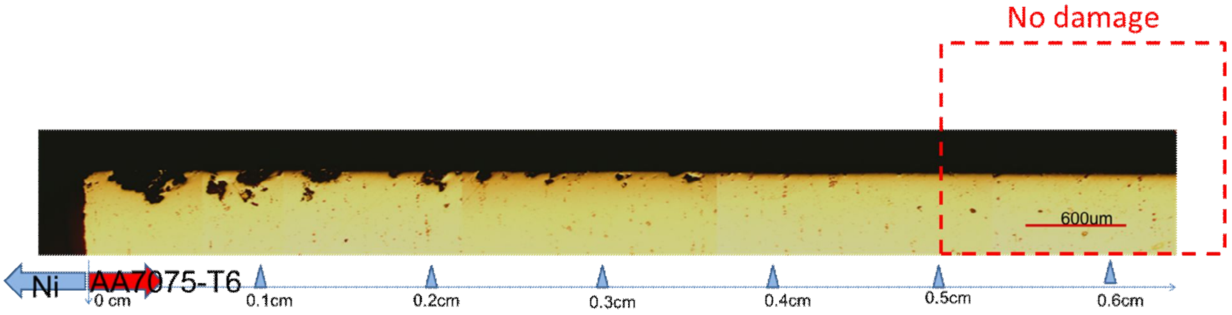

Figure 3. 60

Corrosion damage under 100um thickness in AA7075-T6 with Ni 1:1, RH98%.

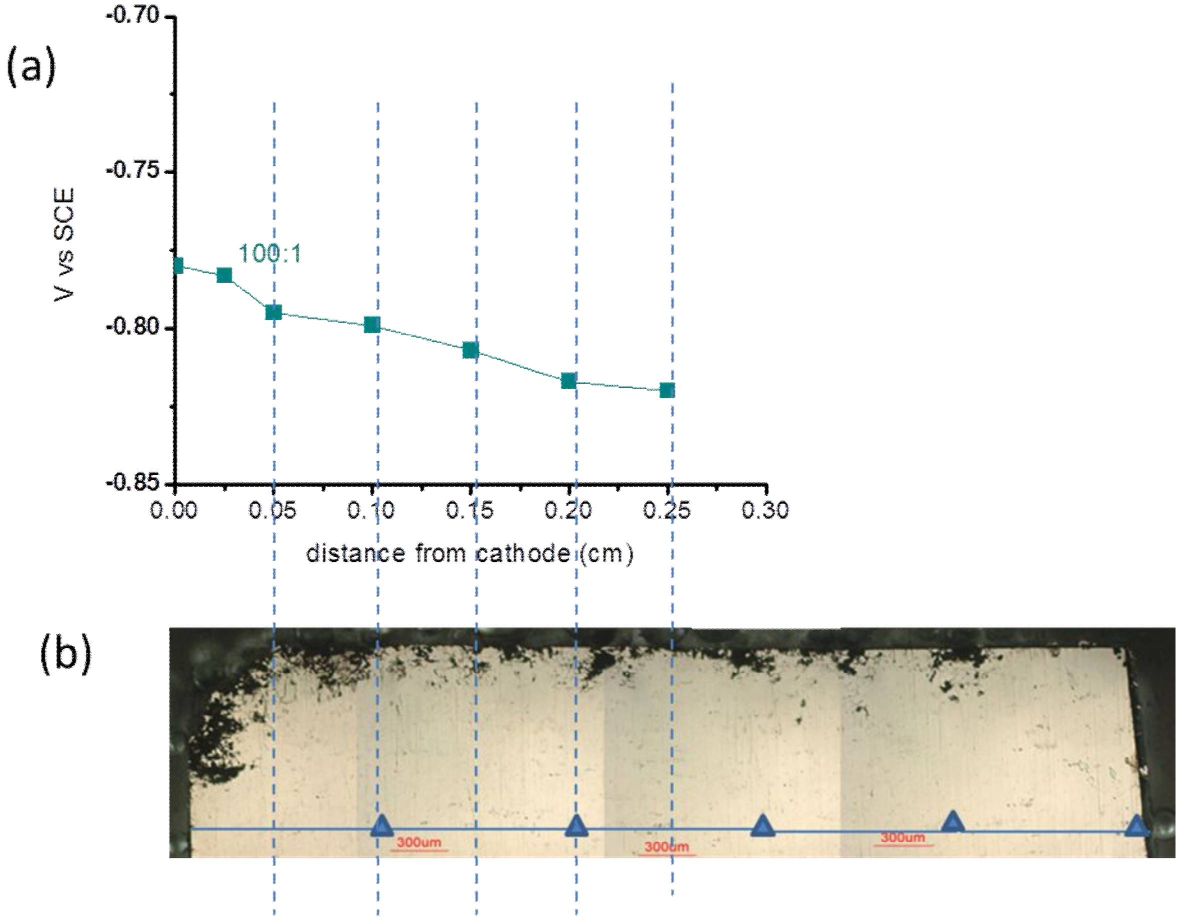

Figure 3. 61

The potential distribution along cathode-to-anode interface (AA7075-T6: Ni 100:1 , RH98%, 100μm water layer thickness)

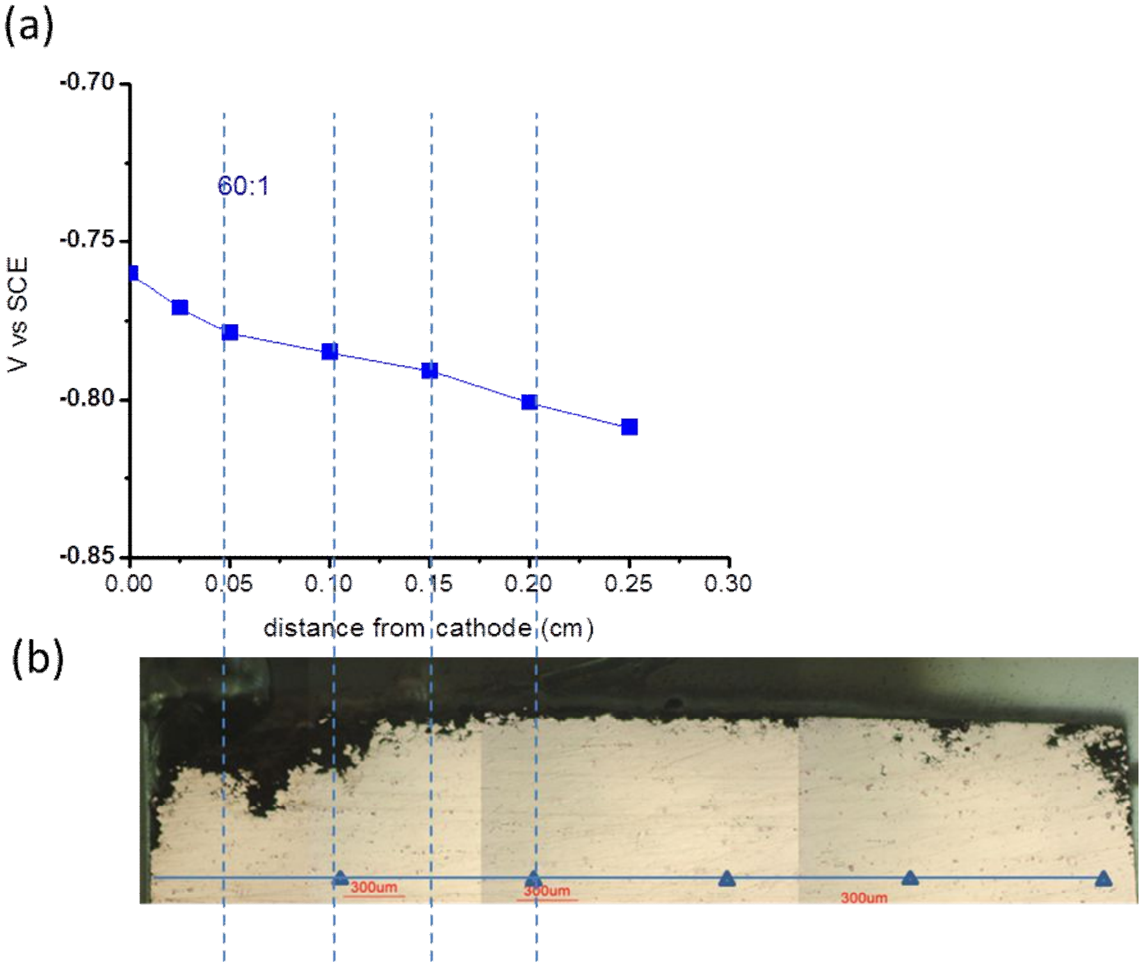

Figure 3. 62

The potential distribution along cathode-to-anode interface (AA7075-T6: Ni , 60:1, RH98%, 100µm water layer thickness)

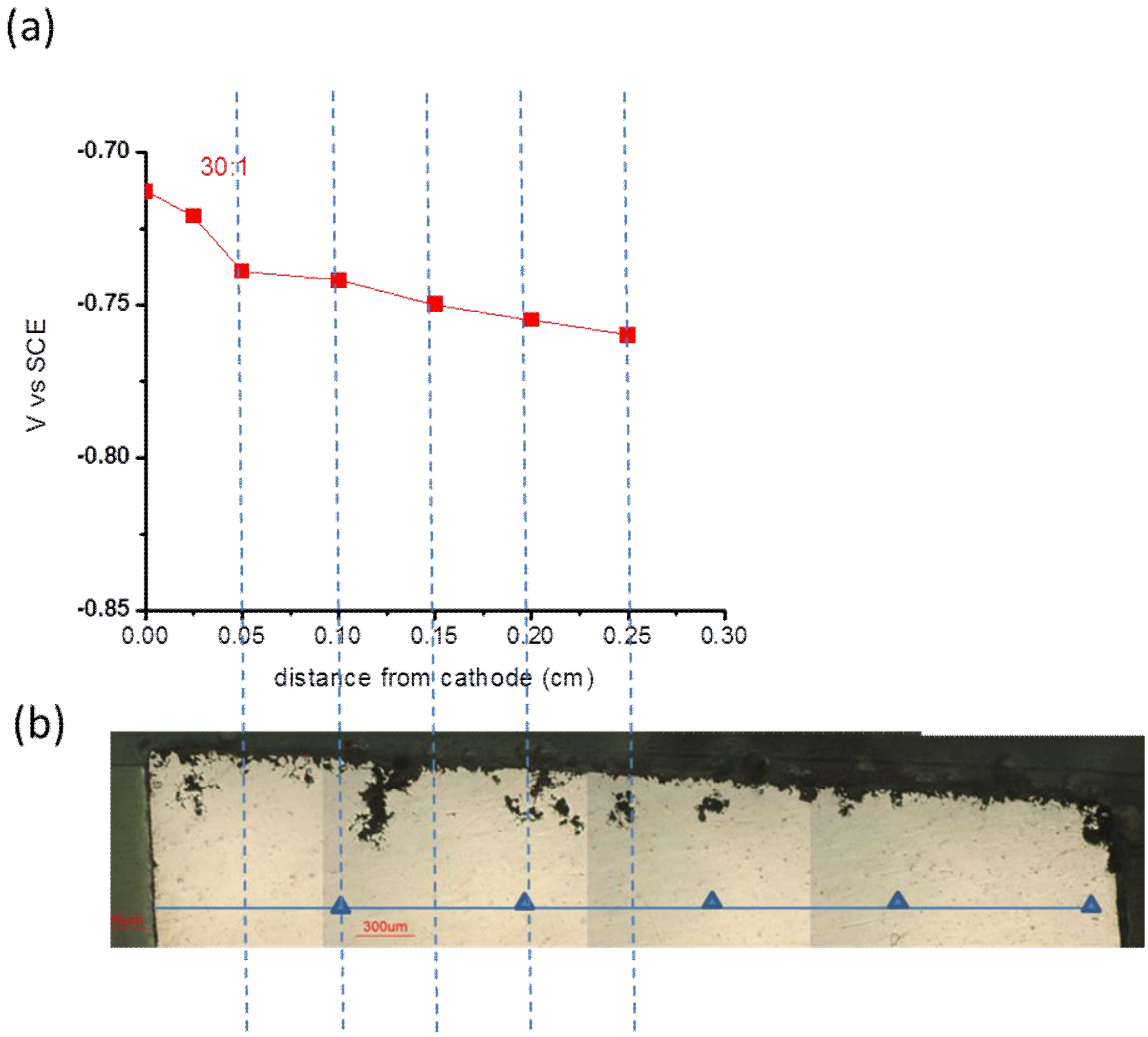

Figure 3. 63

The potential distribution along cathode-to-anode interface (AA7075-T6: Ni , 30:1, RH98%, 100µm water layer thickness)

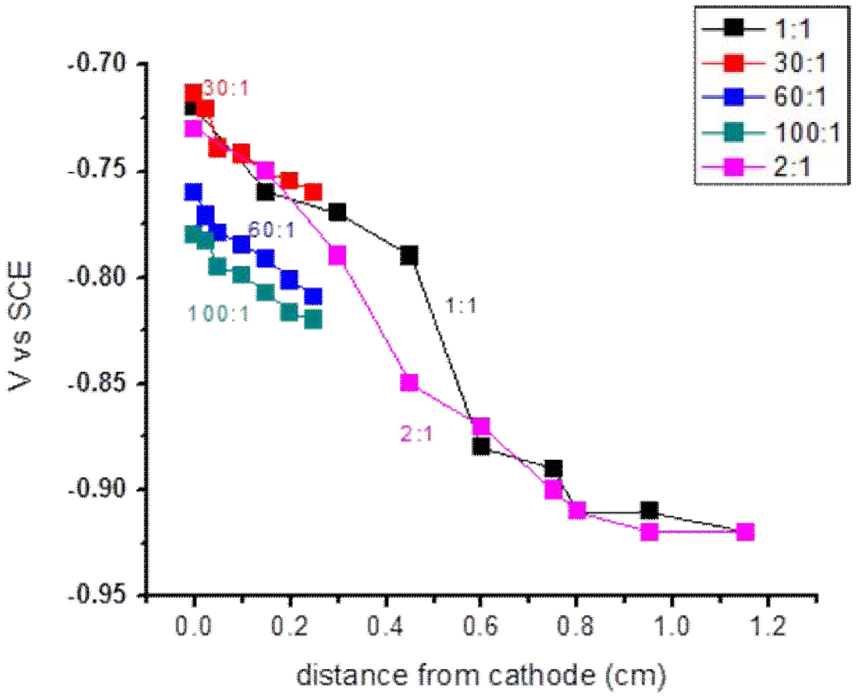

Figure 3. 64

Summary of potential distributions along cathode-to-anode interface (AA7075-T6:Ni, RH98%, 100μm water layer thickness)

<table>
<tr>
<td>
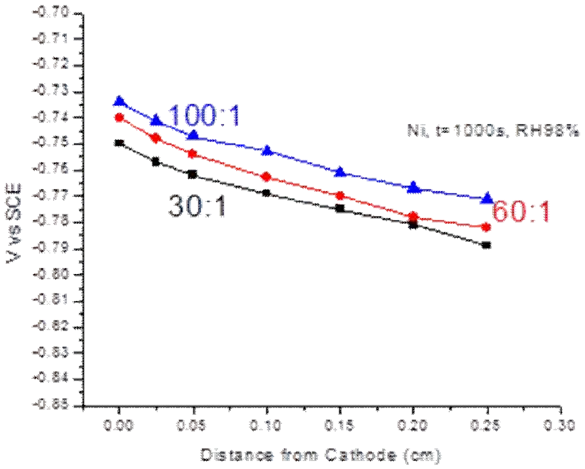

Figure 3. 65
</td>
<td>
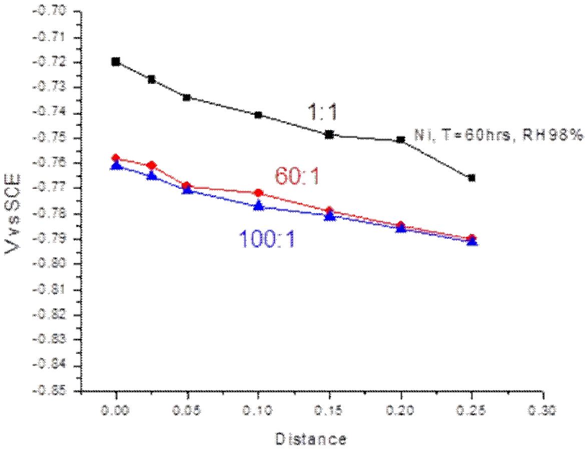

Figure 3. 66
</td>
</tr>
<tr>
<td>The potential distribution along cathode/anode interface after 1000s (AA7075-T6 with Ni, RH 98%)</td>
<td>The potential distribution along cathode/anode interface after 60hrs (AA7075-T6 with Ni, RH 98%)</td>
</tr>
<tr>
<td>
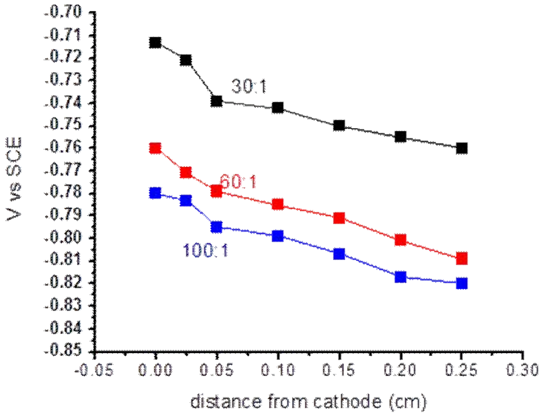

Figure 3. 67
</td>
<td></td>
</tr>
<tr>
<td>The potential distribution along cathode/anode interface after 100hrs (AA7075-T6 with Ni, RH 98%)</td>
<td></td>
</tr>
</table>

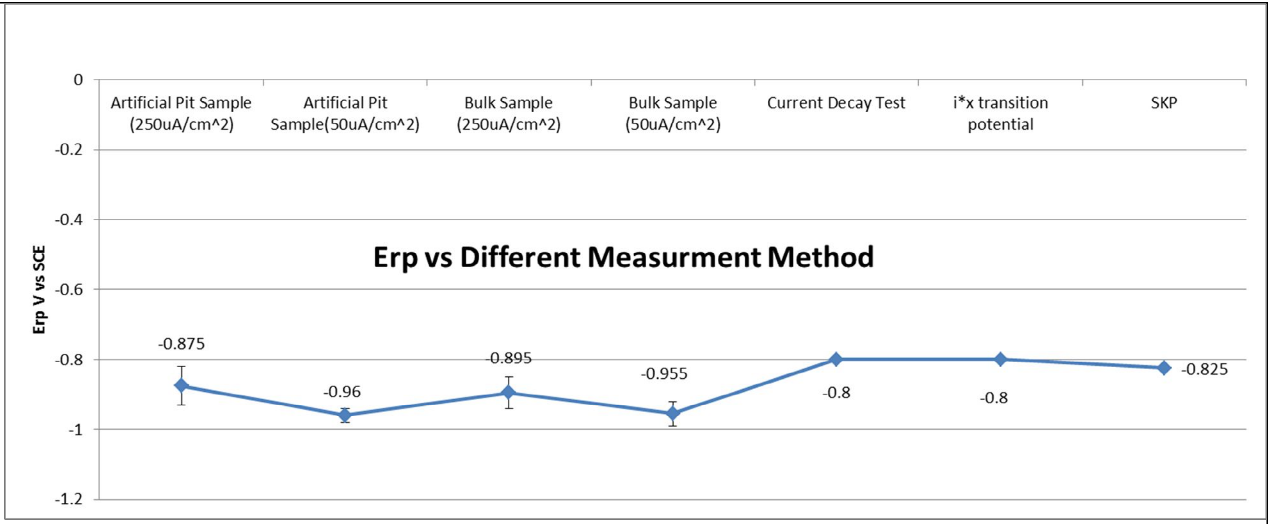

Figure 3. 68

Erp with Different Measurement Method

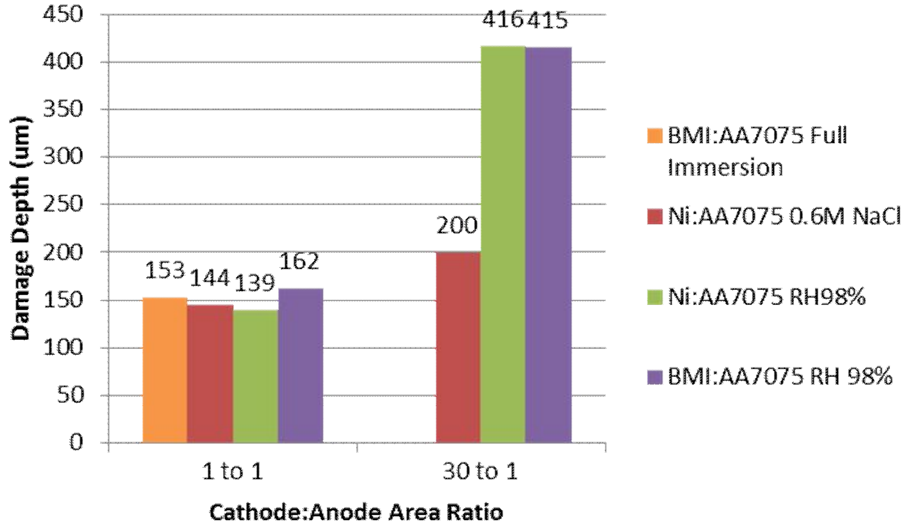

Figure 3. 69

The maximum observed corrosion damage for both BMI and Ni in both full immersion (0.6M NaCl) and RH98% condition.

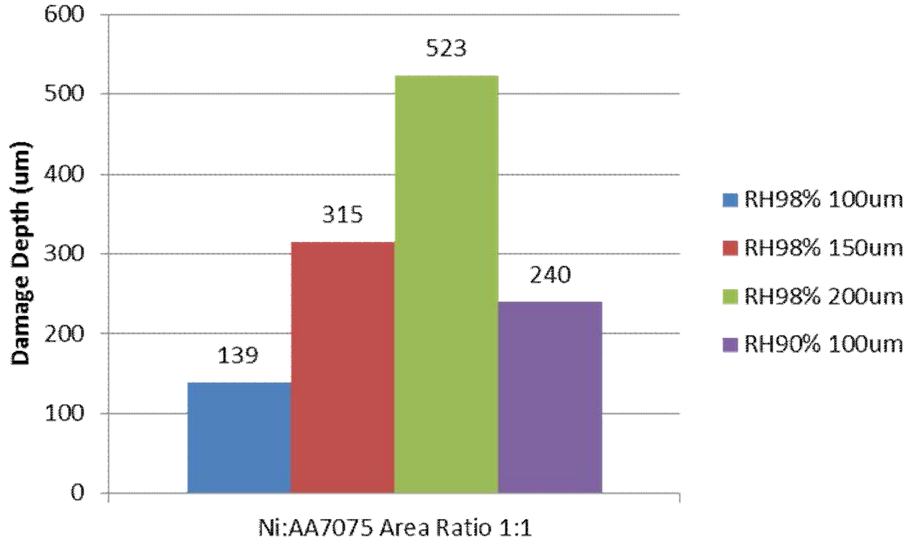

Figure 3. 70

The maximum observed corrosion damage for Ni with RH98% and RH90% with different electrolyte thickness.

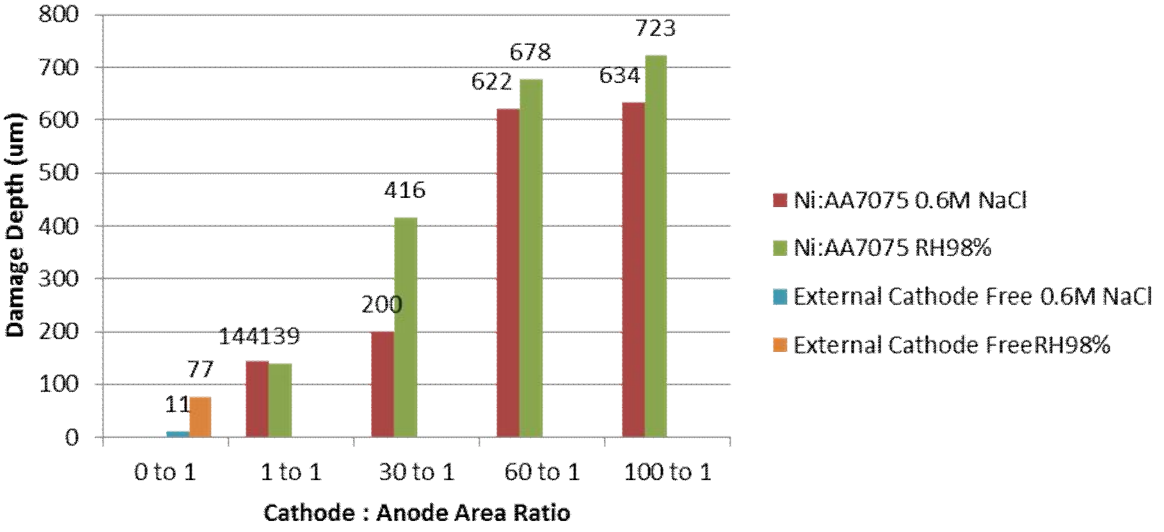

Figure 3. 71

The maximum observed corrosion damage for Ni with RH98% with different cathode-to-anode area ratio at 100um electrolyte thickness

Chapter 4 The Modelling Evaluation of Galvanic Corrosion System

In this section, the Finite Element Analysis (FEA) modeling of potential and current distributions for simulated fastener geometry is discussed. The configuration of the simulated fastener is designed to be consistent with the critical aspects of actual fasteners. Four conditions are investigated: 1) a time-dependent model of the propagation stage assuming the corroding anode is in contact with an acidic solution (0.5M $AlCl_3$) ; 2) a stationary model using the boundary conditions extracted from experiments on materials exposed for 100hrs exposure in 0.6M NaCl; 3) condition 2) with addition of inhibitors as a modified boundary condition; 4) a stationary model using the boundary conditions extracted from experiments on artificial pit samples in 80% and 100% saturated $AlCl_3$

A simple planar configuration with thin electrolyte layer to simulate atmospheric condition with 98% RH and 90% RH was also studied. The effects of environmental factors, including the nature of cathode, the [Cl^-] concentration, and the cathode-to-anode area ratio were studied through the COMSOL 5.0a multiple-physics software. The results were compared with E_{rp} from the previous chapters to assess the corrosion stability of the whole fastener system.

4.1. General Introduction

4.1.1. Background: The modelling of galvanic corrosion and the limitation of the FEM modelling

The research in this chapter is focused on using modelling tools to address the conditions by which galvanic interactions can stabilize localized corrosion in light of the given stability criteria.

By introducing stability criteria into the models, the conditions and the combination of the controlling parameters that meet the criteria can be determined with the aid of FEM software. This approach has been recently used by some researchers. Proust *et al*[1] proposed pH_r as a criterion for arresting the propagation of crevice corrosion in their analytical model using COMSOL software, assuming that repassviation occurred locally when the pH was higher than a critical value, pH_r. Mizuno[2] predicted the IGC damage distributions of the AA5083-Steel galvanic system under atmospheric conditions over a range of exposure scenarios using numerical models with experimental-derived boundary conditions. In these cases, the condition under which localized corrosion is stabilized was studied as a function of exposure conditions. Although all of the above contributed to the development of new ideas and tools, very limited work has been focused on the atmospheric condition with galvanic interactions. In addition, the sensitivity of the corrosion system to the boundary conditions was not systematically studied.

4.1.2. Inhibitors for noble materials as a mitigation strategy

The choice of boundary condition can strongly affect the output results of modeling [3–5]. In the present study, inhibitor effects on the noble metals will be first experimentally tested and then used as a modified cathode boundary condition to study its effect on the stability of the localized corrosion

The effect of inhibitors on the rate of the oxygen reduction reaction has been studied by many researchers [6–12]. The oxygen reduction rate was found to be remarkably reduced on many metals by introducing the inhibitors into the bulk solution [9,11–13]. This modification of the cathodic kinetics can be potentially used as a boundary condition input for the purpose of modeling study.

The impact of chromate, cerium, molybdate and vanadate ions on the oxygen reduction kinetics on Cu, Al and steel have been studied [6,12,13]. However, very little research on inhibitor effects has been conducted on noble materials, particularly those of interest in the present study. In the present study, $NaVO_3$ was selected as the inhibitor of interest. Its effects on the cathodic kinetics were measured through the potentiodynamic scanning on the cathode materials (Ni, Ag, and BMI). The results were then applied as new boundary conditions. The response of the modeling to the new boundaries was investigated. These studies allow a determination of the likelihood that the inclusion of these inhibitors in noble metal-containing coatings will be an effective mitigation strategy for galvanically induced localized atmospheric corrosion.

4.1.3. The engineering question to be answered in this chapter

The questions to be answered in this chapter are focused on how the modelling can facilitate the evaluation of the stability of localized corrosion in the AA7075-noble material galvanic system given a range of environment parameters. The present study attempts to identify the conditions under which this galvanically induced localized corrosion susceptibility can be minimized. To achieve this objective, FEM modeling is used to:

1) Predict the effect of the external parameters on the stability of galvanic corrosion with a given stability criteria. The factors of interest include the system geometry, nature of noble material, the solution concentration and water layer thickness;
2) Examine the sensitivity of the coupled system to the inhibitor-modified boundary conditions.

Given a proper stability criterion, modeling allows the evaluation of the influence of environmental factors on localized corrosion stability, and ultimately to seek the optimal mitigation strategy to ensure the long-term reliability of engineering structures.

4.1.4. General approach used

In general, the modelling work in this chapter is primarily via FEM analysis using COMSOL multi-physics software. The software allows flexibility with respect to inputs of geometry, solutions, and boundary condition and then solves the partial differential equation with the given governing equation and boundary conditions.

The boundary condition is derived from the experiments. In the present study, the boundary conditions are the polarization curves of cathodic and anodic kinetics. The software allows the input of i(E) directly from the experiment data. No numerical equation (although given in the following sections) to fit the boundary condition is therefore necessary.

4.1.5. Brief summary of the results

The work in this chapter first found the limitation of COMSOL for a time-dependent calculation as its failure of consideration of ionic interaction into the calculation. Consequently, a stationary model for steady state with boundary condition after 100hrous exposure was used to study the galvanic interactions without ignoring the significance of the electrochemical kinetics change over the time.

Using the stationary model, , the effects of environmental factors, including the nature of cathode, the [Cl^-] concentration, and the electrolyte layer thickness on the potential distribution along the noble materials-AA7075 interface were calculated . The effects of design factors, such as the fastener gap width, the cathode-to-anode area ratio, and the percentage of noble materials in the coating (to simulate what is known as pigment volume concentration, PVC) were also calculated. The potential distribution along the anode site was compared with E_{rp} from the previous measurements to predict the stability of the galvanic corrosion for the system.

An inhibitor-modified boundary condition was also introduced. Its effect on electrochemical potential distribution was quantified. It was found the potential can decrease to a level close to E_{rp} with the addition of inhibitors with a narrow fastener gap (20μm), which is potentially promising to be used as a mitigation strategy.

A simple planar geometry was also studied under atmospheric conditions. The calculated distribution of potential along noble materials-AA7075 interface was compared with previous SKP measurements from the samples with the same conditions. A discussion to rationalize the discrepancy between the calculated and modelling data was made.

4.2. Modelling Set Up and Experimentally-derived Boundary Condition

Section 4.2 introduces the modeling set up. The details of the modeling set up, including the governing equations, subdomain conditions and the geometry of interest are included.

4.2.1. Governing Equation of modeling, subdomain condition and geometry

FEM software (COMSOL Ver. 5.0a) was used for the present modeling study. The Nernst–Planck equation, assuming no convection and steady-state conditions, was used to describe the transport and mass balance of each species:

Equation 4.1

$$\nabla \bullet (-z_i u_i F c_i \nabla \phi - D_i \nabla c_i) = R_i$$

where D_i = diffusion coefficient of species *i*, c_i = concetration of species *i*, z_i = charge of species *i*, u_i = mobility of species *i*, R_i = reaction rate of species *i* ; F = Faraday's constant; Φ = the potential of the solution. To simplify the modelling, no chemical reactions in the bulk solution were assumed to occur in this study. The species and the related parameters in the solution of the model are listed in Table 4.1.

Figure 4. 1 shows the geometry of the modeled system, an approximation of a fastened joint exposed to atmospheric conditions. The distance, d, represents the length (cm) along noble materials-AA7075 interface. d=0cm is the position at the beginning of the fastener gap, d=1.2cm is the position at the bottom of the fastener gap. The variable f represents the length (cm) of external cathode. The origin for f (i.e., f=0cm) is at the left side of the external cathode and f=5.8cm ends at the right side of external cathode. WL represents the electrolyte layer thickness which ranged from 0.5cm (for full immersion condition), to 25µm (for atmospheric condition). The width of fastener gap, w, ranged from 0.3cm to 10µm.

4.2.2. Boundary Condition Set Up

Three electrochemical boundary conditions (referred to as Boundary Conditions 1, 2, and 3) were derived from the experimental data as shown in Figure 4. 1. Boundary Condition 1 and 2 are for the cathode materials. The cathodic polarization curve i(E) from the experimental measurements is used and can be replaced by the cathodic polarization curves from different cathode materials. Boundary Condition 3 is for anode. The anodic polarization curve i(E) from the experimental measurements is used.

4.2.2.1. Materials

The materials tested were the same as those tested in Chapters 2 and 3. Ni, BMI and pure Ag (99.97%) were used for cathodic kinetics measurement in this chapter. AA7075 rolled sheets were used for anodic kinetics measurement. The cleaning procedures remained the same as in the previous chapters.

4.2.2.2. Solution

NaCl solutions were used as the simulants for the cathodic kinetics measurement. The selected concentrations of chloride ([Cl^-]) were 0.01 M, 0.1 M and 1 M. The selected pH values were 6, 9 and 11, achieved by the addition of NaOH. These solutions were selected to simulate the local alkalinity that develops at cathode site where hydroxide is generated from the oxygen reduction reaction. $AlCl_3$ solutions were used as the simulants for the anodic kinetics measurement. This process simulated the local acidic chemistry that develops at the along anode surface due to the hydrolysis of dissolved aluminum ions. The concentrations ranged from 0.01M to 0.5M.

To simulate the time-dependent anodic kinetics, 0.1M and 0.6M NaCl was used. The samples were immersed in the solution for 100hrs before potentiodynamic scanning.

De-ionized water was used for solution preparation. All the solutions were prepared and used at room temperature and were quiescent.

4.2.2.3. Apparatus

Flat cells were used in this test with the same configuration as in section 2.3.1. A Gamry Potentiostat PCI-4 was also used for electrochemical signal controlling and processing.

4.2.2.4. Procedure

4.2.2.4.1. Cathodic Kinetics from Experiments

Cathodic polarization curves of Ni, Ag, and BMI were measured in a flat cell with NaCl solutions of different chloride concentration and pH from 0.1 V above to 1 V below the OCP with a scan rate of 0.5 mV/s. The selected concentrations of chloride ([Cl^-]) were 0.01 M, 0.1 M and 1 M. The selected pH values were 6, 9 and 11.

4.2.2.4.2 Anodic Kinetics from Experiments

Two sets of anodic polarization were measured. The anodic polarization in $AlCl_3$ is for modelling condition 1 as mentioned in the beginning of the chapter. The anodic polarization in 0.6M/2.8M NaCl after 100hrs of exposure is for modelling condition 2 and 3.

The anodic polarization behavior was determined for AA7075-T6 under conditions meant to simulate those present during the propagation of localized corrosion. Propagation of localized corrosion was simulated by using acidic $AlCl_3$ solution with concentrations ranging from 0.01M to 0.5M. Bulk sample of AA7075 immersed in a flat cell was used for this test. All the scans ranged from 0.1 V below OCP to 0 V (SCE) with a scan rate of 0.5 mV/s.

To simulate the time-dependent anodic kinetics, 0.1M and 0.6M NaCl was used. The samples of AA7075-T6 were immersed in the solution for 100hrs before potentiodynamic scanning. The details of tests was described in section 3.2, Chapter 3.

4.2.2.4.3. Cathodic kinetics measurement with addition of inhibitor

$NaVO_3$ was selected as the inhibitor for the cathodic kinetics study. Two levels of concentration (0.01M and 0.05M) were added to 0.1M NaCl for the cathodic polarization test. Cathode materials, Ni, Ag and BMI were immersed in a flat cell with $NaVO_3$ in addition to 0.1M NaCl. The cathodic polarization started at 0.1 V above OCP to -1V (vs SCE) with a scan rate of 0.5 mV/s.

4.3. Galvanic Corrosion Modeling with Fastener engineering geometry

4.3.1. Condition 1: A propagation stage with cathode in the 0.1M NaCl and anode (AA7075-T6) in 0.5M $AlCl_3$: Time-dependent Model.

4.3.1.1. The cathodic polarization for Ni, BMI and Ag in NaCl

The cathodic polarization for the noble materials aims to quantify the effect of experimental conditions, such as the nature of cathode materials, [Cl^-] and pH on the oxygen reduction reaction. The numerical equations that fit the polarization curves will be used as the input of boundary condition for the modelling study.

Figure 4. 2 and Figure 4. 3 show the cathodic polarization behavior of Ni as a function of [Cl^-] and pH. The figures show that the OCP did not systematically vary with either pH or [Cl-]. The rate of oxygen reduction also does not change much in potential region of interest (-1 to -0.4 V (SCE)) with different [Cl^-] and pH. This insensitivity is due to the fact that reaction is diffusion limited. For BMI, the oxygen reduction rate of BMI was not significantly affected by [Cl^-] nor pH as shown in Figure 4. 4 and Figure 4. 5, although the OCP does seem to decrease with increasing NaCl concentration and elevated pH.

Figure 4. 6 and Figure 4. 7 show the cathodic polarization behavior of silver. The OCP found corresponded well to the reversible potential for $Ag+Cl^- \rightarrow AgCl+ e^-$. Because the curves were initiated at a potential above the OCP (i.e., above the reversible potential), AgCl was formed initially which was then reduced upon cathodic polarization, resulting in the wave just below the OCP. The oxygen reduction rate for all the three cathode materials did not vary with different [Cl^-] as shown in Figure 4. 10

4.3.1.2. The anodic polarization for AA7075 in acidic solution

Similar as in section 4.3.1.2, the effect of the concentration of $AlCl_3$ on the anodic kinetics was studied in this section. The acidic solution was to simulate the propagation stage of anode corrosion, where the hydrolysis reaction is dominant. The different level of $AlCl_3$ is to simulate the different stage of propagation. For example, the 0.01M $AlCl_3$ represents the initial stage of hydrolysis under the propagation. With the proceeding of hydrolysis process, more Al^{3+} dissolves and react with the solution to form more concentrated $AlCl_3$, which can be represented by the anodic kinetics attained from 0.05 M to 0.5M $AlCl_3$. Although the anodic slopes are similar, the higher concentration of $AlCl_3$ results in a lower OCP as shown in the figure. The results will be used as the anodic boundary condition in the following section.

No passivation behavior was observed for AA7075 in solutions simulating the chemistry of a localized corrosion site, as expected and seen in the polarization curves in Figure 4. 8. Acidic solution causes the rapid dissolution of Al alloy. Both the pH and OCP values decreased with increasing $AlCl_3$ concentration.

A numerical equation was used to fit the polarizations curve for the anode site. For Boundary Condition 3, the anodic kinetics of the AA7075-T6 simulating the Al dissolution in acidic $AlCl_3$ was described by:

$$i^{p}{}_{a} = i^{p}{}_{acorr}[\exp(\frac{E^{p}a_{corr} - V}{\alpha^{p}{}_{a}}) - \exp(\frac{E^{p}a_{corr} - V}{\beta^{p}{}_{a}})] \qquad \text{Equation 4.2}$$

where $i^{p}a_{corr}$ is anode corrosion current density, $E^{p}a_{corr}$ is anode corrosion potential, $\alpha^{p}{}_{a}$ is the anodic coefficient for the anode, and $\beta^{p}{}_{a}$ is the cathodic coefficient for the anode

A plot of the OCP value of AA7075 as a function of $AlCl_3$, is shown in Figure 4. 9, produced a linear function, E_{corr} =-0.60433-0.07154*log[$AlCl_3$], where E_{corr} is the OCP of AA7075 in $AlCl_3$.

4.3.1.3. The current density/potential vs time in the time-dependent model.

For Boundary Condition 1, a time-dependent model was studied in order to more precisely describe the local chemistry and the corrosion behaviors as a function of time. An example, Ag-AA7075 coupled system is selected At time=0, it was assumed that cathode was in contact with

0.1M NaCl and anode was in contact with 0.5M $AlCl_3$. The surface reaction $Al \rightarrow Al^{3+} + 3e^-$ was added as an additional anode boundary condition. [Al^{3+}] will be generated along anode surface and diffuse into subdomain solution. The $E^p a_{corr}$ for anode is set as a function of the [Al^{3+}]. This model reflects the change of ionic concentration and thus of potential with the time. The detailed boundary conditions are shown in Table 4.2.

Figure 4. 11 shows the distributions of [Al^{3+}] and [Na^+] along the cathode-anode coupling surface after 12,000s. It should be pointed out that the negative value of the calculated [Na^+] is obviously not physically realizable. The problem arises because the COMSOL software only describes an electrochemical system with the Nernst-Planck equation coupled with the electroneutrality condition. This approach ignores the electric field caused by ionic interactions. Improved means of handling these ionic interactions is required, but such improvements are outside the scope of this thesis. Thus, the present research will be focused on the steady-state models.

4.3.2. Condition 2: A propagation stage with cathode in the 0.6M NaCl and anode (AA7075-T6) in 0.6M NaCl after 100hrs exposure : Steady State

As shown in section 4.3.1, the limitation of time-dependent model with COMSOL causes barriers to study the effect of time evolution on the corrosion stability of the fastener system. A boundary condition drawn from data on materials tested after 100hrs of exposure was therefore introduced into the model to attempt to predict the corrosion evolution over time.

4.3.2.1. Boundary Condition and Subdomain Setting.

The fastener geometry in this study is the same as in the previous sections as shown in Figure 4. 1. For Boundary Condition 1 and 2 of the cathode, the polarization curves of noble materials (Ni, BMI, and Ag) in 0.1M NaCl solution were used to simulate the cathodic kinetics in the bulk solution, as the cathode part of the curves (i.e. the diffusion limited current density) was not affected by the [Cl^-] concentration as discussed in section 4.3.1.1. For Boundary Condition 3 of the anode, the polarization curves of AA7075-T6 in 0.6M NaCl after 100hours of exposures were used. 0.6M NaCl is a solution of interest because it is an equivalent concentration for 98%RH as well as the concentration of sea water, which is consistent with the environment for the potential application. The 100hour of time period is selected to be consistent with the previous galvanic coupling experiments in chapter 3.

The polarization curves were imported as data sets and used as boundary conditions via the interpolation function of COMSOL. Therefore, no numerical equation fitting was required.

The initial subdomain setting for the entire volume assumed 0.6M NaCl with the consideration of two species only (Na+ and Cl^-). The parameters for diffusion and migration are listed in Table 4.1.

4.3.2.2. Potential Distribution as a function of Cathode Materials (Ni, Ag and BMI)

Figure 4. 12, Figure 4. 13, and Figure 4. 14 show the potential distribution inside the fastener as a function of the length along cathode-to-anode interfaces, i.e. distance d.(the distance d part indicated in Figure 4. 1) when AA7075-T6 is coupled with Ni, Ag and BMI respectively.

Figure 4. 12 shows the potential distribution when coupled with Ni. The width of fastener gap (w) ranged from 10μm to 0.3cm. As shown in the figure, the highest potential appears at the mouth of the fastener (d=0cm) and then decreases to the lowest at the bottom of the fastener (d=1.2cm). The slope of the potential distribution curves is dependent on the gap width. With the narrowest gap (w=10μm), the slope is the steepest, i.e. the degree of potential change with the same distance d along cathode-to-anode coupling interface (mV/cm) is the largest, ranging from -0.654V to-0.758V vs SCE with a degree of change 86mV/cm. When the gap is wider, for example when w=0.3cm, the slope is the flattest, with the potential ranging from -0.744V to -0.751V vs SCE with a degree of potential change of 6mV/cm. For the different selections of cathode material, the trend of potential change over cathode-to-anode interface is similar. For Ag (Figure 4. 13), with a gap width of 10μm, the potential ranges from -0.656V (d=0cm) to -0.759V vs SCE (d=1.2cm). With a gap width of 0.3cm, the potential ranges from -0.738V (d=0cm) to -0.748V vs SCE (d=1.2cm). For BMI (Figure 4. 14), the potential ranges from -0.636 V (d=0cm) to -0.752V vs SCE (d=1.2cm) for gap width 10μm and -0.738V (d=0cm) to -0.748V vs SCE (d=1.2cm) for gap width 0.3cm, respectively. More details of the effects of noble material selection are included in the discussion section.

For all the three selected cathode materials, the entire potential distribution for all the gap width is higher than the E_{rp} (-0.82V vs SCE) from the measurements in the previous chapters. This indicates the galvanic system is under active corrosion no matter which noble material is selected and for the entire range of gaps.

Accordingly, Figure 4. 15 to Figure 4. **17** show the current density distributions with the fastener gap for Ni-AA7075-T6, Ag-AA7075-T6 and BMI-AA7075-T6 galvanic system. The current density, as a function of potential, i(E) is calculated by using the cathodic polarization curves measured in 4.3.1.1. In Figure 4. 15, for the Ni-AA7075-T6 system, the current density remains negative along the cathode site and becomes positive at the anode site. The cathodic current density is lower in magnitude (~-0.2A/cm^2) than the anodic current density (ranged from 5.5A/cm^2 to 2A/cm^2, depending on the position and the gap width). This trend is consistent for Ag-AA7075-T6, and BMI-AA7075-T6 as well.

The potential distributions on the cathode outside the fastener (part f as shown in Figure 4. 1) for Ni-AA7075-T6, Ag-AA7075-T6 and BMI-AA7075-T6 systems are shown in Figure 4. 21. Figure 4. 18 shows the current distribution of part f for Ni-AA7075-T6 with a fastener gap ranging from 10µm to 0.3cm. At the same position d, the potential rises when the gap is narrower. For all the gap widths, the highest potential appears at f=0 and the potential then decreases and reaches its lowest value at f=5.8cm, the mouth of fastener. For the narrowest gap (w=10µm), the potential range is from -0.637V to -0.653V vs SCE. For the widest gap 0.3cm, the potential range is from -0.729V to -0.743V vs SCE. All the potentials are lower than the OCP of Ni in 0.1M NaCl (OCP=-0.340V vs SCE), which indicates that the entire external cathode (from f=0 to f=5.8cm) is polarized to provide the cathodic current. The potential distribution trend is similar for Ag-AA7075-T6 and BMI-AA7075-T6 systems as shown in Figure 4. 20 and Figure 4. 21, respectively. For Ag-AA7075, the potential ranges from -0.640V to -0.656V vs SCE for the 10µm gap and from -0.740V to -0.750V vs SCE for the 0.3cm gap. For BMI-AA7075, the potential ranges from -607 V to -0.637V vs SCE for the 10µm gap and from -

0.712V to -0.738V vs SCE for the 0.3cm gap. The OCP for Ag and BMI in 0.1M NaCl is 0.04V and -0.06V vs SCE respectively. So for these two galvanic systems, the cathodes are also fully activated to provide cathodic current.

Figure 4. 21 to Figure 4. 23 show the corresponding cathode current density along outside of fastener for all the three galvanic systems. As shown in Figure 4. 21, the magnitude of current density is higher when the gap is wider for Ni-AA7075-T6. The similar trend was observed for both Ag-AA7075-T6 and BMI-AA7075-T6 system as well.

4.3.2.3. Potential Distribution as a function of [Cl-]

Figure 4. 24 shows the potential distributions as a function of distance d inside the fastener gap (from d=0cm to d=1.2cm) for both 0.6M NaCl and 2.8M NaCl solutions with Ni as the cathode material. Four gap widths, 10 μm, 20μm, 500 μm and 0.2cm, were selected. The polarization curve of AA7075-T6 in 2.8M NaCl after 100hrs of exposure (as shown in Figure 3.44 and Figure 3.45 in chapter 3) was used as the anodic boundary condition for 2.8M NaCl condition. For the both 0.6M and 2.8M NaCl solution, the potential decreases with the increase of distance d, i.e., lower potential at the bottom of the gap. With the same gap width, the potential distribution slope over the distance d is flatter with the higher [Cl^-], i.e., the degree of potential change over the same distance is lower. For w=10 μm, the potential ranges from -0.654V (d=0cm) vs SCE to -0.758V (d=1.2cm) vs SCE for 0.6M NaCl (the degree of potential change is 87mV/cm) and from -0.673V to -0.746V vs SCE for 2.8M NaCl (the degree of potential change is 60mV/cm). For w=0.2cm, the potential ranges from-0.743V to -0.753V vs SCE for 0.6M NaCl (the degree of change is 8mV/cm) and -0.740V to -0.743V vs SCE for 2.8M NaCl (the degree of change is

2.5mV/cm). For all the given conditions, the potential is still higher than E_{rp} (E_{rp}=-0.82V vs SCE).

4.3.2.4. Potential Distribution as a function of cathode-to-anode area ratios

The effect of cathode-to-anode area ratio is also discussed. To simplify the study, the area of cathode outside of fastener gap (part of “f”) is kept as a constant, while the ratio of cathode (boundary 2) to anode (boundary 3) inside the fastener is adjusted to study its effect on the resulting potential and current density along the coupling interface. For this study, Ni-AA7075-T6 in 0.6M NaCl was selected as an example with two gap width, 20um and 0.2cm.

Figure 4. 25 shows the potential distribution along the anode interface (along distance d) as a function of cathode-to-anode area ratios from 3:1, 2:1, 1:1, 1:2, 1:3 and 0:4 (all anode) with a 0.2cm gap width. For all of the area ratios, the potential decreases with the increase of d, i.e., the potential is highest at the mouth of fastener. At the same position d, the highest potential appears at the higher cathode-to-anode area ratio and decreases with a decrease of cathode-to-anode area ratio. For example, for a cathode-to-anode area ratio=3:1, the potential ranges from -0.733V (d=0cm) to -0.745V (d=1.2cm) vs SCE. For cathode-to-anode area ratio=1:3, the potential ranges from -0.748V (d=0cm) to -0.757V (d=1.2cm) vs SCE, which is overall lower than the ones with higher cathode-to-anode area ratio. Figure 4. 26 shows the corresponding current density distribution along the coupling interface for 0.2cm gap. The current density is converted by according to i(E) function of anodic polarization of AA7075 in 0.6M NaCl, The effect of

cathode-anode area ratio on the current density is thus similar as its on the potential distribution. At the same position d, the higher cathode-to-anode area ratio results in higher current density value. For cathode-to-anode area ratio=3:1, the current density is 6.34A/m^2 (0.634x10^{-3} A/cm^2) at d=1.2cm. For cathode-to-anode area ratio=1:3, the current density is lower, 2.07A/m^2 (0.207x10^{-3} A/cm^2) at d=1.2cm.

Figure 4. 27 and Figure 4. 28 show the potential and current density distributions along the anode interface inside the fastener with a gap width of 20um. The trends of both potential and current density distribution are similar to the ones with the wider gap. The slope for both the potential and current density distribution is steeper compared to the ones with the wider gap. As a comparison, for cathode-to-anode area ratio=3:1, the potential at d=0cm is -0.656V vs SCE. At d=1.2cm, the potential and the current density is -0.746V vs SCE and 4.58A/m^2 (0.458x10^{-3} A/cm^2), respectively. For cathode-to-anode area ratio=1:3, the potential is -0.686V vs SCE at d=0cm. At d=1.2cm, the potential is -0.767V vs SCE , and the current density is 1.625A/m^2 (0.163x10^{-3} A/cm^2).

.

4.3.2.5. Potential Distribution as a function of electrolyte layer thickness (WL)

The effect of electrolyte layer thickness (indicate as WL in Figure 4. 1) on the potential distribution along the coupling interface under the atmospheric exposure condition was also studied. The WL studied were 25um, 100um and 200um. Ni-AA7075-T6 in 0.6M NaCl was used to illustrate the effect of WL with different gap width (0.2cm, 100µm and 50µm.)

Figure 4. 29 shows the effect of WL on the potential distribution along coupling interface with gap widths of 0.2cm, 100µm and 50µm. For all the conditions, the potential decreases with the increase of d. For the wider gap of 0.2cm, the potential at the same position (the same distance d) decreases with the decrease of WL. For 200µm WL, the potential at d=0cm is -0.746V vs SCE and -0.756V vs SCE at d=1.2cm. For 100µm WL, the potential at d=0cm decreases by 7mV to -0.753V vs SCE and by 4mV to -0.760V vs SCE at d=1.2cm. For 25µm WL, the potential at d=0cm further decreases by 22mV to -0.768V vs SCE and by 16mV to -0.772Vvs SCE at d=1.2cm.

For the 100µm gap width, the effect of the WL on the potential change is less. With a 200µm WL, the potential at d=0cm is -0.708V vs SCE and -0.757V vs SCE at d=1.2cm. For a thinner WL of 100µm, the potential drops by 6mV to -0.714V vs SCE at d=0cm and by only 1mV to -0.758V vs SCE at d=1.2cm. More discussion is included in the following section 4.5.

4.3.2.6. Potential Distribution as a function of PVC

The pigment volume concentration, PVC, is an important design parameter in coatings that include inhibitors. PVC is defined as the volume of pigment compared to the volume of all solids. In the real application, a layer of coating containing noble materials particles is designed to be applied upon AA7075-T6 substrate. PVC is thus used to represent the percentage of noble materials particles within the coating, assuming all particles are electrically connected to assure the conductivity. Ag-AA7075-T6 system in 0.6M NaCl is used as an example for this study. Four PVC value, 40%, 60%, 80% and 100% are used. The change of PVC is implemented by modifying the cathodic boundary condition of boundary 2. The adjusted boundary condition is the original boundary condition, (i.e., in this case, the i(E) curve of Ag in 0.1M NaCl from Figure 4. 7) multiplied by the percentage of PVC value. For example, the new boundary condition for PVC 40% is the original i(E)*40%.

Figure 4. 30 and
Figure 4. 31 show the potential distribution along coupling surface vs distance d for both 0.2cm gap and 20µm gap. With all the PVC values, the potential decreases with the increase of d distance. Compared with the 20µm gap, the slope of curve is flatter for 0.2cm gap, i.e., the change of potential with the same change of distance d is less than the ones in the narrower gap. For example, for 0.2cm gap with 80%PVC, the potential at d=0cm is -0.753V vs SCE and at d=1.2cm, the potential is -0.759vs SCE. The change of the potential is 5mV/cm. For 20µm gap, the potential at d=0cm is -0.683V vs SCE and at d=1.2cm is -0.762V vs SCE. The change of the potential is 62mV/cm, much more than the ones in 0.2cm gap. Similar trends can be attained for PVC 60% and 40% as well according to the figures.

The decrease of PVC also decreases the potential at the same distance d. For the 0.2cm gap, at d=0cm, the potential with 100%PVC is-0.749V vs SCE, and it then decreases to -0.753V vs SCE at PVC 80%, to-0.761V vs SCE at PVC 60%, and -0.778V vs SCE at PVC 40%, respectively. Overall, the potential changes by 29mV when PVC decreases from 100% to 40%. Similarly, for the 20µm gap, at d=0cm, the potential with 100%PVC is -0.675V vs SCE, and it then decrease to -0.683V vs SCE at PVC 80%, to-0.694V vs SCE at PVC 60%, and -0.718V vs SCE at PVC 40%, respectively. The overall change of potential is 43mV from PVC 100% to PVC 40%.

4.3.3. Condition 3: Propagation stage with cathode in the 0.1M NaCl and anode (AA7075-T6) in 0.6M NaCl after 100hrs exposure with addition of inhibitors: Steady State

The introduction of inhibitors is one of the potential mitigation strategies for the designed engineering structure. As discussed in previous sections, the choice of boundary condition can strongly affect the output results of modeling. In the present study, inhibitor effects on the oxygen reduction rate (ORR) of the noble metals were determined and the results were used as a modified cathode boundary condition to study the effect of such an inhibitor on the stability of the localized corrosion via modelling work.

4.3.3.1. The effect of Inhibitors on the ORR of noble materials

$NaVO_3$ was selected as a candidate inhibitor in the present research to study its effect on oxygen reduction rate on noble materials as it has been shown to be a potent oxygen reduction inhibitor[13]. The small amount of $NaVO_3$ (50mM/10mM) is effective to change the cathodic kinetic according to the previous research[13]. The solution, selection of noble materials and the details of the cathodic polarization tests were listed in section 4.2.

The effect of inhibitor concentration on the cathodic polarization behavior of Ni is shown in Figure 4. 32. The diffusion limited current density for oxygen reduction is approximately $3x10^{-5}A/cm^2$ without the inhibitor, but it is reduced in the presence of the inhibitor ($NaVO_3$) by more than an order of magnitude, becoming $1x10^{-6}$ A/cm^2 for a solution with 0.05M $NaVO_3$, and to $2x10^{-6}$ A/cm^2 for a solution with 0.01M $NaVO_3$. These results agree with Jakab *et al.* [12] who found that the inhibition effect of the $NaVO_3$ on oxygen reduction rate is not significantly dependent on its concentration.

Figure 4. 33 and Figure 4. 34 show the effects of the inhibitor on the cathodic kinetics on the other different noble materials. The ORR decreases from $4x10^{-5}A/cm^2$ to $1x10^{-5}A/cm^2$ in the presence of the inhibitor for BMI, but it did not change the rate appreciably for silver. The reasons for the above experimental observations are not clear. However, the goal of the present research is not focused on understanding the mechanism of the inhibitor, but to predict what its effect would be on galvanically induced localized corrosion on AA7075-T6. This effect is to be investigated in the following sections.

The likely mechanism for the inhibitors to reduce ORR reaction is due to the change of coverage on the reaction surface which will affect the number of sites at which the ORR is able to take place. This inhibitor may also impact the anodic reaction. However, the focus of this research is the study the sensitivity of galvanic interactions to characteristics of the cathode reaction via the introduction of inhibitors, for the potential development of a mitigation strategy. The detailed mechanism of how the inhibitor works is beyond our scope.

4.3.3.2. Boundary condition and Subdomain set up

The subdomain (0.6M NaCl) and geometry remain the same as the ones in condition 2. The i(E) polarization curves with the addition of inhibitors was used to replace the boundary condition in boundary condition 1 and 2. For anode boundary condition 3, the boundary condition remains the same, using the anodic polarization of AA7075 from 0.6M NaCl after 100hrs of exposure.

4.3.3.3. The effect of inhibitors on the potential distribution

Two examples Ni-AA7075-T6 and BMI-AA7075 in 0.6M NaCl with 0.2cm and 20µm gap were discussed in the present study as the $NaVO_3$ inhibitors were observed to have no significant effect on the ORR kinetics of Ag according to section 4.3.3.1.

Figure 4. 35 shows the potential distributions along coupling surface inside the fastener gap for Ni-AA7075-T6 system. Two gap widths, 0.2cm and 20µm are selected. The potential distributions without inhibitors are also plotted for comparison. For both gap widths, the introduction of the inhibitors brings the overall potential down as well as changing the slope of the plots. For the 0.2cm gap without inhibitors, the potential at d=0cm is-0.743V vs SCE and at d=1.2cm, the potential is -0.753V. The degree of potential change over d is 8mV/cm. For the same gap with inhibitors, the potential at d=0cm lower by 71mV to -0.814V vs SCE, compared with the one without inhibitors. Because of the flatter slope, at d=1.2cm, the potential does not change a lot and stay at -0.814V.

For the 20um gap without inhibitors, the potential at d=0cm is -0.671V vs SCE and -0.757V vs SCE at d=1.2cm. The degree of the potential is 72mV/cm. With inhibitors, the potential at d=0cm is lowered to -0.752V vs SCE and to -0.772V vs SCE at d=1.2cm. However, due to the flatter slope, the degree of potential change is less, only 16mV/cm over the distance d.

Similar trends were observed in
Figure 4. 36. For BMI-AA7075-T6 in 0.6M NaCl, the potential also decreases with the addition of inhibitors, while the slope of the potential distribution vs distance d does not change a lot by adding the inhibitors. For the 0.2cm gap without inhibitors, the potential at d=0cm is-0.748V vs

SCE and at d=1.2cm, the potential is -0.756V. The degree of potential change is 6.7mV.cm. For the same gap with inhibitors, the potential at d=0cm decrease by 36mV to -0.784V vs SCE. Because of the flatter slope, at d=1.2cm, the potential changes by 26mV to -0.782V vs SCE. The degree of potential change is 1.7mV/cm.

For the 20um gap without inhibitors, the potential at d=0cm is -0.675V vs SCE and -0.759V vs SCE at d=1.2cm. The change of the potential is 70mV/cm, while with inhibitors, the potential at d=0cm decrease to -0.725V vs SCE and to -0.789V vs SCE at d=1.2cm. The change of the potential is 53mV/cm across the distance d.

4.3. 4. Condition 4: a stationary model using the boundary conditions extracted from experiments on artificial pit samples in 80% and 100% saturated $AlCl_3$

In order to further consider the acidification with the proceeding of hydrolysis, anodic boundary condition attained from artificial pit samples in saturated $AlCl_3$ was used. The anodic kinetics are shown in Figure 2.40 in Chapter 2. The anodic kinetics from 80% and 100% saturation of $AlCl_3$ were selected to ensure the corrosion is under stable propagation status with the hydrolysis reaction.

For the cathode physical boundary, the cathode boundary condition and subdomain is the same as in Condition 2, section 4.3.2. In all cases, interpolation was used to input the boundary condition from the experimental polarization curves through COMSOL.

4.3.4.1. The comparison of potential distribution along Ni-AA7075 interface for the anodic condition in 0.6M NaCl and $AlCl_3$

In this section, a Ni-AA7075-T6 fastener geometry is discussed. As shown in Figure 4.1, the boundary condition 1 and 2 are the boundary condition for cathode, which is the same as in section 4.3.2, a cathodic polarization curve from 0.1M NaCl. Boundary condition 3 is the boundary condition for anode. Anodic kinetics attained from 80% and 100% $AlCl_3$ from Figure 2.40 are used.

Figure 4. 37 shows the potential distribution along distance d, with the anode boundary condition in 80% $AlCl_3$. with gap width 20μm and 0.2cm. For the narrow gap 20μm, the potential changes from -0.775V vs SCE at d=0cm to -0.845V vs SCE at d=1.2cm. For the gap of 0.2cm, the slope of potential vs d is flatter. At d=0cm, the potential is -0.843V vs SCE, and at d=1.2cm, the potential is -0.851V vs SCE.

Similarly, in

Figure 4. 38, the plots show the potential distribution along distance d, with the anode boundary condition in 100% $AlCl_3$ with two gap widths. For the narrow gap 20μm, the potential changes from -0.781V vs SCE at d=0cm to -0.856V vs SCE at d=1.2cm. For the gap of 0.2cm, the slope of potential vs d is flatter. At d=0cm, the potential is -0.844V vs SCE, and at d=1.2cm, the potential is -0.851V vs SCE.

In both of the figures, the potential distributions from condition 2 in section 4.3.2, of which the anode boundary condition is under 0.6M NaCl with 100hours exposure were plotted for the comparison. The potential is higher for the ones in bulk solution 0.6M NaCl than in $AlCl_3$.

4.4. Atmospheric Exposure

In addition to the fastener geometry, a simple planar configuration was also studied. The details of the geometry are shown in Figure 4. 39. This configuration was used to simulate the galvanic coupling test setting under the atmospheric exposure from chapter 3. The effect of environmental parameters, including cathode-to-anode area ratio, the exposure time (33hrs, 66hrs, and 100hrs) and the change of relative humidity RH (98% and 90%), on the corrosion stability of the atmospheric exposed galvanic system were studied through modelling. The calculated potential distribution along the coupling interface results are compared with the experimental results (SKP measurements) from chapter 3 to evaluate the validation of the modelling works.

4.4.1. Geometry and Boundary Condition Setting

The geometry is shown in Figure 4. 39. Four cathode-to-anode area ratio: 1:1, 30:1, 60:1 and 100:1 were selected in this study to be consistent with the ones used for the experimental tests in chapter 3. The length of the cathode and anode is also the same as the actual length used for the experimental setting. The details are listed in table 4.3.

In the present study, a Ni-AA7075-T6 galvanic system is selected as an example. The cathodic boundary condition was extracted from the i(E) curves generated by the polarization curve of Ni in 0.1M NaCl (as shown in Figure 4. 3). The anodic boundary condition were extracted from the i(E) polarization curve of AA7075-T6 in 0.6M NaCl and 2.8M NaCl, with three exposure time length (33hrs, 66hrs and 100hrs), depending on the condition of RH and exposure time. In all cases, interpolation was used to connect the data points where necessary. The details of the anodic polarization curves for each condition are shown in Figure 3.45-3.46 in Chapter 3.

4.4.2. Potential distribution as a function of exposure time

Figure 4. **40** shows the potential distribution along the anode site for Ni-AA7075-T6 with cathode-to-anode area ratio 1:1 after 100hrs of exposure. The solution used is 0.6M NaCl. The x axis represents the distance of anode site from the cathode/anode interface "I". The potential distribution is a concave-up shape while decreasing when the anode is distant from the interface. At the same position, the lowest potential appears after 100hrs exposure. The highest potential appears after 66hrs exposure. For 33hrs exposure, at a=0, the potential is-0.703V vs SCE, and at a=1.2cm, it is -0.719V vs SCE. For 66hrs exposure, at a=0cm, the potential is -0.694V vs SCE and at at a=1.2cm, it is -0.710vs SCE. For 100hrs exposure, at a=0cm, the potential is -0.753V vs SCE, and it is -0.757V vs SCE at a=1.2cm. The degree of potential change per distance is 13mV/cm for 33hrs exposure, 13mV/cm for 66hrs exposure and 3mV/cm for 100hrs exposure. The slopes for 33hrs and 66hrs exposure are the same, while for 100hrs, the slope is flatter, and the potential change along the entire anode site is therefore less.

4.4.3. Potential distribution as a function of RH

Figure 4. 41 shows the potential distribution along the anode site for Ni-AA7075-T6 with cathode-to-anode area ratio 1:1 after 100hrs of exposure in 2.8M NaCl. In this case, the highest potential at the same distance still appears at 66hrs, while the lowest potential appears after 33hrs of exposure. For 33hrs exposure, at a=0, the potential is-0.759V vs SCE, and at a=1.2cm, with a flat slope, it remain as -0.759V vs SCE. For 66hrs exposure, at a=0cm, the potential is -0.576V vs SCE and at at a=1.2cm, it slightly decreases to -0.579vs SCE. For 100hrs exposure, at a=0cm, the potential is -0.744V vs SCE, and it is -0.748V vs SCE at a=1.2cm. The degree of potential change per distance is 0mV/cm for 33hrs exposure, 2.5mV/s for 66hrs exposure and 3mV/cm for 100hrs exposure. Compared with the ones in 0.6M NaCl, at 33hrs exposure, the potential for 2.8M NaCl is lower with a given distance a. And after 66hrs exposure and 100hrs exposure, the potential for 2.8M NaCl overall is higher than the ones in 0.6M NaCl. Also, the slopes of 2.8M NaCl for 33hrs and 66hrs exposure is flatter than the ones in 0.6M NaCl, due to the less ohmic resistance in a higher [Cl$^-$].

4.4.4. Potential distribution as a function of Cathode to Anode area ratio.

Figure 4. 42, Figure 4. 43 and Figure 4. 44 show the effects of cathode-to-anode area ratio (30:1, 60:1 and 100:1) on the potential distribution vs distance a for three exposure times, 33hrs, 66hrs and 100hrs. As shown in the figures, independent of the exposure time, a lower potential appears at the lower cathode-to-anode area ratio for any given position. In

Figure 4. 42 with 33hrs of exposure, the potential at a=0cm is -0.664V vs SCE for 30:1, increases to -0.660V vs SCE for 60:1, and further increases to 0.644V vs SCE for 100:1. With 66hrs exposure as shown in Figure 4. 43, the potential at a=0cm is -0.648V vs SCE for 30:1, increases to -0.641V vs SCE for 60:1, and then increases to -0.635V vs SCE for 100:1. With

100hrs exposure in Figure 4. 44, the potential at a=0cm is -0.746V vs SCE for 30:1, increases to -0.738V vs SCE for 60:1, and then increases to -0.731V vs SCE for 100:1.

4.5. Discussion

4.5.1. The cathode and anode current

In the modeling work of this chapter, total cathode current should be equal to total anode current which can be calculated by integrating the current density along the exposure surface. For example, according to Figure 4. 15 and Figure 4. 21, the total cathode current from both inside and outside the fastener gap is -1.5A. The total anode current inside fastener gap is 1.5A, which is equal to the total cathode current generated.

4.5.2. The effect of anode boundary condition

As shown in

Figure 4. **37** and

Figure 4. **38**, two sets of anode boundary condition were compared. One condition (A) is assumed that the anode is in 0.6M NaCl after 100hours exposure. The boundary condition was extracted from the anodic polarization curve of AA7075-T6 bulks samples after 100hours galvanic coupling exposure with Ni.

The other condition (B) is assumed that the anode is in saturated $AlCl_3$ to simulate the aggressive local chemistry due to the hydrolysis reaction with the propagation of the pitting. The boundary condition was extracted from the anodic polarization curve of AA7075 artificial pit samples in 80% and 100% saturated $AlCl_3$.

For condition A, it considers the effect of exposure time as well as the effect from the coupling cathode materials. Also, since E_{rp} was measured in 0.6M NaCl, it is easy to compare the potential along cathode-to-anode interface with E_{rp} to predict the corrosion stability of the whole system.

For condition B, it considers the acidification of the local chemistry which typically occurs when the corrosion product are generated due to the high dissolution rate. With this boundary condition, as shown in
Figure 4. 37 and
Figure 4. 38, the potential distribution along the coupling interface is lower. However, this boundary condition does not include any time exposure considerations. Also, the effectiveness of E_{rp} from previous measurement in the acidic solution was not evaluated in the present studied.

4.5.3. The effect of cathode

The effect of cathode for the fastener engineering geometry on the distribution along the cathode-anode interface inside the fastener gap (distance d) is discussed in this section. Figure 4. 45 and Figure 4. 46 show the potential at the mouth of the fastener (d=0cm) and at the end of the gap (d=1.2cm) when AA7075-T6 is coupled with Ni, Ag, BMI, respectively. The potential is plotted vs gap width, w, to illustrate the effect of the gap width as well as the selection of noble materials on the potential distribution. The data for the plots were drawn from
Figure 4. 12, Figure 4.13 and Figure 4. 14.

As shown in Figure 4. 45, at d=0cm, for all the three materials, the potential decreases with the increase of the gap width. While in Figure 4. 46, at d=1.2cm, at the bottom of gap, the potential increase slightly with the increase of the gap width. With a narrower gap, more ohmic drop is created inside the fastener gap, which reduces the polarization at the mouth of the fastener whereas there is much less effect at the bottom of the crevice.

For all the gap widths, the highest potential is present on BMI, and the lowest is on Ag as shown in the above two figures. This discrepancy is explained by the different limited current density of the three materials, as shown in Figure 4. 47. At the range of coupling potential (-0.7V to -0.8V vs SCE), the diffusion limited current density of BMI is higher than Ni, and Ag, which causes it to polarize the AA7075-T6 to a higher potential. The potential at d=1.2cm is also compared with the E_{rp} (=-0.82V vs SCE) from the measurement referred from Chapter 2. For all the gap width, with all the noble materials, the potential is higher than E_{rp}. At d=1.2cm, the potential is the lowest on the anode site, while since it is still higher than E_{rp}. This indicates that the whole system, regardless of the selection of noble materials, is expected to have continuous corrosion propagations.

The discussion of the effect of the noble materials gives the insights of the importance of the selection of noble material on the corrosion resistance for the designed engineering geometry in practical applications. According to the current findings, silver would lead to the lowest coupling potential at the anode site due to the lower diffusion limited current density at the potential of interest. Combined with other mitigation strategy, a potential even lower than E_{rp} may be implemented to assure the corrosion protection.

4.5.4. The effect of [Cl$^-$]

Similarly, the effect of [Cl$^-$] on the potential distribution along distance d is discussed. Ni-AA7075-T6 system is selected for this study. Two [Cl$^-$], 0.6M NaCl and 2.8M NaCl were selected, which are equivalent to 98%RH and 90%RH, respectively, for the atmospheric exposure. In practice, the fastener geometry can be applied to various environment including the full immersion and atmospheric exposure. So it is important to understand the corresponding [Cl$^-$] to these environments.

Figure 4. 48 and Figure 4. 49 show the potential vs gap width at d=0cm and d=1.2cm. The plots were drawn using data from
Figure 4. 24. In Figure 4. 48, the potential with each gap width for 2.8M NaCl and 0.6M NaCl at d=0cm are compared. The potential for 0.6M NaCl with narrower gap (10µm and 20µm) is higher than the one of 2.8M NaCl and lower with wider gap (0.2cm). In Figure 4. 49, the potential for 0.6M NaCl at d=1.2cm with all the gap width is lower than the ones of 2.8M NaCl. The degree of potential change with the same distance d at each gap width for 0.6M NaCl is higher, which is due to the higher ohmic drop resulting from the less ionic conductivity in the solution with lower [Cl$^-$]

From the current findings, the lower [Cl$^-$] allows a lower potential on the anode site (d=1.2cm) as shown in Figure 4. 49 which favors the corrosion protection. This understanding facilitates the corrosion risk assessment as well as the decision making for the environment of application in both full immersion and atmospheric condition.

4.5.5. The Cathode-to-Anode area ratio

The effect of cathode-to-anode area ratio inside the fastener is studied to understand its impact on localized corrosion stability. In practical applications, changing the design of the cathode-to-anode area ratio is feasible to implement. An optimal cathode-to-anode area ratio under which the corrosion is minimized can be selected by comparing the potential and current density along coupling interface of each given area ratio with a given stability criterion . The Ni-AA7075-T6 in 0.6M NaCl system is selected for illustration. Two gap widths, 20μm and 0.2cm, representing the narrow/wide gap condition used, are discussed.

Figure 4. 50 shows the potential as a function of cathode-to-anode area ratio for the four given condition: the potential at d=0cm for 20um and 0.2cm gap and the potential at d=1.2cm for the same given gap width. For all the conditions, the potential decreases when the cathode-to-anode area ratio decreases. The change is more significant for 20μm at both d=0cm and d=1.2cm, which is due to the higher ohmic drop created from the narrower the gap.

The anodic current density at the bottom of the anode is also plotted in Figure 4. 51. The current density follows the polarization curve i(E), so the trend of current density change with the cathode-to-anode area ratio is consistent with that for the potential.

With a lower cathode-to-anode-area ratio, the cathodic current supply is less, which is taken into account to the decrease of both the potential and current density at the cathode-anode interface inside the fastener.

According to the current findings, with the given gap, less cathode inside the fastener gap results in the lower potential, which provides the insights for the practical design of determining the cathode-to-anode ratio for the engineering structure. While reducing the cathode material is likely to achieve the lower cathode-to-anode area ratio, other concerns such as the effectiveness of cathode material for the original purpose should also be taken into consideration.

4.5.6. The effect of electrolyte layer thickness (WL)

The electrolyte layer thickness is particularly important for the applications under atmospheric exposures. Three water layer thickness, 25um, 100um and 200um, are selected here for the discussion.

Figure 4. 52 and Figure 4. 53 show a case of Ni-AA7075-T6 in 0.6M NaCl, which corresponds to 98% RH under the thin water layer condition. For gap widths 0.2cm and 100µm, the potential decreases with the decrease of WL. With a thinner electrolyte layer, the amount of ions across the same distance along the cathode-to-anode interface is limited due to the limited space, the actual cathode-to-anode area ratio therefore decrease. And the resulting lower cathode-to-anode area ratio brings the potential down as well.

4.5.7. Conductivity in the atmospheric condition.

In chapter 3, the potential distributions along cathode-anode interface under atmospheric conditions for the planar configuration were measured with SKP. Given the same condition, the results from modelling are calculated with the experimentally-derived electrochemical boundary conditions. Figure 4. 54-Figure 4. 55, Figure 4. 56-Figure 4. 57, Figure 4. 58-Figure 4. 59 show the comparison with the potential distribution between experiment and calculated data for the various cathode-to-anode area ratio (1:1, 30:1, 60:1 and 100:1) after 33hrs, 66hrs and 100hrs of exposure. Although the trend of the potential distribution change is the same for both modelling and experimental results (potential decreasing with increasing distance from the cathode), the slope for the calculated results is much flatter. We speculate this discrepancy is caused by the following reason: In the modelling, the concentration of the thin electrolyte layer as well as the thickness of the electrolyte thickness is assumed to be constant over the time for all the exposures. Also, no chemical reactions were considered in the electrolyte. The conductivity and ohmic resistance of the solution therefore remains constant. However, in the actual exposure, the generation of corrosion products changes the conductivity of the solution as well as the shape of the electrolyte layers, which can increase the ohmic resistance and result in a steeper slope of potential along the cathode to anode interface.

The effects of changing the solution conductivity were studied to see if the modelling could approach the results of the experiments. Two changes are made in present work. First, the change of conductivity is implemented by changing the diffusivity and concentration of the species in the solution. Second, the change of the electrolyte layer thickness was allowed to change the ohmic resistance of the solution.

The conductivity in the binary solution (with Na^+ and Cl^- species) in the absence of concentration gradients is described as follows:

$$\kappa=F^2 \sum_i z_i^2 u_i c_i \qquad \text{Equation 4.2}$$

where, z_i is the charge of ion specie, $u_i$is the mobility of ion specie,

c_i is the concentration of specie. The mobility is experred by

$$u_i = \frac{D_i}{RT} \qquad \text{Equation 4.3}$$

Where D_i is the diffusivity of the specie and R is the gas constant ($8.31 J mol^{-1} K^{-1}$).

In the modelling, the reducing of conductivity κ of the NaCl solution is achieved by decreasing the diffusivity and concentration of two species to simulate the effects of the generation of corrosion products.

The original and modified D_i and c_i is listed in Table 4.4. Besides the conductivity modification, the water layer thickness is also reduced from 100μm to 50μm.

Figure 4. 60 shows the resulting conductivity-modified potential distribution with the comparison of the experimental results. As shown in the figure, with the lower κ, the slope for the potential distribution curve is steeper than the originally calculated one. However, the potential is still not as low as the ones from the measurement. The lower potential from the measurement may also cause by the change of local chemistry due to the anodic dissolution and their hydrolysis. The acidification is likely be accelerated with the coverage of corrosion products which can bring the anodic kinetics as well as the OCP of the anodic polarization curves down. For future work, the change of local chemistry due to chemical reactions may need to be taken into the consideration for a more precise prediction of the actual environments.

Reference

[1] A. Proust, G. Girardin, COMSOL Confererrnce paper, 2006.

[2] D. Mizuno, R.G. Kelly, Corrosion, submitted (Aug, 2012)

[3] N. Murer, N. Missert, R. Buchheit, COMSOL Conference paper, 2008.

[4] J. Xiao, S. Chaudhuri, *Electrochim. Acta* 2011, *56*, 5630.

[5] O. Guseva, P. Schmutz, T. Suter, O. von Trzebiatowski, *Electrochim. Acta* 2009, *54*, 4514.

[6] A. D. Scientific, T. Organisation, F. Bend, 1992, *180*, 15.

[7] A. Online, M. R. Ali, C. M. Mustafa, M. Habib, 2009, DOI 10.3329/jsr.vlil.1053.

[8] G. O. Ilevbare, J. R. Scully, J. Yuan, R. G. Kelly, *Corrosion* 2000, *56*, 227.

[9] M. W. Kendig, R. G. Buchheit, *Corrosion* 2003, *59*, 379.

[10] K. F. Khaled, *Corros. Sci.* 2010, *52*, 2905.

[11] M. A. Jakab, D. a. Little, J. R. Scully, *J. Electrochem. Soc.* 2005, *152*, B311.

[12] F. J. Presuel-Moreno, M. a. Jakab, J. R. Scully, *J. Electrochem. Soc.* 2005, *152*, B376.

[13] J. Wilson, Arwen and Scully, in *NACE Conf.*, 2011.

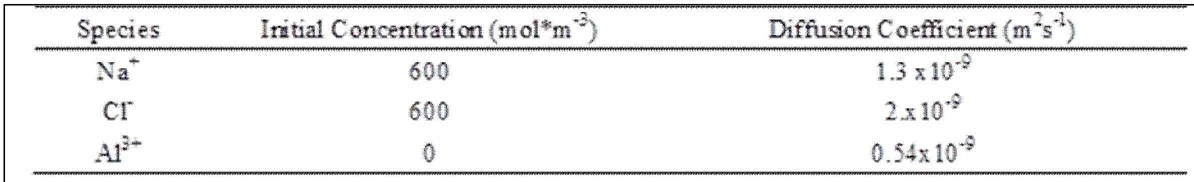

Species	Initial Concentration ($mol*m^{-3}$)	Diffusion Coefficient (m^2s^{-1})
Na^+	600	1.3×10^{-9}
Cl^-	600	2×10^{-9}
Al^{3+}	0	0.54×10^{-9}

Table 4.1 Boundary condition of Noble Material-AA7075 Materials: Steady State Model

	Boundary 1&2 (Cathode)	Boundary 3(Anode)
Current Density (A/m^2)	Interpolation of Ag cathodic polarization in 0.1M NaCl from Figure 4.7	$i^p{}_a = i^p{}_{acorr}[\exp(\frac{E^p a_{corr} - V}{\alpha^p{}_a}) - \exp(\frac{E^p a_{corr} - V}{\beta^p{}_a})$
Flux (Mole/m^2/s)	N/A	$N_{Al}{}^{3+} = i^p{}_a/3F$; $E^p a_{corr}$ =-0.60433-0.07154*log([Al^{3+}])

Table 4.2 Boundary condition set up for modelling condition 1

Cathode-to-Anode Area Ratio	Length of Cathode (cm)	Length of Anode (cm)
1 to 1	1.2	1.2
30 to 1	7.5	0.25
60 to 1	15	0.25
100 to 1	25	0.25

Table 4.3 Area Ratio Condition set up

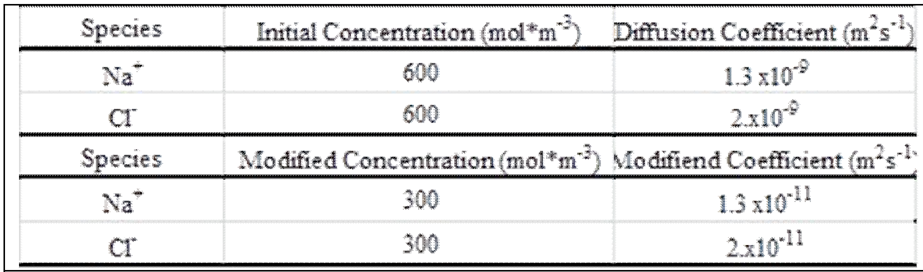

Species	Initial Concentration (mol*m^{-3})	Diffusion Coefficient (m^{2}s^{-1})
Na$^+$	600	1.3 x10^{-9}
Cl$^-$	600	2.x10^{-9}
Species	Modified Concentration (mol*m^{-3})	Modifiend Coefficient (m^{2}s^{-1}
Na$^+$	300	1.3 x10^{-11}
Cl$^-$	300	2.x10^{-11}

Table 4.4 Modification for the solution conductivity

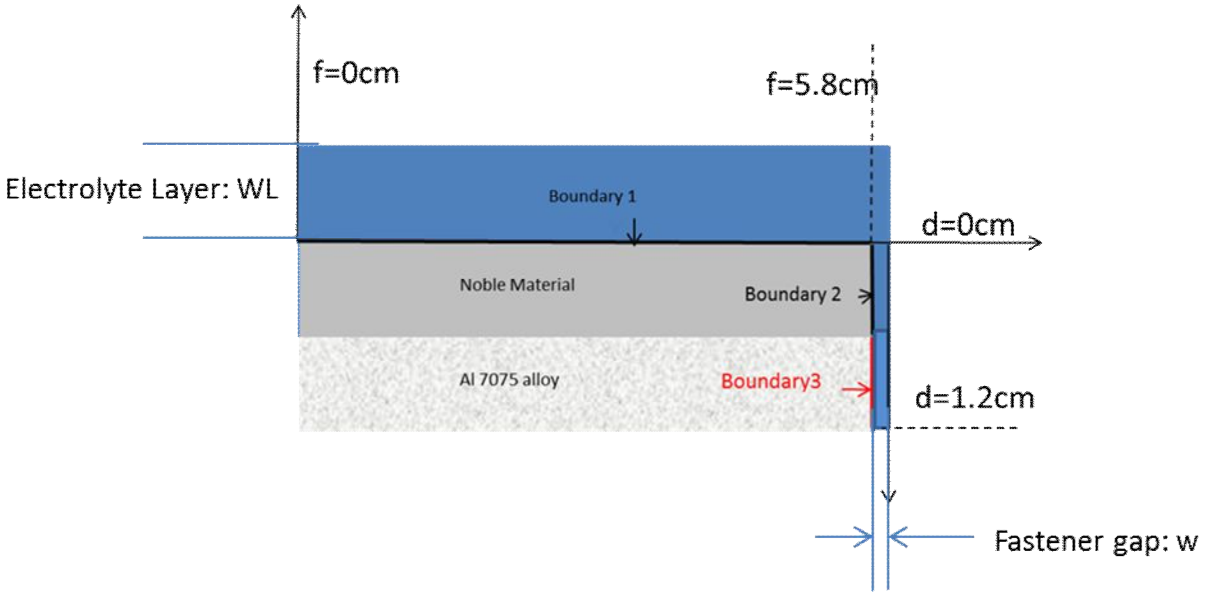

Figure 4. 1

Schematic demonstration of fastener geometry

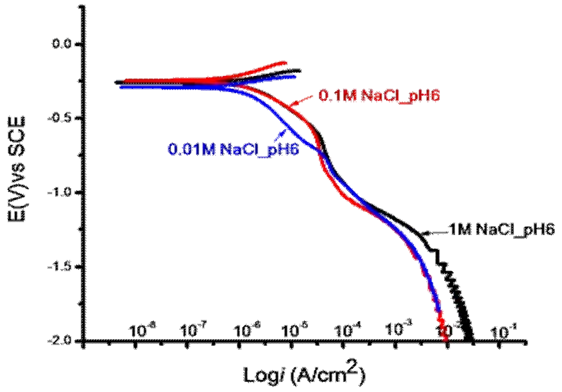 Figure 4. 2	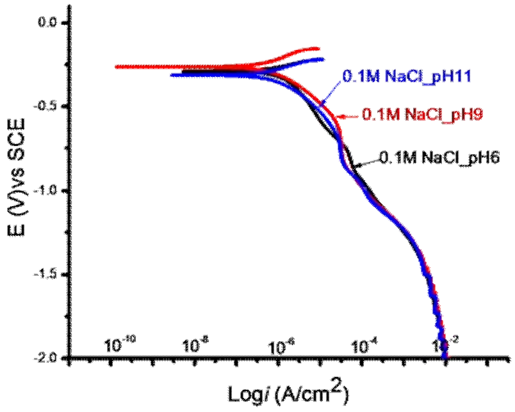 Figure 4. 3
Effect of [Cl$^-$] on Ni cathodic kinetics	Effect of pH on Ni cathodic kinetics
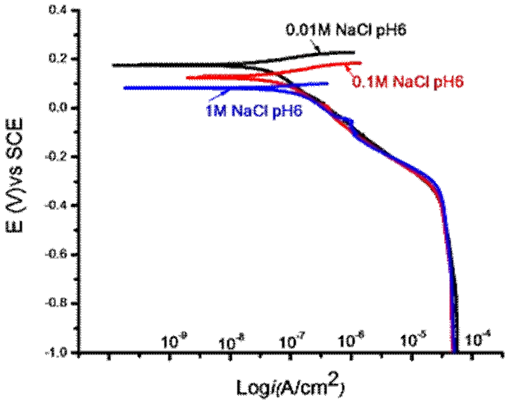 Figure 4. 4	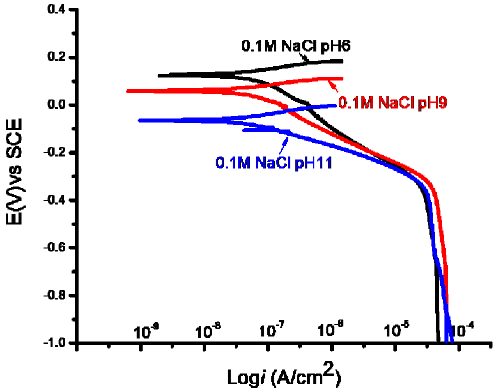 **Figure 4. 5**
Effect of [Cl$^-$] on BMI cathodic kinetics	Effect of pH on BMI cathodic kinetics

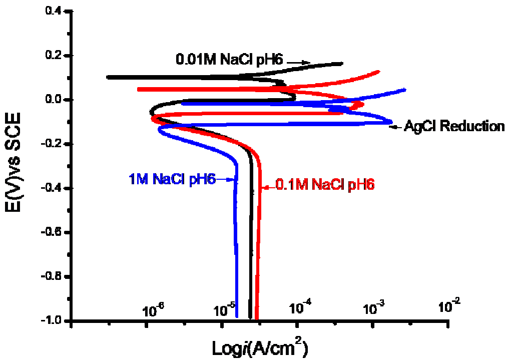

Figure 4. 6

Effect of [Cl⁻] on BMI cathodic kinetics

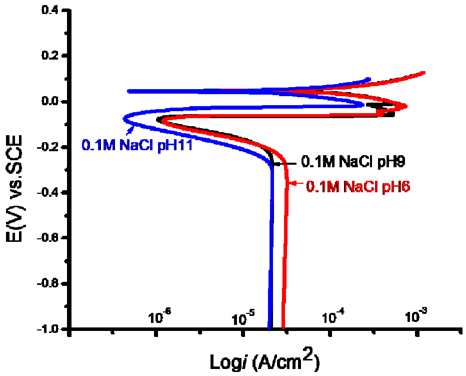

Figure 4. 7

Effect of pH on Ag cathodic kinetics

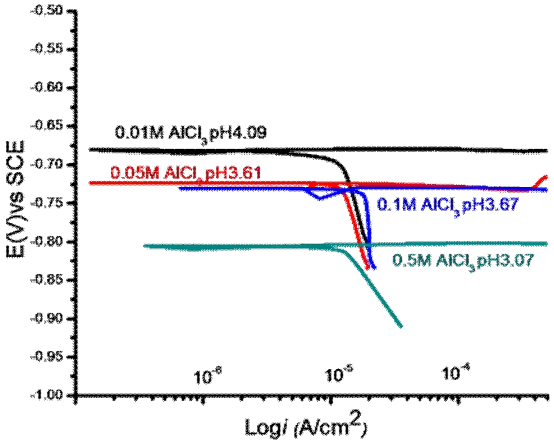

Figure 4. 8

Effect of $AlCl_3$ on AA7075-T6 anodic kinetics

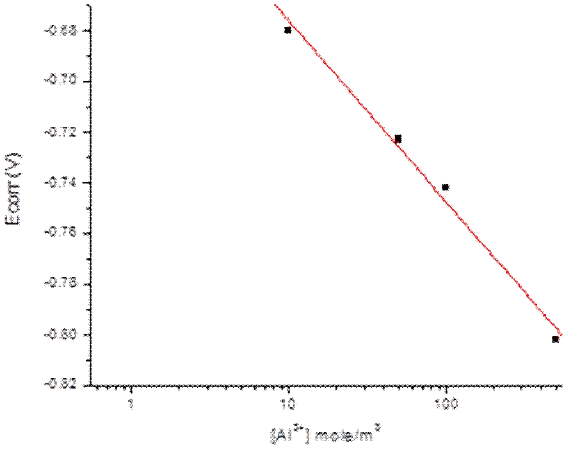

Figure 4. 9

OCP of AA7075-T6 in $AlCl_3$ with different concentration.

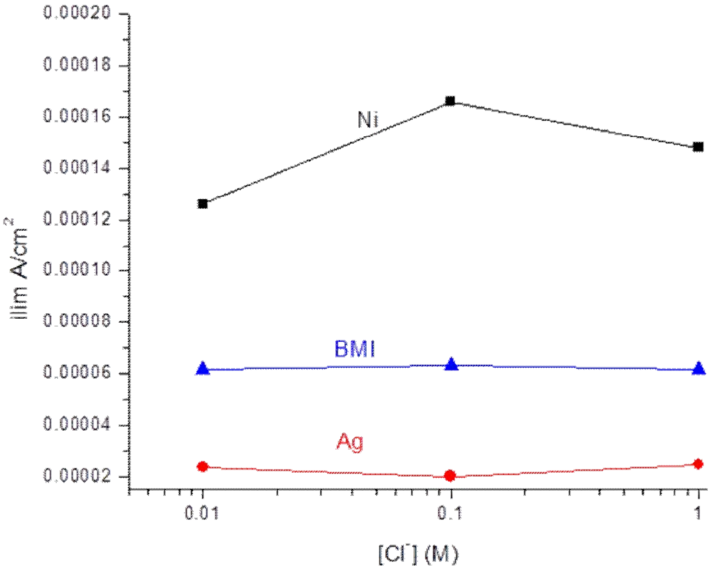

Figure 4. 10

The diffusion limited current density (assessed at ### V(SCE) for Ni, Ag, BMI as a function of [Cl$^-$]

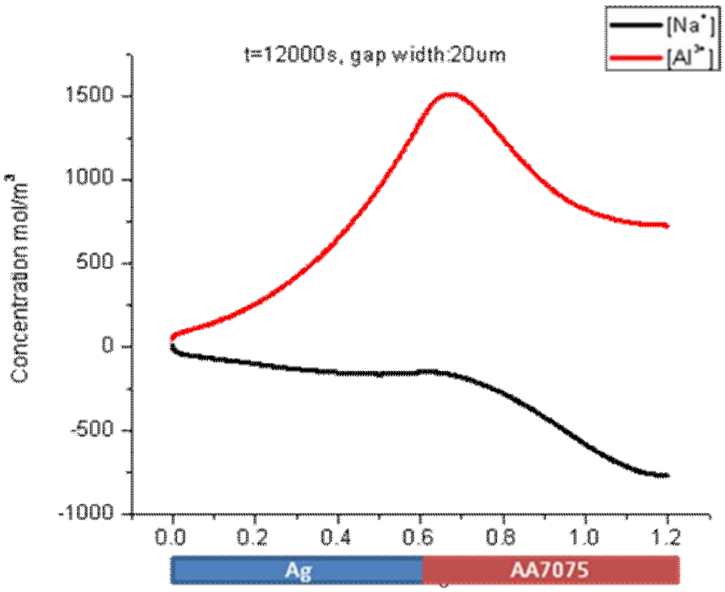

Figure 4. 11

COMSOL-calculated ionic concentration distributions for Na^+ and Al^{3+} along Ag-AA7075 interface. Polarization curve used for Ag was for 0.1 M NaCl , pH11 condition. Polarization curve used for AA7075 was for 0.5 M $AlCl_3$.

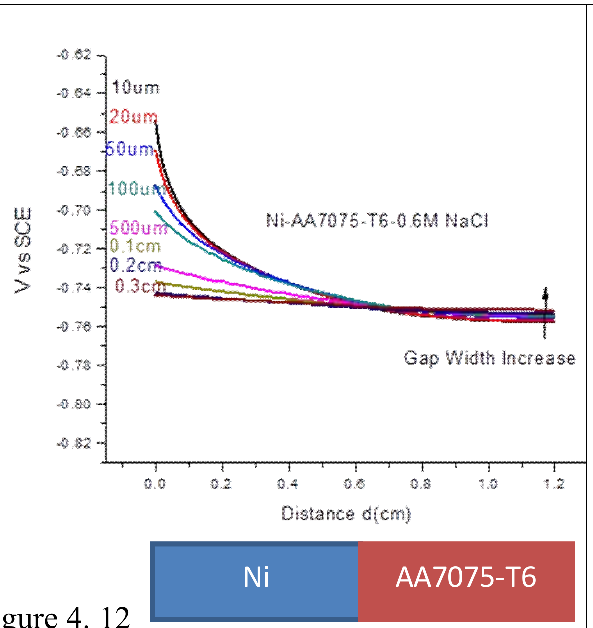

Figure 4. 12

Potential distribution along Ni-AA7075-T6 coupling interface for a fastener geometry with gap width from 10um to 0.3cm.

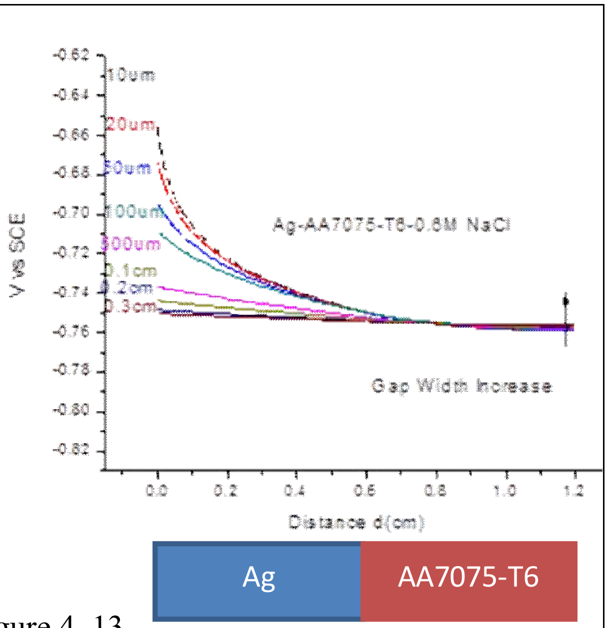

Figure 4. 13

Potential distribution along Ag-AA7075-T6 coupling interface for a fastener geometry with gap width from 10um to 0.3cm.

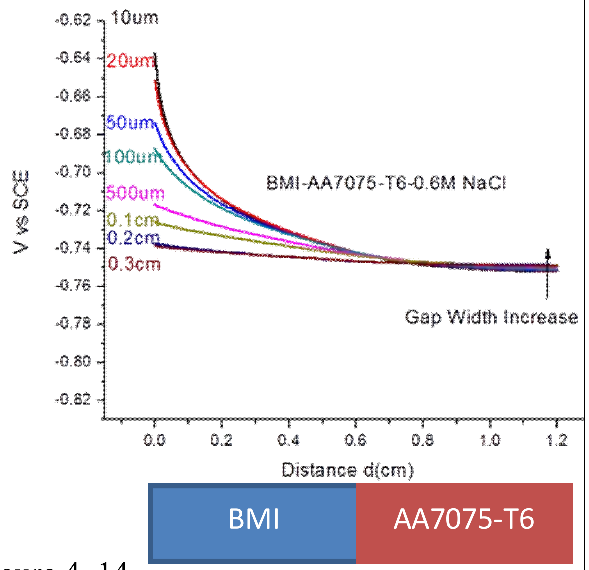

Figure 4. 14

Potential distribution along BMI-AA7075-T6 coupling interface for a fastener geometry with gap width from 10um to 0.3cm.

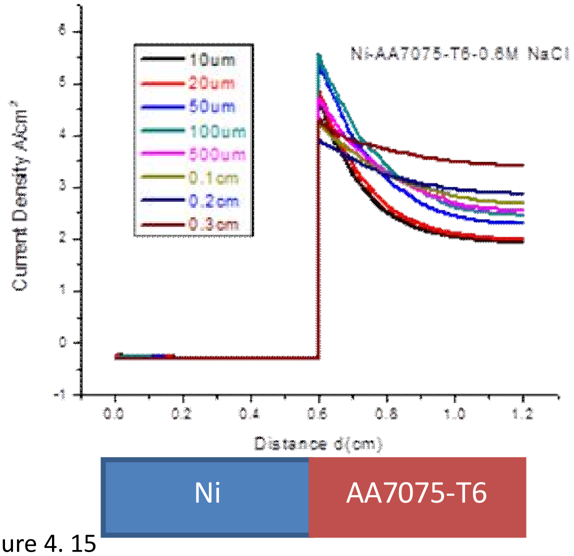 Figure 4. 15	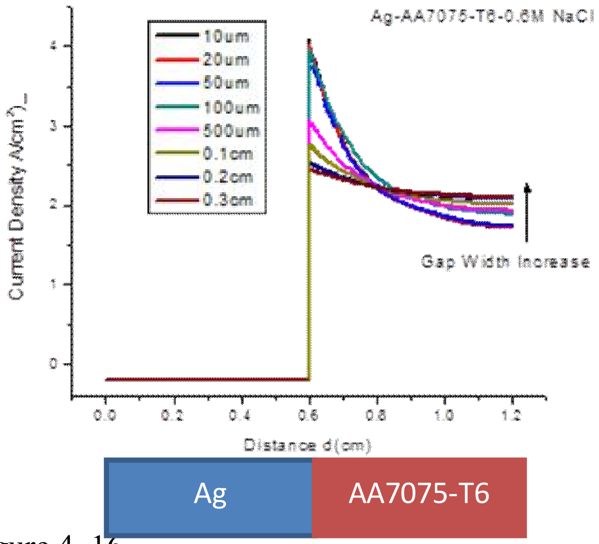 Figure 4. 16
Current density distribution along Ni-AA7075-T6 coupling interface for a fastener geometry with gap width from 10um to 0.3cm.	Current density distribution along Ag-AA7075-T6 coupling interface for a fastener geometry with gap width from 10um to 0.3cm.
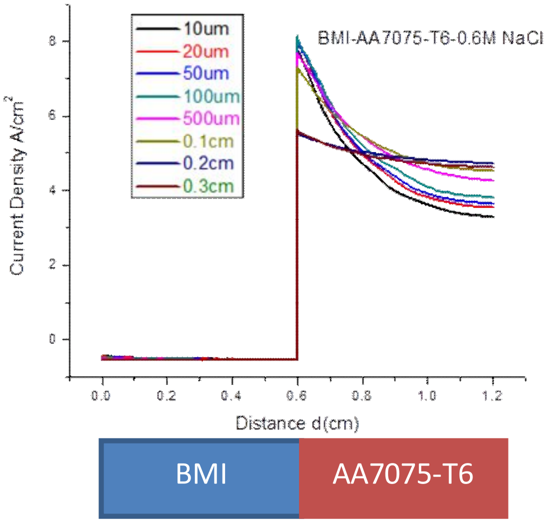 Figure 4. 17	
Current density distribution along BMI-AA7075-T6 coupling interface for a fastener geometry with gap width from 10um to 0.3cm.	

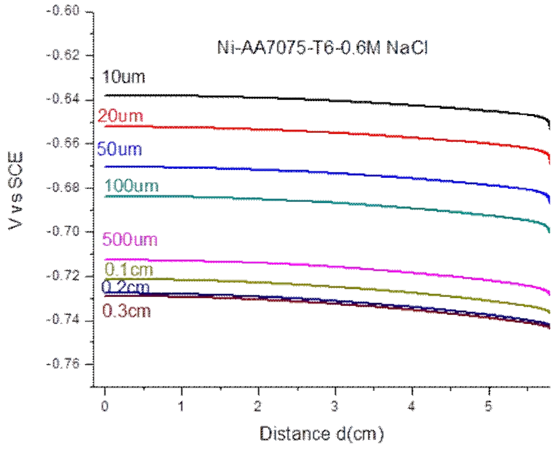

Figure 4. 18

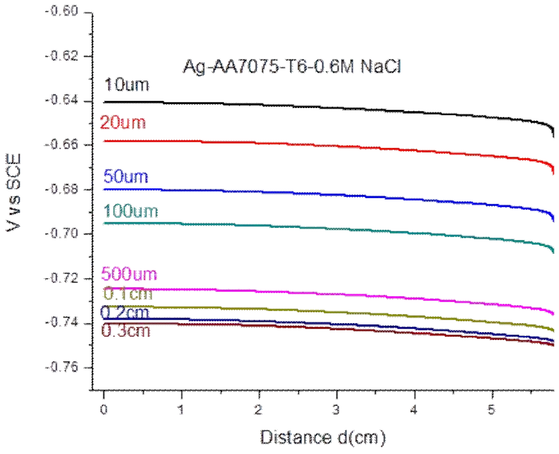

Figure 4. 19

Potential distribution along an external cathode for Ni-AA7075-T6 coupling interface for a fastener geometry with gap width from 10um to 0.3cm.

Potential distribution along an external cathode for Ag-AA7075-T6 coupling interface for a fastener geometry with gap width from 10um to 0.3cm.

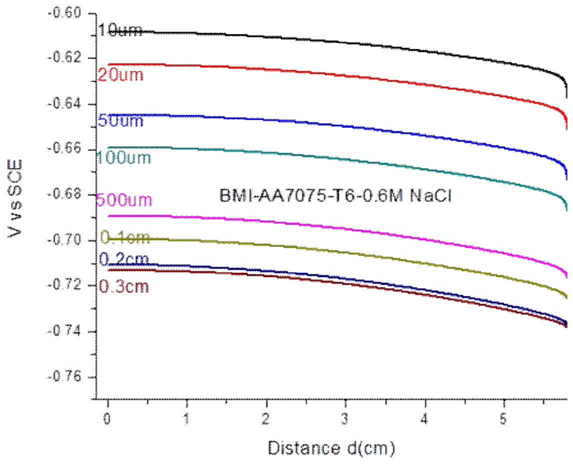

Figure 4. 20

Potential distribution along an external cathode for BMI-AA7075-T6 coupling interface for a fastener geometry with gap width from 10um to 0.3cm.

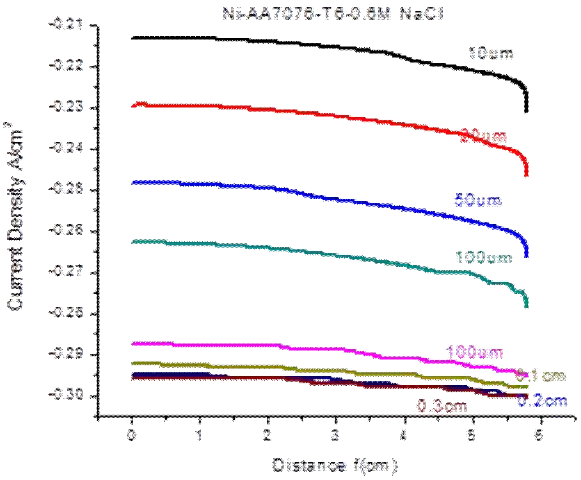 Figure 4. 21	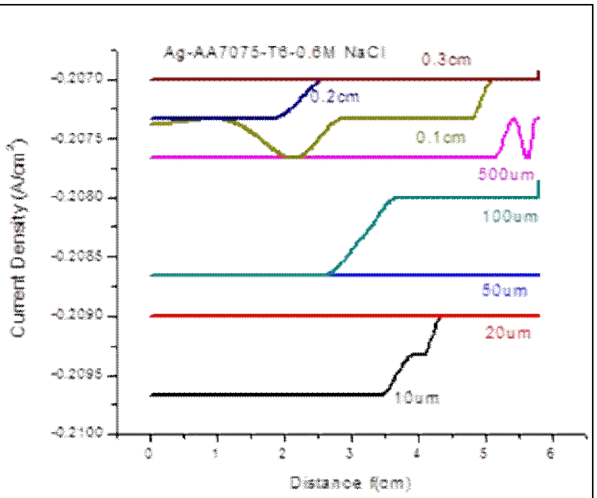 Figure 4. 22
Current Density distribution along an external cathode for Ni-AA7075-T6 coupling interface for a fastener geometry with gap width from 10um to 0.3cm.	Current Density distribution along an external cathode for Ag-AA7075-T6 coupling interface for a fastener geometry with gap width from 10um to 0.3cm.
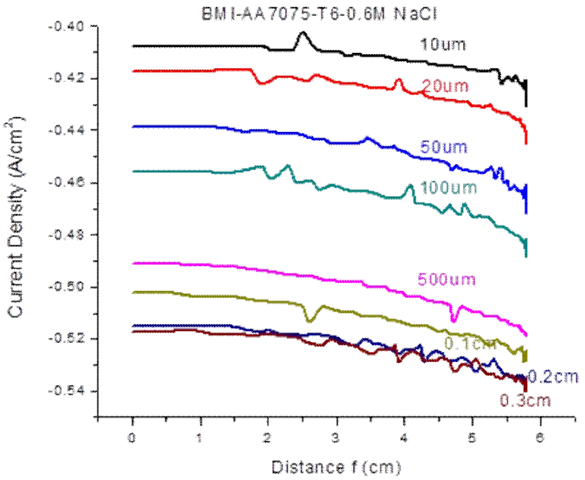 Figure 4. 23	
Current Density distribution along an external cathode for BMI-AA7075-T6 coupling interface for a fastener geometry with gap width from 10um to 0.3cm.	

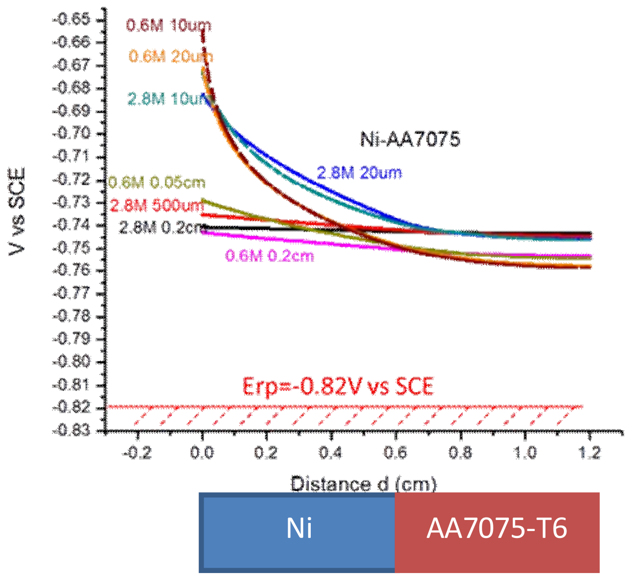

Figure 4. 24

Potential distribution along Ni-AA7075-T6 coupling interface for a fastener geometry in 0.6M and 2.8M NaCl

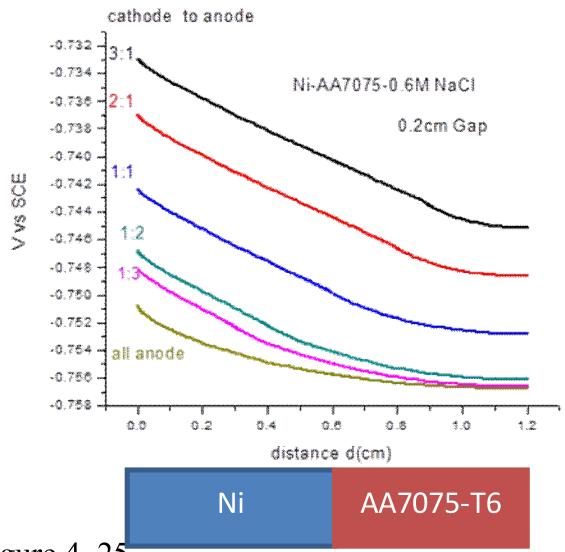

Figure 4. 25

Potential distribution along Ni-AA7075-T6 coupling interface for a fastener geometry with different cathode-to-anode area ratios, at 0.2cm gap

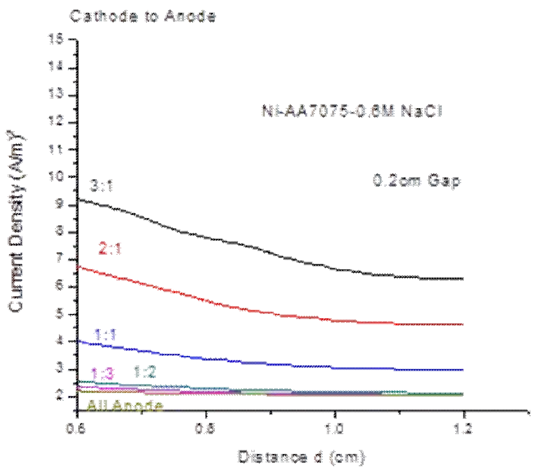

Figure 4. 26

Current density distribution along Ni-AA7075-T6 coupling interface for a fastener geometry with different cathode-to-anode area ratios, at 0.2cm gap

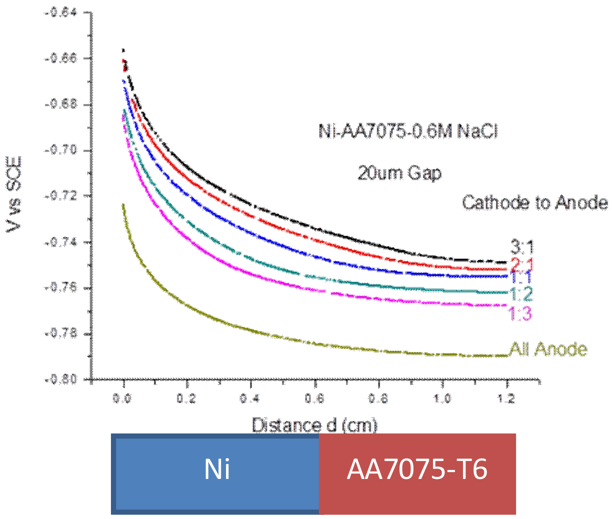

Figure 4. 27

Potential distribution along Ni-AA7075-T6 coupling interface for a fastener geometry with different cathode-to-anode area ratios, at 20um gap

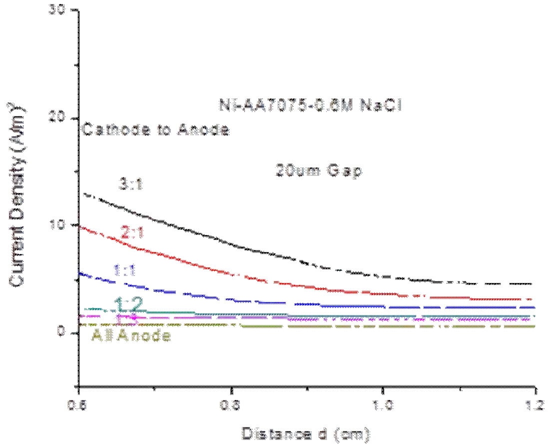

Figure 4. 28

Current density distribution along Ni-AA7075-T6 coupling interface for a fastener geometry with different cathode-to-anode area ratios, at 20um gap

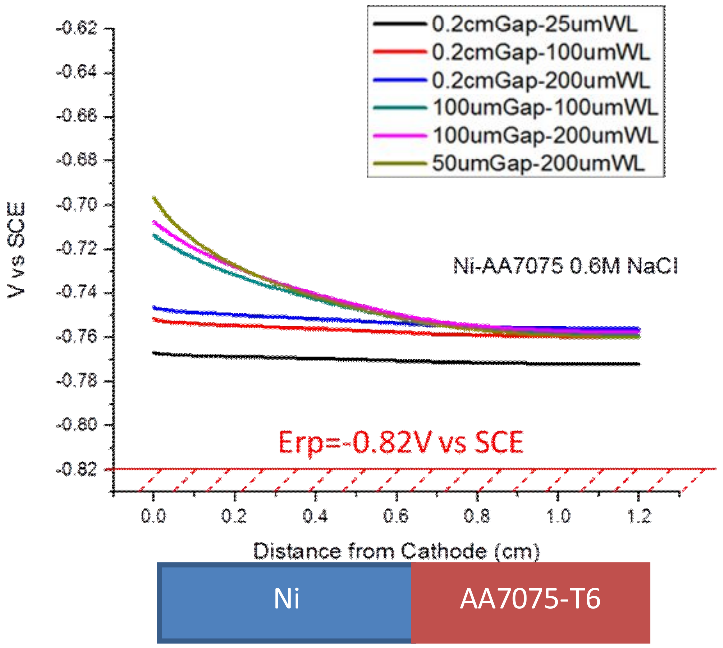

Figure 4. 29

Potential distribution along Ni-AA7075-T6 coupling interface for a fastener geometry with different electrolyte layer thicknesses.

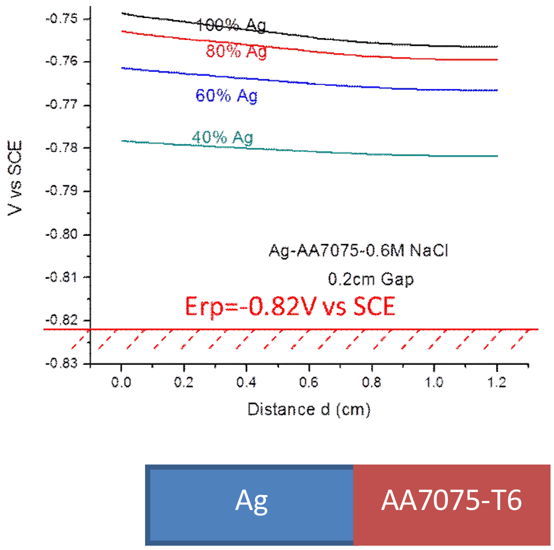 Figure 4. 30	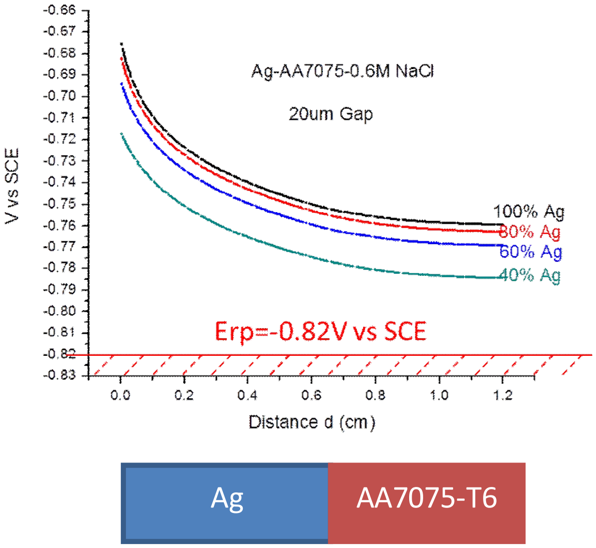 Figure 4. 31
Potential distribution along Ag-AA7075-T6 coupling interface for a fastener geometry with different PVC, at 0.2cm gap	Potential distribution along Ag-AA7075-T6 coupling interface for a fastener geometry with different PVC, at 20um gap

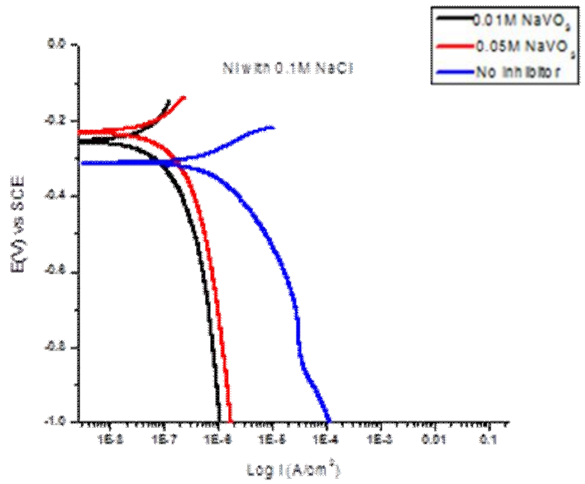

Figure 4. 32

Effect of inhibitor on cathodic kinetics on Ni

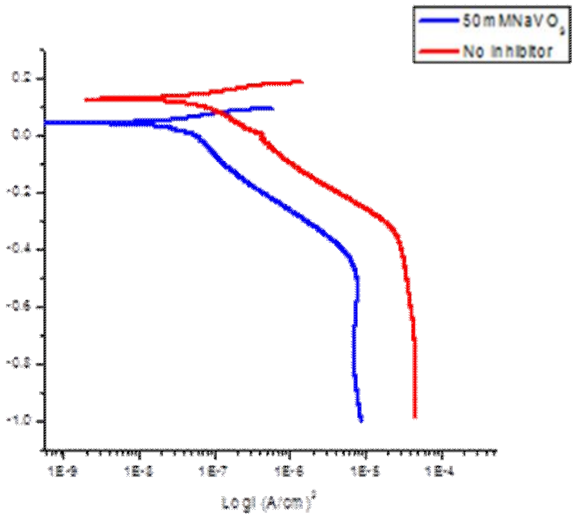

Figure 4. 33

Effect of inhibitor on cathodic kinetics on BMI

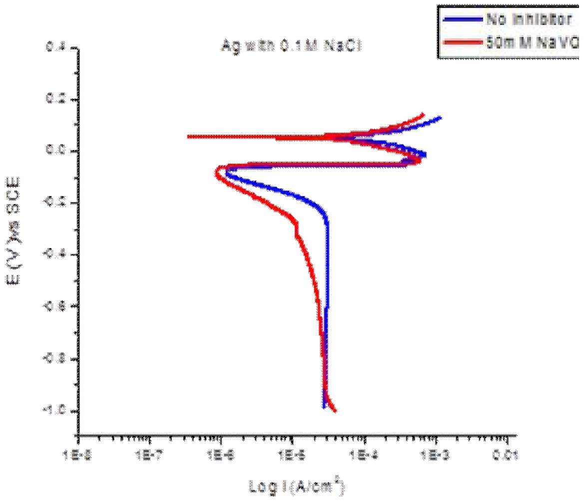

Figure 4. 34

Effect of inhibitor on cathodic kinetics on Ag

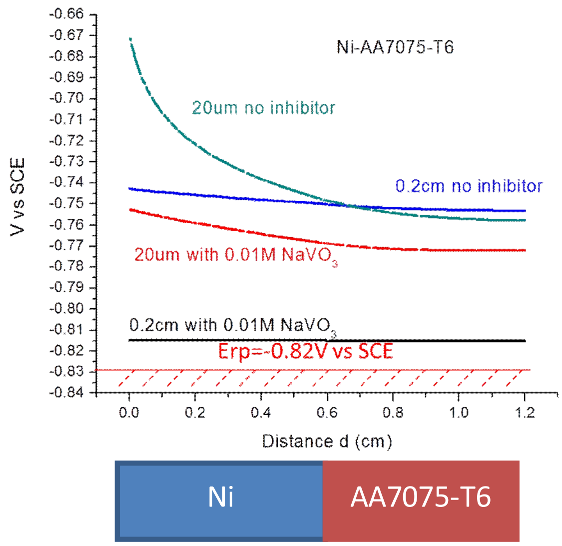

Figure 4. 35

Potential distribution along Ni-AA7075-T6 coupling interface for a fastener geometry with anode boundary condition with and without inhibitor

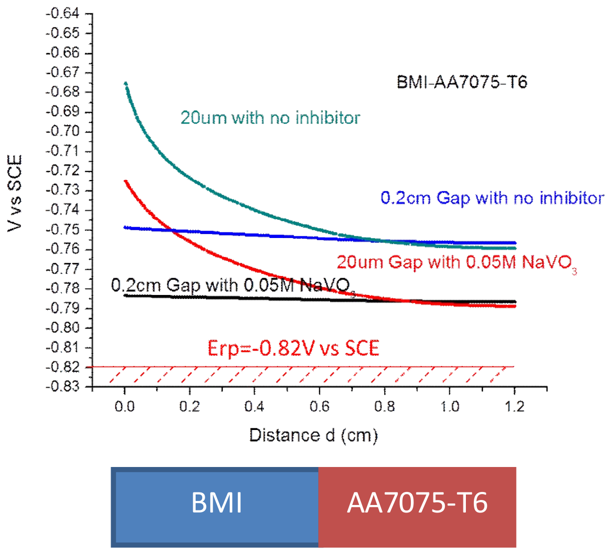

Figure 4. 36

Potential distribution along BMI-AA7075-T6 coupling interface for a fastener geometry with anode boundary condition with and without inhibitor

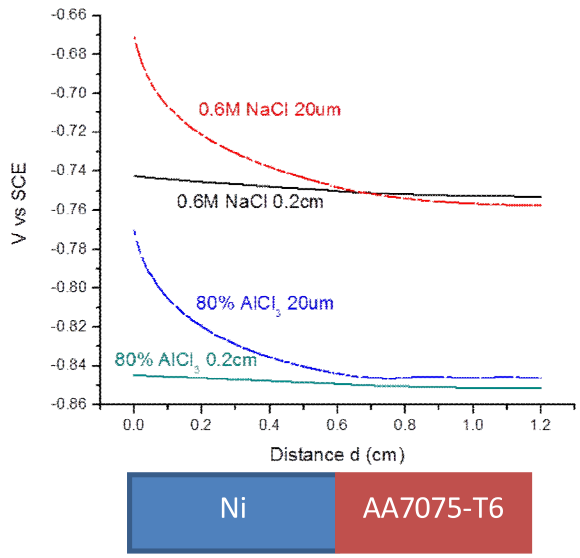

Figure 4. 37

Potential distribution along Ni-AA7075-T6 coupling interface for a fastener geometry with different gap width in NaCl and 80% Saturated AlCl$_3$ solution.

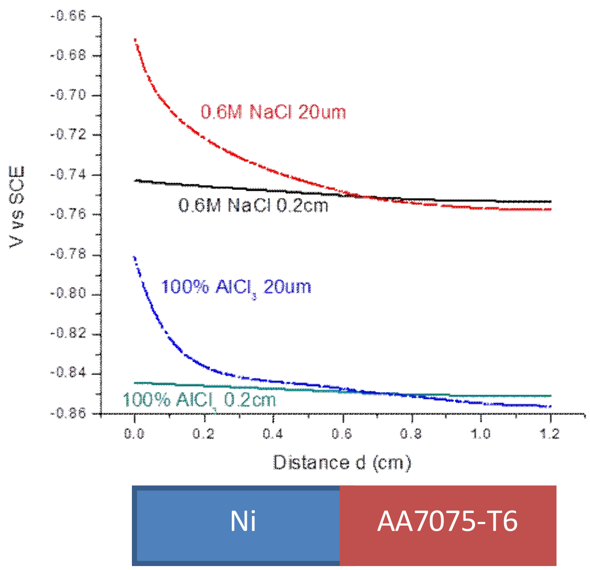

Figure 4. 38

Potential distribution along Ni-AA7075-T6 coupling interface for a fastener geometry with different gap width in NaCl and 100% Saturated AlCl$_3$ solution.

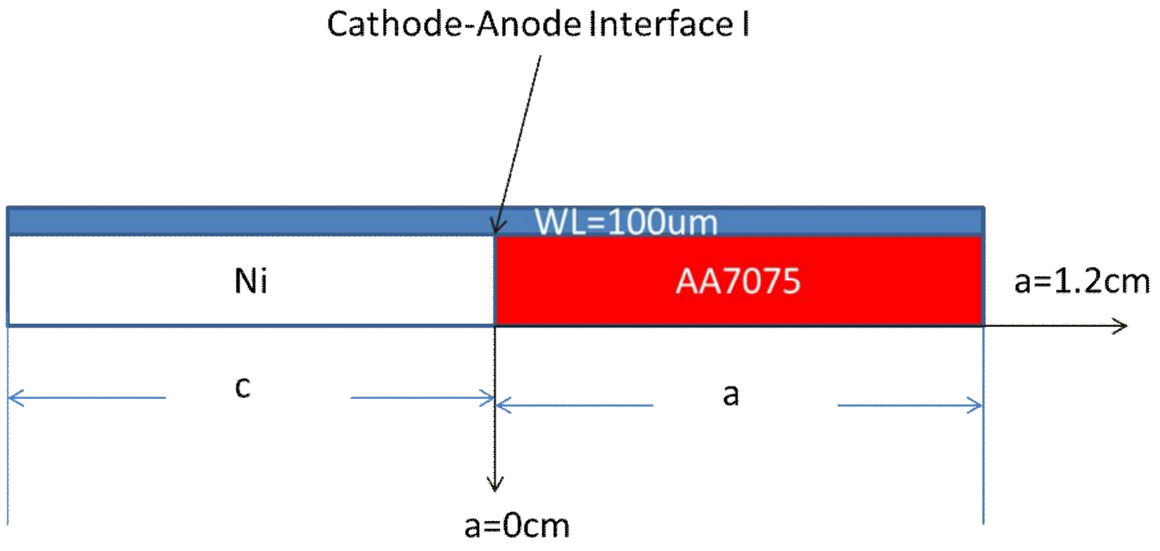

Figure 4. 39

Schematic demonstration of planar configuration for atmospheric exposure

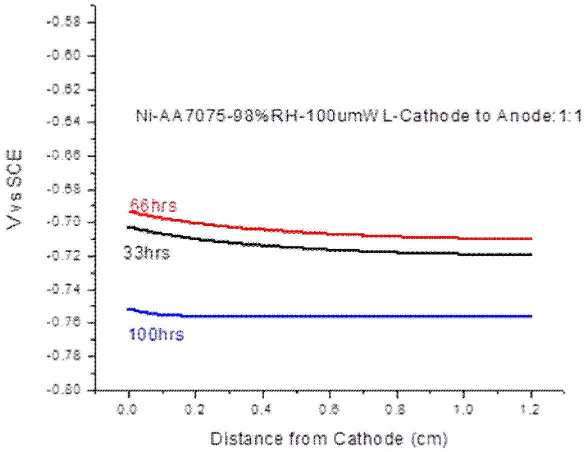

Figure 4. 40

Potential distribution vs the distance from cathode, for Ni-AA7075-T6 with RH98%, cathode-to-anode area ratio at 1:1 with 33hrs, 66hrs, and 100hrs of exposure.

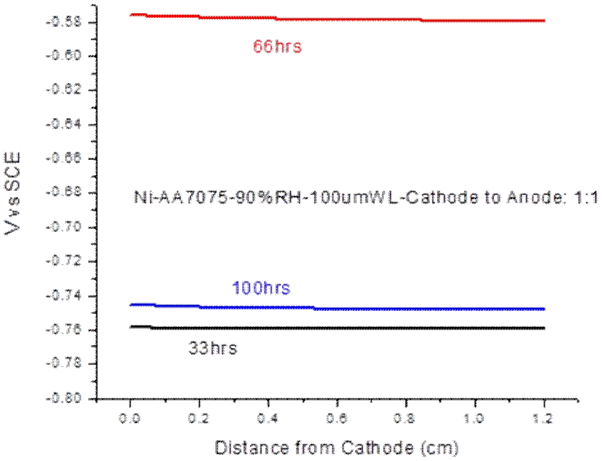

Figure 4. 41

Potential distribution vs the distance from cathode, for Ni-AA7075-T6 with RH90%, cathode-to-anode area ratio at 1:1 with 33hrs, 66hrs, and 100hrs of exposure.

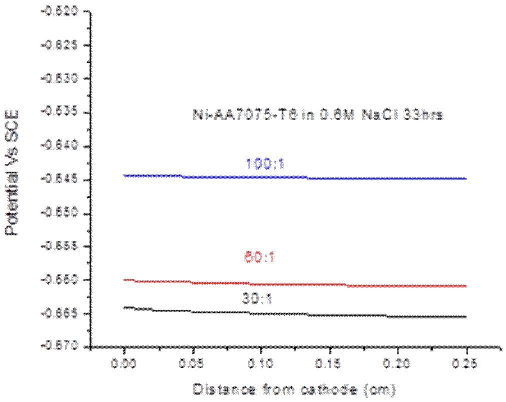

Figure 4. 42

Potential distribution vs the distance from cathode, for Ni-AA7075-T6 with RH98%, cathode-to-anode area ratio at 30:1, 60:1, 100:1 with 33hrs of exposure.

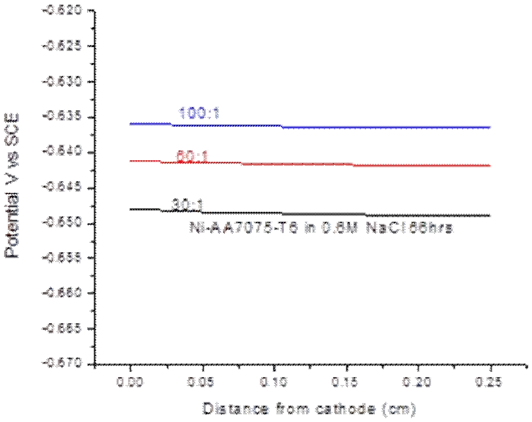

Figure 4. 43

Potential distribution vs the distance from cathode, for Ni-AA7075-T6 with RH98%, cathode-to-anode area ratio at 30:1, 60:1, 100:1 with 66hrs of exposure.

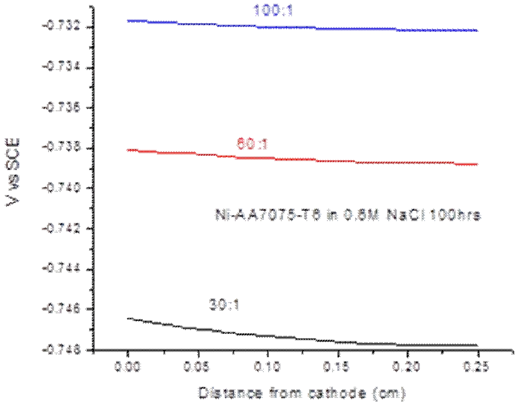

Figure 4. 44

Potential distribution vs the distance from cathode, for Ni-AA7075-T6 with RH98%, cathode-to-anode area ratio at 30:1, 60:1, 100:1 with 100hrs of exposure.

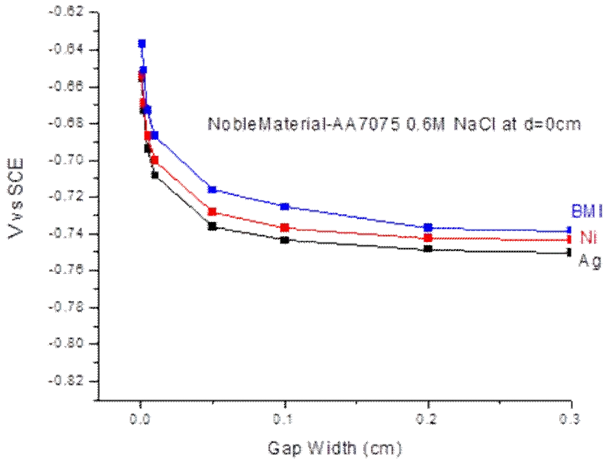 Figure 4. 45	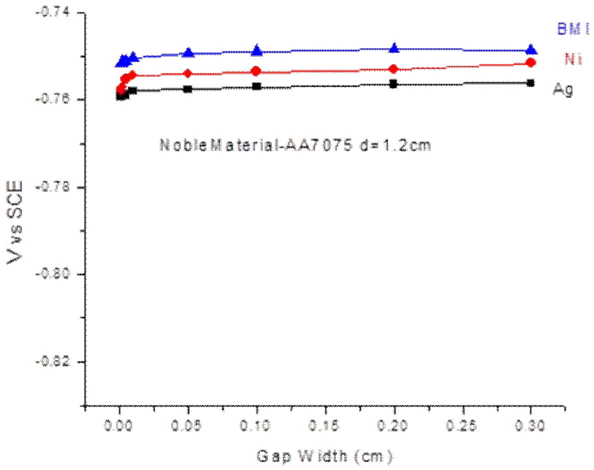 Figure 4. 46
Potential vs gap width at the mouth of fastener d=0cm for the three cathode materials	Potential vs gap width at the bottom of fastener d=1.2 cm for the three cathode materials

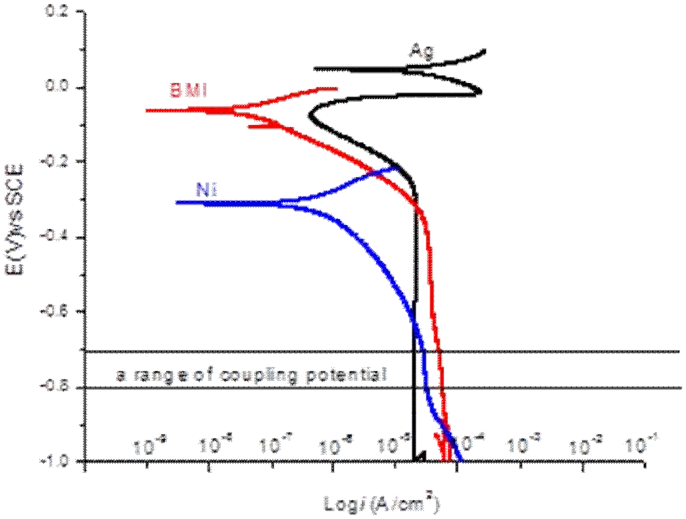

Figure 4. 47

An illustration of differences in the diffusion limited current density for the three cathode materials in the range of the coupling potentials

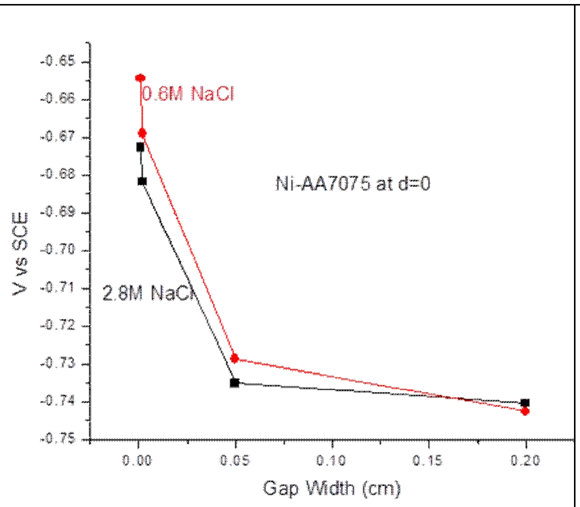

Figure 4. 48

Potential vs gap width at the mouth of fastener d=0cm for 0.6M and 2.8M NaCl

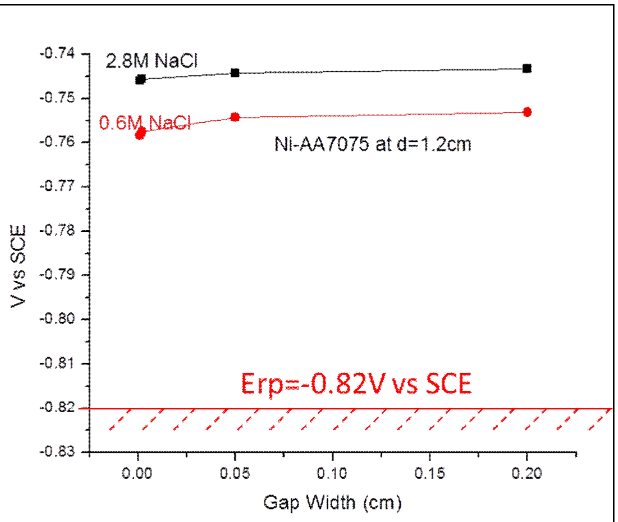

Figure 4. 49

Potential vs gap width at the bottom of fastener d=1.2cm for 0.6M and 2.8M NaCl

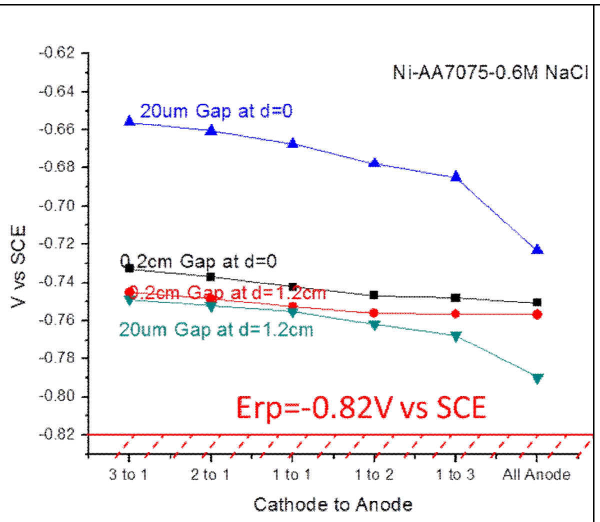

Figure 4. 50

The effect of cathode-to-anode area ratio on the potential at d=0cm and d=1.2cm for Ni-AA7075-T6 system in 0.6M NaCl

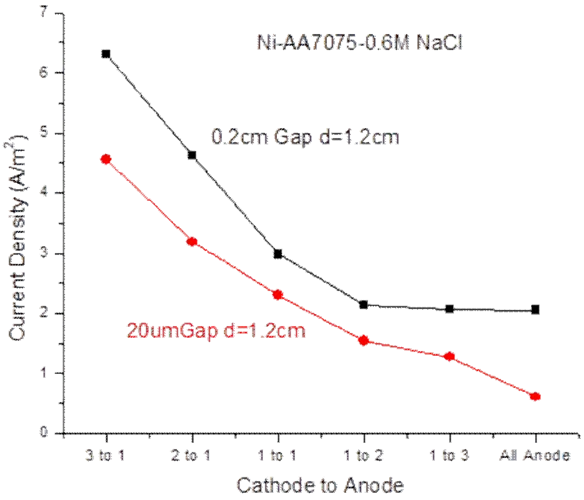

Figure 4. 51

The effect of cathode-to-anode area ratio on current density at d=1.2cm for Ni-AA7075-T6 system in 0.6M NaCl

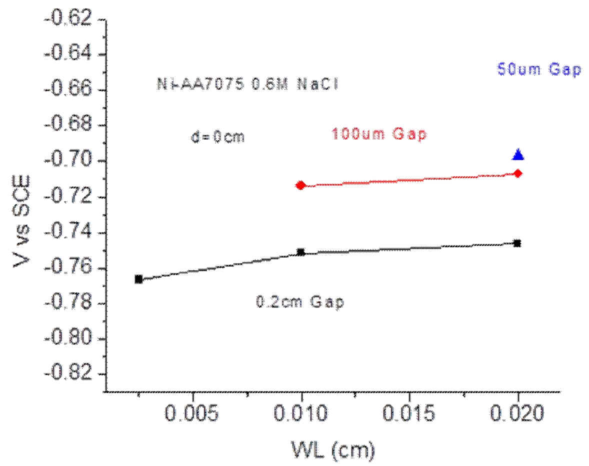

Figure 4. 52

The effect eletrolyte layer thickness on the potential at d=0cm for Ni-AA7075-T6 system in 0.6M NaCl

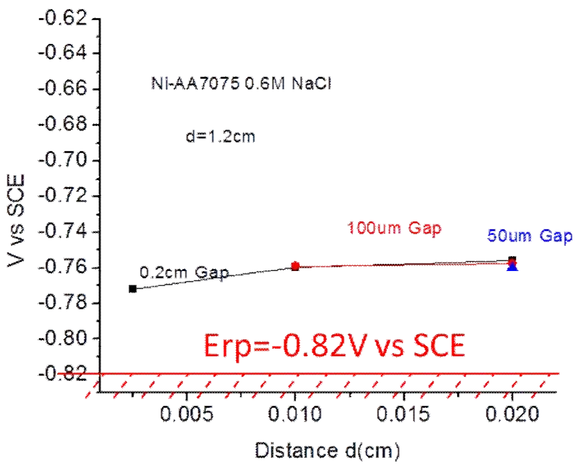

Figure 4. 53

The effect eletrolyte layer thickness on the potential at d=1.2cm for Ni-AA7075-T6 system in 0.6M NaCl

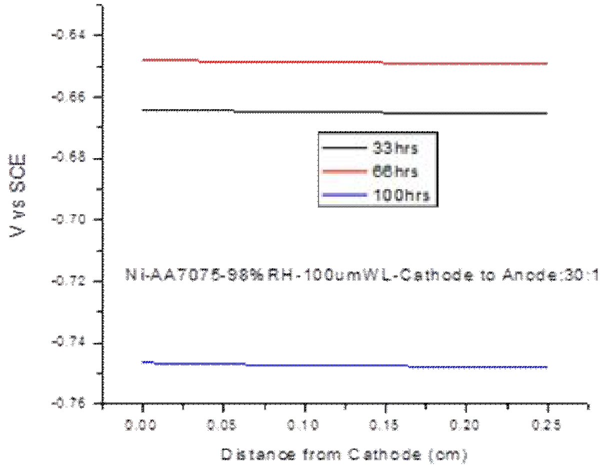 Figure 4. 54	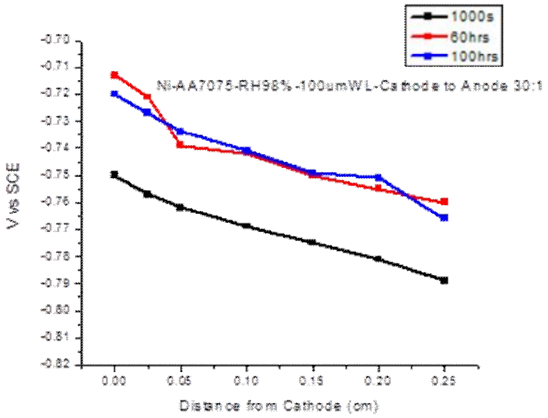 Figure 4. 55
Potential vs distance from cathode for Ni-AA7075 98%RH, cathode-to-anode area ratio 30:1 after 33hrs, 66hrs and 100hrs exposure. The results is calculated from COMSOL.	Potential vs distance from cathode for Ni-AA7075 98%RH, cathode-to-anode area ratio 30:1 after 33hrs, 66hrs and 100hrs exposure. The results is measured from SKP.
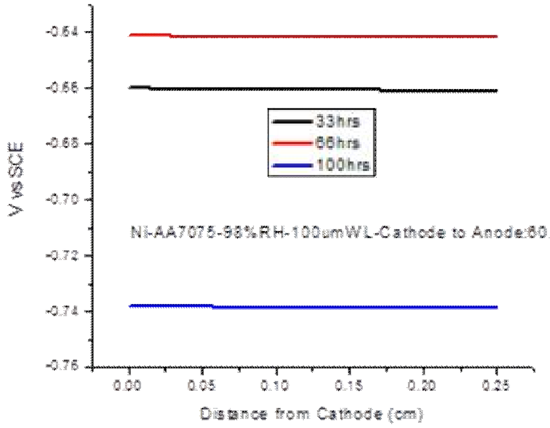 Figure 4. 56	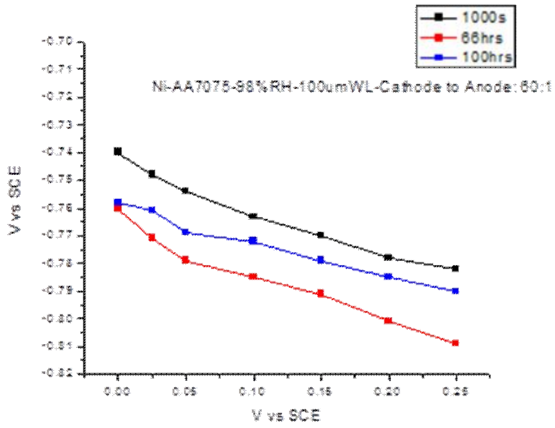 Figure 4. 57
Potential vs distance from cathode for Ni-AA7075 98%RH, cathode-to-anode area ratio 60:1 after 33hrs, 66hrs and 100hrs exposure. The results is calculated from COMSOL.	Potential vs distance from cathode for Ni-AA7075 98%RH, cathode-to-anode area ratio 30:1 after 33hrs, 66hrs and 100hrs exposure. The results is measured from SKP.

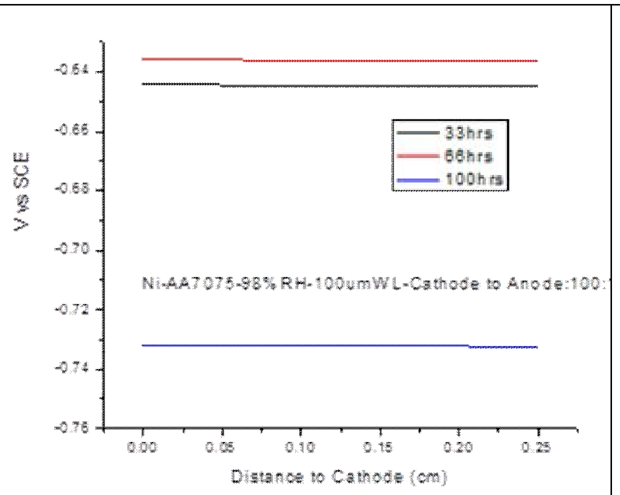

Figure 4. 58

Potential vs distance from cathode for Ni-AA7075 98%RH, cathode-to-anode area ratio 60:1 after 33hrs, 66hrs and 100hrs exposure. The results were calculated with COMSOL.

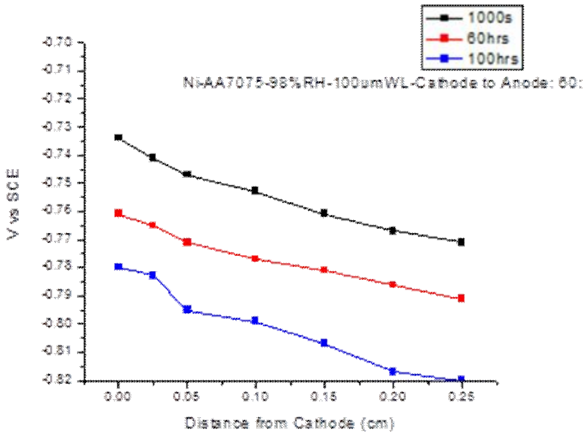

Figure 4. 59

Potential vs distance from cathode for Ni-AA7075 98%RH, cathode-to-anode area ratio 100:1 after 33hrs, 66hrs and 100hrs exposure. The result were measured with the SKP.

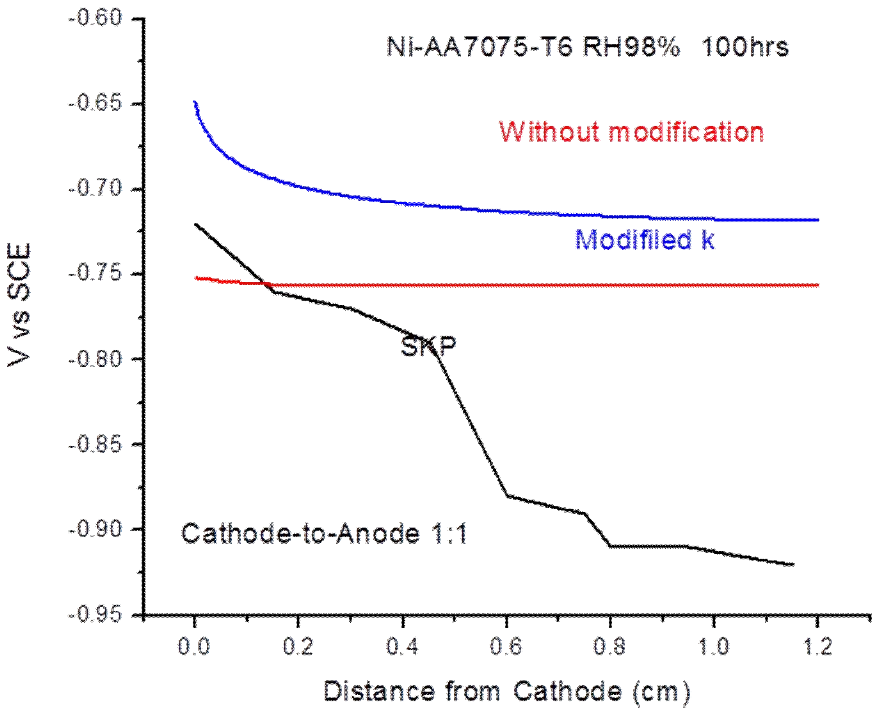

Figure 4. 60

The effect of modified solution conductivity on the potential vs distance from cathode for Ni-AA7075 98%RH, cathode-to-anode area ratio 1:1 after 100hrs exposure. The results from COMSOL and SKP are compared.

Chapter 5 Summary and Future Work

Two major questions were the focus of this research. The first question concerned the mechanism that controls the stability of localized corrosion of AA7075-T6. The second question sought to establish the conditions under which galvanically-induced localized corrosion can be stabilized for both full immersion and atmospheric conditions. A combination of experimental measurements and computational modeling were conducted to address these issues.

To answer the first question, in Chapter 2, two stability criteria, E_{rp} and i*x were measured. E_{rp} of AA7076-T6 in 0.1M and 0.6M NaCl solution were determined for both bulk and artificial pit samples. The E_{rp} ranges around -0.82V to -0.94V vs SCE for 0.6M NaCl and -0.73V to -0.80V vs SCE for 0.1M NaCl. The effectiveness of E_{rp} was validated through current decay test of artificial pit samples with prolonged exposure which showed that at a potential higher than Erp in 0.6M NaCl, the pit grow after 100000secs. i*x of AA7075 in 0.6M NaCl was determined using 25um-diameter artificial pit samples with the consideration of local cathodic current. A remarkable drop of i*x at the potential around E_{rp} shows the connection between E_{rp} and i*x. Finally, the dissolution kinetics on the corroding surface of artificial pits as a function of saturation of $AlCl_3$ was used to determine the critical solution to support the stable corrosion growth inside pits. By comparing the current density at the E_{rp}, it is the found about the current density drops remarkably when the saturation is lower than 80%, which indicate 80% saturation is required to support a high level of current density, i.e. corrosion rate inside the pit.

To answer the second question, in Chapter 3, the galvanic corrosion of AA7075-T6 coupled with different cathode materials under both full immersion and atmospheric conditions were investigated.

For the full immersion condition, the corrosion damage as a function of holding potential (-0.67V to -0.55V vs SCE) for the AA7075-T6 without external cathode was plotted to illustrate the effect of holding potential on the corrosion damages. Corrosion damage does not develop until -0.64V and higher holding potentials. IGC damages presents at higher holding potential.

Also, the damages from galvanic coupling under full immersion conditions were plotted as a function of cathode-to-anode arear ratio (1:1, 30:1, 60:1, 100:1) and the nature of cathode (Ni and BMI) in both 0.6M NaCl and 2.8M NaCl. The coupling potential and the electrochemical kinetics after the exposure were characterized to rationalize the effects of different environmental conditions. The damages from different cathode materials do not change a lot. The damages increase with the increase of cathode-to-anode area ratio, and then reached a plateau at higher cathode-to-anode area ratio. The average depth of damage for exposure solution with higher [Cl^-] is deeper if the rest of conditions remain the same.

Similarly, the damages from galvanic coupling under atmospheric exposure were compared under two different RH (98% and 90%) with different cathode-to-anode area ratio (1:1, 30:1, 60:1, 100:1) for 33hrs, 66hrs and 100hrs exposure, respectively.. The damage is most severe at the sites where anode is connected with the cathode. Less corrosion attacks are found in the anode sites where is distant from cathode.

In addition, interfacial electrochemical potential were measured during the above exposures via SKP. The potential at the damage free region along the coupling interface were compared with E_{rp} from chapter 2. It is found the damage free area corresponded to the potential that is lower than E_{rp}, which is used to validate the effectiveness of this stability criterion.

FEA modelling was introduced in Chapter 4 to further assess the stability of localized corrosion of AA7075-T6 with a fastener complex geometry. Using the stationary model, , the effects of environmental factors, including the nature of cathode, the [Cl^-] concentration, and the electrolyte layer thickness on the potential distribution along the noble materials-AA7075 interface were calculated . The effects of design factors, such as the fastener gap width, the cathode-to-anode area ratio, and the percentage of noble materials in the coating (to simulate what is known as pigment volume concentration, PVC) were also calculated. The results were compared with E_{rp} from the previous measurements to predict the stability of the galvanic corrosion for the system.

An inhibitor-modified boundary condition was also introduced. Its effect on electrochemical potential distribution was quantified. It was found the potential can decrease to a level close to E_{rp} with the addition of inhibitors with a narrow fastener gap (20μm), which is potentially promising to be used as a mitigation strategy.

A simple planar geometry was also studied under atmospheric conditions. The calculated distribution of potential along noble materials-AA7075 interface was compared with previous

SKP measurements from the samples with the same conditions. A discussion to rationalize the discrepancy between the calculated and modelling data was made.

Future Work

For Chapter 3, the damages from potentiostaic holding tests (without cathode) and the galvanic coupling test, with the same given potential, are not consistent. It may be caused by the shorter exposure time in the former test. Therefore, a longer exposure duration will be made to further investigate the corrosion damages as a function of potential for both cathode-free and galvanic condition.

The effect of corrosion products on the corrosion damages were discussed in this chapter to rationalize the discrepancy of potential from theoretical prediction (mixed potential theory) and the experimental evaluation for the atmospheric exposure condition (Chapter 3, section 3.5). A time-dependent corrosion product evolution will be monitored throughout the galvanic interaction to support the current hypothesis.

The effectiveness of E_{rp} was not validated at all the exposure conditions. More SKP measurements of the potential and damage examinations on the corroding surface of AA7075-T6 will be done to further prove the effectiveness of $E_{rp.}$

For Chapter 4, the modelling is simplified without considering the chemistry reaction of solution, or the generation of corrosion products on the corroding surface due to the saturation of local acidic chemistry through hydrolysis reaction. The conductivity of the electrolyte thus may not precisely reflect the situation in practice. A more sophisticated modelling will be developed by considering the above factors.

The current modelling is focused on only steady state condition. The time-dependent boundary condition from the experiments was used to demonstrate the effect of exposure time. The limitation of the current commercial software COMSOL eliminates the study of time evolution of the corrosion damage due to its failure of consideration ionic interactions together with the electro-neutrality. A self-coded module with the consideration of Gauss's law will be coupled into the current modelling to simulate such ionic interaction.

Validation for the modelling results with complex fastener geometry condition will also be conducted. The results will be used to further improve the current modelling setting.